CHARLES UNIVERSITY

faculty of mathematics and physics

MODELLING OF DOMAIN STRUCTURES IN FERROELECTRIC CRYSTALS

by
Pavel Márton

Doctoral thesis

Prague, July 2007

Acknowledgements

It is my pleasure to thank the people who made this thesis possible.

First of all, I would like to thank my supervisor Ing. Jiří Hlinka Ph.D. who was my advisor and mentor for my PhD. I am especially grateful for his concern, patience and friendship. Many thanks also for his insight, preciseness and honesty in scientific work which, I hope, have influenced me. It has been great to have an opportunity to work with him. He also went through the manuscript of the thesis and drew my attention to problematic parts.

I also thank RNDr. Ivan Rychetský CSc. for many discussions, Martin Kempa, Tonda Klíč and the whole department of dielectrics at the Institute of Physics of the Academy of Sciences of the Czech Republic. I will never forget years spent in this group. Special gratitude belongs to RNDr. Jan Petzelt DrSc, the head of the department.

Lastly, I am profoundly grateful to my wife Lenka for her support and love during my doctoral studies and preparation of the thesis.

This work has been supported by the Grant Agency of the Czech Republic (Project No. 202/05/H003).

Abstract

Ferroelectric materials exhibit electrical, mechanical and electromechanical properties that are being intensively studied and used in wide range of applications. These characteristics influenced by internal heterogeneous domain structure. Tailoring of material properties by engineering of underlying structure would enable design of devices with special functionalities. It however requires deep understanding of domain behavior. In spite of long-lasting research, there are still many questions opened concerning domains, domain walls morphology and motion. This work deals with investigation of ferroelectric domains in perovskite materials, particulary in $BaTiO_3$.

Generalized Ginzburg-Landau-Devonshire phenomenological approach together with symmetry analysis is used for description and analytical predictions of properties of domains and domain walls in ferroelectric crystals, e.g. domain wall thickness, shape and orientation. Landau, gradient, elastic, electrostriction and long-range dipole-dipole electrostatic interaction taken into account. Method for computations of domain wall characteristics is presented and applied to computation of all types of domain walls, that appear in $BaTiO_3$ ferroelectric phases.

Development and dynamics of a polarization field and formation of complicated ferroelectric domain patterns can be too complex to enable analytical treatment. These phenomena can be simulated numerically based on time-dependent generalized Ginzburg-Landau-Devonshire. Computational tool was developed for simulation of evolution of domain structure in bulk ferroelectric material designed to cover up variety of external conditions in order to enable investigation of material under different loading and constraints (external stress, mechanical clamping, electric field or changes of temperature). These influences are important in real applications and the model can provide simplified insight about what is happening inside the sample. The results of our computer program were demonstrated on several examples.

Abstrakt

Feroelektrické materiály vykazují elektrické, mechanické a elektromechanické vlastnosti, které jsou intenzivně studovány a využívány v množství důležitých aplikací. Tyto vlastnosti mohou být do značné míry ovlivněny vnitřní doménovou strukturou přítomnou v materiálu. Ta také poskytuje možnost dalšího vylepšování materiálových vlastností. Zvládnutí přípravy navržené doménové struktury by také umožnilo konstrukci nových materiálů a zařízení se speciálními vlastnostmi. Takový cíl však vyžaduje hlubokou znalost a porozumění chování domén. Navzdory dlouhodobému úsilí věnovanému této problematice zůstává stále mnoho otázek, týkajících se feroelektrických domén, doménových stěn a jejich pohybu, otevřených. Tato práce se zabývá studiem doménových stěn analytickými a numerickými přístupy. Především se soustředí na perovskitové materiály, konkrétně na $BaTiO_3$. Tyto materiály jsou aplikačně perspektivní mimo jiné právě díky své jednoduché struktuře.

Fenomenologický Ginzburg-Landau-Devonshire model, který zahrnuje Landauovu, gradientní, elastickou, elektrostrikční a elektrostatickou dipól-dipólovou interakci, je využit pro popis a analytické předpovědi vlastností domén a doménových stěn ve feroelektrických krystalech, například jejich tloušťky, tvaru a orientace. Model je aplikován na výpočet charakteristik všech typů doménových stěn, které se vyskytují ve feroelektrických fázích barium titanátu.

Formování a vývoj komplikované doménové struktury často není možné postihnout analytickými přístupy. Zde využíváme numerických simulací založených na časově závislém zobecněném Ginzburg-Landau-Devonshire modelu. Byl vyvinut program pro simulace vývoje doménové struktury v objemovém feroelektriku perovskitové struktury, který umožňuje zahrnutí nejrůznějších okrajových podmínek (vnější mechanické napětí, deformace, elektrické pole či změna teploty), které napodobují vlivy působící v reálných krystalech. Model může poskytnout určitý náhled do procesů probíhajících ve vzorku. Možnosti programu jsou demonstrovány na několika příkladech.

Contents

1 Introduction **15**
- 1.1 Motivation and basic definitions . . . 15
  - 1.1.1 Dielectrics and ferroelectrics . . . 15
  - 1.1.2 Domain formation . . . 16
  - 1.1.3 Domain engineering . . . 17
  - 1.1.4 Predictions of domain structure . . . 19
  - 1.1.5 Ginzburg-Landau-Devonshire theory and bulk simulation . . . 20
- 1.2 $BaTiO_3$ . . . 21
- 1.3 Related works . . . 21
- 1.4 Scope and brief overview of the thesis . . . 24

2 Generalized Ginzburg-Landau-Devonshire model **25**
- 2.1 Landau-Devonshire potential . . . 26
- 2.2 Ginzburg gradient contribution to the free energy . . . 31
- 2.3 Elastic long-range interaction . . . 33
- 2.4 Homogeneous strain and stress . . . 35
- 2.5 Electrostatic long-range interaction . . . 36

3 Charge-free elastically compatible domain walls **39**
- 3.1 Domain walls . . . 40
- 3.2 One-dimensional approximation . . . 41
- 3.3 Results . . . 48
  - 3.3.1 T180{001} domain wall . . . 48
  - 3.3.2 T180{011} domain wall . . . 48
  - 3.3.3 T90 domain wall . . . 49
  - 3.3.4 O180{$1\bar{1}0$} domain wall . . . 51
  - 3.3.5 O180{001} domain wall . . . 51
  - 3.3.6 O90 domain wall . . . 51
  - 3.3.7 O60 domain wall . . . 52
  - 3.3.8 O120 domain wall . . . 52
  - 3.3.9 R180{$1\bar{1}0$} domain wall . . . 55
  - 3.3.10 R180{$\bar{2}11$} domain wall . . . 55
  - 3.3.11 R109 domain wall . . . 55
  - 3.3.12 R71 domain wall . . . 56
- 3.4 Angle dependence of W_∞ wall thickness . . . 60
- 3.5 Discussion of the charge-free assumption . . . 61

3.6 Discussion of the Ising assumption . . . 62

4 Dynamics of polarization field 67
4.1 Lattice contribution to the dielectric constant in $BaTiO_3$ . . . 67
4.2 Soft mode concept . . . 69

5 Landau-Khalatnikov equation 71
5.1 Landau-Khalatnikov Equation in Fourier space . . . 71
5.1.1 Landau energy . . . 72
5.1.2 Gradient energy . . . 72
5.1.3 Elastostriction energy . . . 73
5.1.4 Dipole-dipole electrostatic energy . . . 73

6 Implementation details of computer programs 75
6.1 Numerical methods for solving Landau-Khalatnikov equation . . . 75
6.2 Description of programs and their parameters . . . 77
6.2.1 Program `ferrodo` . . . 78
6.2.2 List of outputs of the program `ferrodo` . . . 83
6.2.3 Program `drawarray` . . . 84
6.2.4 Program `view` . . . 84
6.2.5 Program `elast_draw` . . . 86
6.2.6 Storing of polarization field . . . 87
6.3 Simulations in one and two dimensions . . . 87
6.4 Possible domain walls in individual configurations . . . 88
6.5 Advantages and disadvantages of simulation in Fourier space . . . 89

7 Examples of simulations 91
7.1 Space accuracy of numerically obtained profiles . . . 92
7.2 Simulation of domain wall profiles . . . 92
7.3 Evolution from noise . . . 95
7.3.1 Tetragonal phase . . . 95
7.3.2 Orthorombic phase . . . 96
7.4 Switching from tetragonal to orthorombic state . . . 105
7.5 Comparison with other authors . . . 108
7.5.1 Grid spacing and time step . . . 108
7.5.2 Domain structure . . . 108
7.6 Mobility of domain walls in tetragonal phase . . . 109

8 Conclusions 113
8.1 Analytical computation of wall profiles . . . 113
8.2 Numerical simulation of domain evolution . . . 114

9 Future work 115
9.1 Implementation of absolutely stable algorithm . . . 115
9.2 Generalization of boundary conditions . . . 115
9.3 Simulation of chemical ordering and appearance of nanoclusters . . . 116

A Additional materials for analytical approach **117**

B Fourier Transform **121**
B.1 Continuous Fourier transform 121
B.2 Discrete Fourier transform 122

C Variation of the free energy functional **123**
C.1 Landau energy variation 123
C.2 Gradient energy variation 124
C.3 Elastostriction energy variation 124
C.4 Electrostatic dipole-dipole energy variation 125

D Elastostriction kernels **127**

E Tensors and transformation of coordinates **129**
E.1 Transformation of tensors 129
E.2 Voigt notation 130
E.3 Transformation matrices for domain walls in $BaTiO_3$ 131

F Compatibility relations **133**

Notation and symbols

Notation

In order to simplify tensorial relations we use abbreviated Voigt notation for symmetric tensor (Sec. E.2).

Greek indexes stands for contracted indexes $\alpha \in \{1, 2, 3, 4, 5, 6\}$, while Latin symbols $i, j \in \{1, 2, 3\}$ are indexes of directions in three-dimensional space corresponding to $\{x, y, z\}$. They are used interchangeably.

Elastically permissible non-charged domain walls in $BaTiO_3$ are discussed in this work. Twelve nonequivalent types of walls (three for tetragonal, five for orthorombic and four for rhombohedral phase) are taken into account. They are addressed by names composed of a letter denoting ferroelectric phase (T,O,R), a degree between polarization in adjacent domains (180,120,109,90,71,60) and, if necessary, also by their Miller indices (e.g. $\{001\}$) which can be omitted if discussed property does not depend on particular orientation of domain wall. Sometimes, it is necessary to address charged wall; in that case subscript c is attached to the name of the wall (e.g. $T90_c$). Considered electrically neutral elastically permissible domain walls are: T180$\{001\}$, T180$\{011\}$, T90, O180$\{1\bar{1}0\}$, O180$\{001\}$, O90, O120, O60, R180$\{1\bar{1}0\}$, R180$\{\bar{2}11\}$, R109, R71.

Symbols

Symbol	Unit [SI]	Meaning of the symbol	Definition
F	$\mathrm{kg\,m^2\,s^{-2}}$	Free energy	(page 25)
f_L	$\mathrm{kg\,m^2\,s^{-2}}$	Landau energy density	(page 26)
f_G	$\mathrm{kg\,m^2\,s^{-2}}$	Gradient energy density	(page 31)
f_C	$\mathrm{kg\,m^2\,s^{-2}}$	Elastic energy density	(page 28)
F_q	$\mathrm{kg\,m^2\,s^{-2}}$	Electrostriction energy density	(page 28)
F_dep	$\mathrm{kg\,m^2\,s^{-2}}$	Dipole-dipole electrostatic energy density	(page 36)
F_Cq	$\mathrm{kg\,m^2\,s^{-2}}$	Elastostriction energy density	(page 25)
$f_\mathrm{L}^{(e)}$	$\mathrm{kg\,m^{-1}\,s^{-2}}$	Clamped Landau energy density	(page 26)
P_i	$\mathrm{C\,m^{-2}}$	Polarization field	
u_i	m	Field of displacements	
e_{ij}	1	Component of a strain tensor	(page 25)
σ_{ij}	$\mathrm{kg\,m^{-1}\,s^{-2}}$	Component of a stress tensor	
α_i	$\mathrm{kg\,m^3\,s^{-2}\,C^{-2}}$	Coefficients of Landau expansion	(page 26)
α_{ij}	$\mathrm{kg\,m^7\,s^{-2}\,C^{-4}}$		
α_{ijk}	$\mathrm{kg\,m^{11}\,s^{-2}\,C^{-6}}$		
α_{ijkl}	$\mathrm{kg\,m^{15}\,s^{-2}\,C^{-8}}$		
G_{ij}	$\mathrm{kg\,m^5\,s^{-2}\,C^{-2}}$	Gradient constants	(page 31)
q_{ij}	$\mathrm{kg\,m^3\,s^{-2}\,C^{-2}}$	Electrostriction constants	(page 28)
Q_{ij}	$\mathrm{m^4\,C^{-2}}$	Electrostriction constants	(page 30)
C_{ij}	$\mathrm{kg\,m^{-1}\,s^{-2}}$	Elastic constants	(page 28)
$\epsilon_\mathbf{B}$	1	Background permittivity	(page 36)
ϵ_0	$\mathrm{kg\,m^3\,s^{-2}\,C^{-2}}$	Permittivity of vacuum	
g_α	$\mathrm{kg\,m^{-1}\,s^{-2}}$	Electrostriction stress components	(page 28)
$A_{\rho\sigma}$	$\mathrm{kg^{-1}\,m\,s^2}$	Tensor of elastostriction kernels	(page 35,127)
E	$\mathrm{kg\,m\,s^{-2}\,C}$	Electric field	
T	K	Temperature of the sample	
Λ	$\mathrm{C^2kg^{-1}m^{-3}s}$	Kinetic coefficient in Landau-Khalatnikov Equation	(page 71)
U	$\mathrm{kg\,m^{-1}\,s^{-2}}$	Energy barrier in Euler-Lagrange potential	(page 45)
A	$\mathrm{kg\,m^{-1}\,s^{-2}}$	Depart from simple *tanh* profile	(page 44)
Σ	$\mathrm{kg\,s^{-2}}$	Surface energy of a domain wall	(page 45)
2ξ	m	Domain wall thickness	(page 44)
Δ	m	Numerical grid spacing	(page 75)
τ	1	Numerical time step	(page 75)
Y_α	$\mathrm{C^2\,m^{-4}}$	Component of the vector of squares of polarization	(page 35)
μ_E	$\mathrm{m^2\,V^{-1}\,s^{-1}}$	Mobility of a domain wall under electric field E	(page 109)

Chapter 1

Introduction

1.1 Motivation and basic definitions

1.1.1 Dielectrics and ferroelectrics

An increasing number of systems utilizes internal electrical, mechanical and electromechanical properties of dielectric materials. Telecommunication systems, detection and measurement devices are common examples, though applications are far from being limited to this area. Coupling in smart materials make it possible to transform electric, magnetic, thermal or other energy fields into mechanical deformation et vice versa. Piezoelectricity and electrostriction enables construction of various experimental and medical probes, sensors, transducers and positioning devices with nanometric accuracy, transformers of AC voltage or active elements for suppression of vibrations, stabilizers, or actuators e.g. Refs. [1, 2, 3]. High value and possible tunability of a dielectric constant is appreciated in a range of microelectronic devices and systems for electronic communication.

Dielectric materials are electrical insulators, substances highly resistant to the flow of electric current. They are well penetrable by electric field. The lack of charge carriers causes only partial compensation of applied electric field originating from small displacement of bound charges. The efficiency of compensation is determined by a dielectric constant - permittivity. In the case of ionic insulators, the polarization[1] is directly bound with deformation of the crystal grid. The strain is accessible by external electric field and a material exhibits (at least) inverse piezoelectric effect[2]. Electric permittivity is frequency dependent since it is connected with crystal lattice dynamics. Important subgroup of ionic insulators, polar dielectrics, posses spontaneous dipole moment, which appears due to mutual shift of individual positively and negatively charged ions with respect to one another. These materials lack center of symmetry[3] and exhibit pyroelectric effect[4].

Ferroelectric materials are dielectric substances that are pyroelectrics and have at least two equivalent states that differ only in the direction of the spontaneous polarization [4], and polarization can be switched[5] by electric field from one state to another. Hysteresis and saturation

[1] Polarization is dipole moment per unit volume.

[2] Strain appears at applied electric field.

[3] There is a symmetry restriction: 20 point groups out of 32 are piezoelectric and only 10 of them are pyroelectric.

[4] Variation of polarization with temperature

[5] Generally, substances that exhibit some property (e.g. polarization, magnetic moment, strain) which can

are essential properties of ferroelectrics. In ferroelectrics, additional contribution to electronic and ionic (lattice) permittivity is possible due to motion of domain walls and reorientation of polarization domains.

Ferroelectric materials exhibit large piezoelectric and dielectric properties[6] (Fig. 1.7) and are therefore being used in all previously mentioned devices. Ferroelectrics are closely related to other technologically important materials like relaxor ferroelectrics[7] or multiferroics[8].

1.1.2 Domain formation

Typical feature of ferroelectric materials is formation of ferroelectric domains. Most ferroelectrics have a high-temperature, high-symmetry paraelectric phase with zero spontaneous polarization [5]. As temperature falls, the dielectric constant increases and reaches its maximum at the transition temperature. Material changes its symmetry and undergoes phase transition to a non-centrosymetric ferroelectric phase. On continual cooling, down it is sometimes possible to reach another ferroelectric phases. An order parameter[9] of ferroelectric phase transition is a vector of spontaneous polarization. At least two possible equivalent directions of spontaneous polarization give rise to ferroelectric domain structure[10]. Inside ferroelectric domain the polarization is homogeneous. Domains are separated by domain walls where the polarization vector changes between spontaneous values of polarization in adjacent domains.

Domain architecture is generally complicated and it is strongly dependent on many factors like method of growth of the crystal, its history, external mechanical constraints, electric field, temperature, internal defects, crystal conductivity etc. Size of a ferroelectric domain can vary from millimeters in the case of mono-domain crystals down to nanometric dimensions. It also strongly depends on external conditions and history of a sample.

Ferroelectrics domains in a bulk single-crystal are shown in Fig. 1.1. They were observed on 125μm-thick sample by contact scanning force microscopy technique [7]. Images show contrast that results from crossing of internal domain structure with the surface of the crystal. Domain size here ranges from 1 up to 10 μm. Ferroelectric are, however, used not only as single-crystals but also in the form of powders, polycrystalline and ceramic components. Fig. 1.2 shows $BaTiO_3$ grains mechanically strained with other grains in the ceramics. The twin structure is very fine, domain thickness can be estimated to just about 20 nm. Fig. 1.3 reveals domain size even below 20 nm for epitaxial $PbTiO_3$. Unit cell in these materials is almost cubic with dimension about 4 nm. The domain is only about 50 unit cells thick.

Domains represent additional degree of freedom for material to relax mechanical energy of

be switched (by means of electric field, magnetic field, stress or combination of these) from one spontaneous orientation state to another are called ferroics [6].

[6]Value of dielectric constant can be strikingly high (even in orders of 1000) namely in the vicinity of a phase transition temperature.

[7]Relaxors exhibit smooth and frequency dependent maximum of dielectric constant at phase transition temperature.

[8]E.g. magnetoelectrics where electric polarization could be directly driven by magnetic field or vice-versa.

[9]Order parameter – phase transition parameter changes its property quantitatively through phase transition. It is used to expand free energy in Landau theory (see Sec. 2). It has two basic aspects [8]. Symmetry aspect: Phase transition parameter determines possible symmetry of low symmetry phase. Physical aspect: The crystal is unstable at transition temperature with respect to phase transition parameter with all other extensive thermodynamic parameters held constant.

[10]Consequently, ferroelastic domain structure may also appear in species with strong electromechanical coupling.

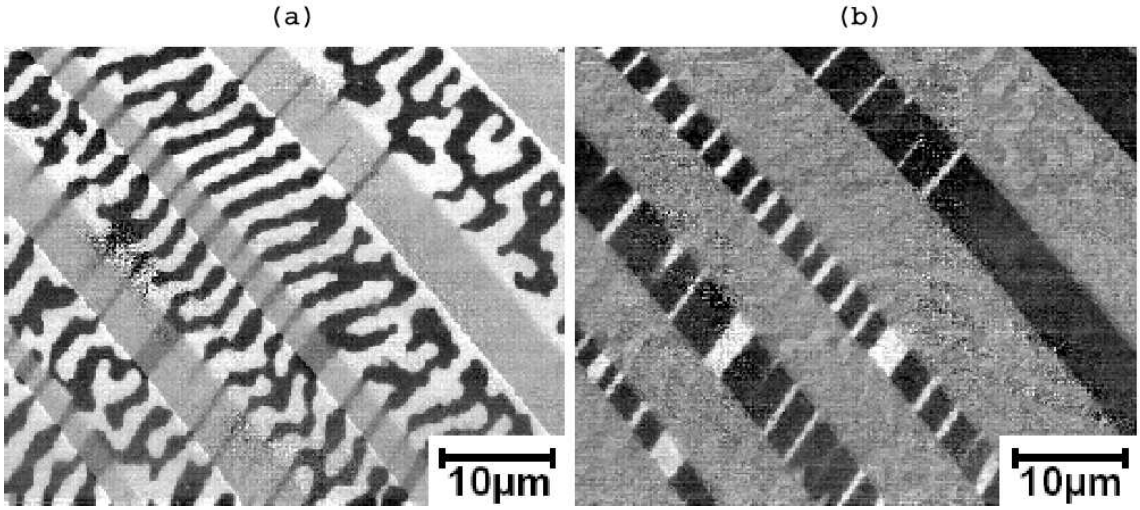

Figure 1.1: Contact scanning force measurements of domain distribution at ferroelectric surfaces in $BaTiO_3$. (a) Out-of-plane polarization signal (bright and dark areas correspond to polarization pointing out of and into the sample, resp. (b) In-plane polarization, bright and dark areas correspond to polarization pointing to the up right and down left, resp. Images are taken from Ref. [7].

external clamping. It is well known that underlying domain structure has enormous impact on properties and response of the material. It can be stated: "The finer the domain structure, the higher the dielectric constant". In Ref. [9] the authors claim that the wall motion contribution to the dielectric constant may be up to 80% in $BaTiO_3$ ceramics with 1 μm grain (value strongly depends on grain size).

Effective properties of a material depend on a volume fraction of individual domains, their ordering, dynamics, shape, density and mobility of domain walls.

1.1.3 Domain engineering

Both benefits and drawbacks resulting from domain formation lead to increasing interest in domain structure. Formation of domain provides material engineers with another tool for improving material properties. It is expected that with use of various techniques it could be possible to produce engineered domain structure with desired morphology and properties (Ref. [10, 3]). There has been attempts to control domain architecture experimentally, but there is still lack of answers to many questions, e.g processing, design of structure with defined behavior under external electrical or mechanical loading. Formation of domains is not always desired[11]. Question arises how to avoid unwanted domains.

The concept domain engineering is mostly used in the literature for poling of ferroelectric crystals by sufficiently large electric field applied along one of the possible polar axes of the crystal other than zero-field polar axis [13]. Resulting domains are then equivalent with respect to the applied field and there is no motion of domain walls. In broader sense, the concept of domain engineering is used to denote modification of domains in material in order to produce

[11]Monodomain single-crystals are required for certain applications and domain formation can result in inappropriate change of material properties.

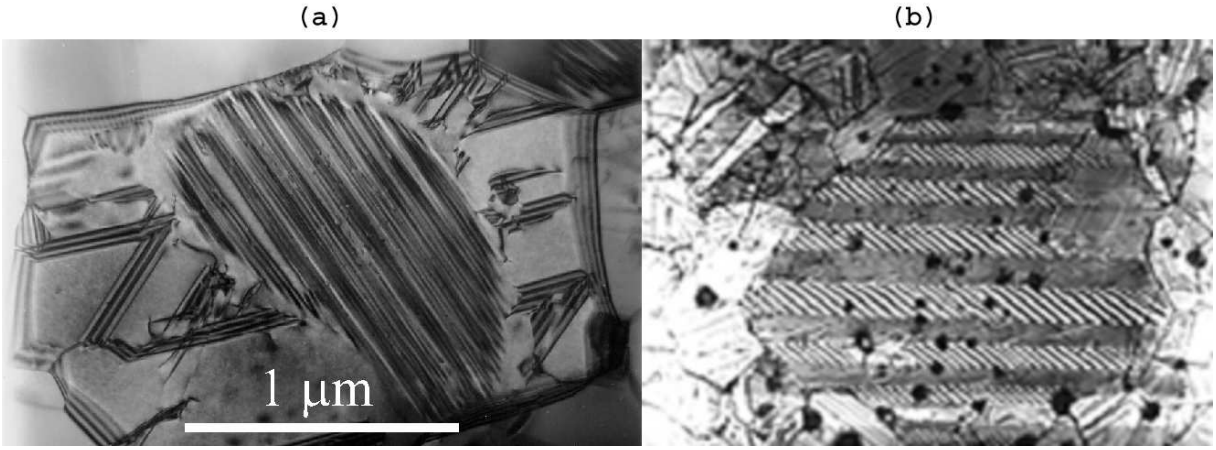

Figure 1.2: (a) Transmission electron microscopy and (b) reflected light microscopy of a domain structure in mechanically clamped grain in $BaTiO_3$ ceramics. Micrographs taken from Ref. [72, 73].

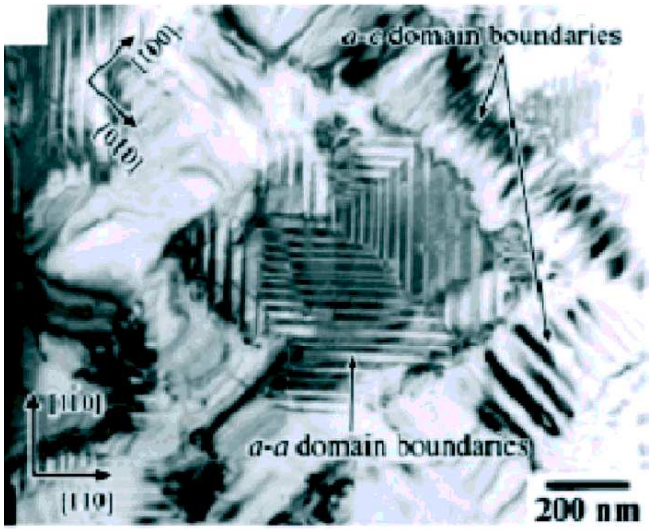

Figure 1.3: Transmission electron microscopy of a domain structure in an epitaxial $PbTiO_3$ (Ref. [1])

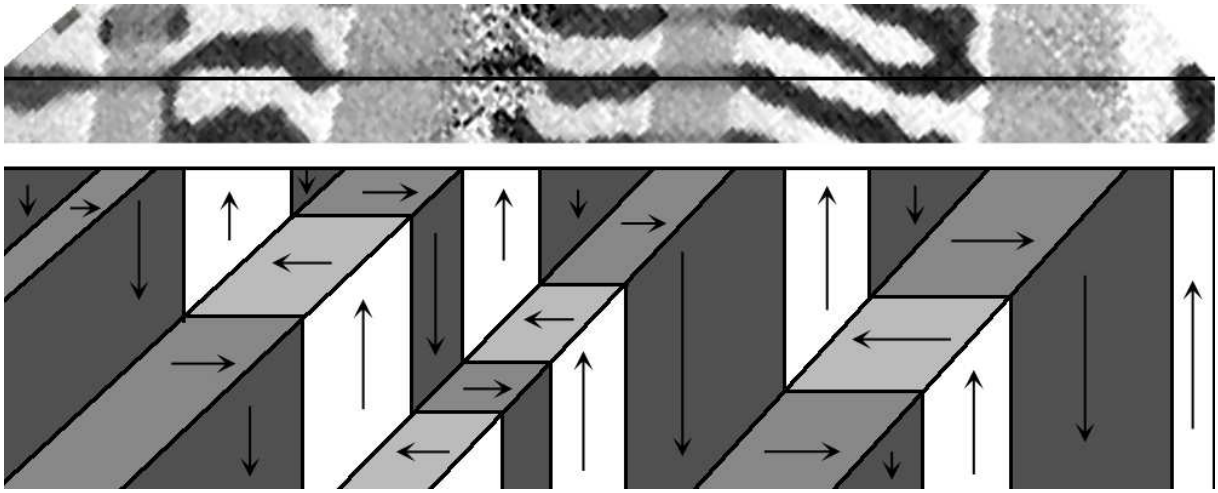

Figure 1.4: Estimate of domain structure from surface polarization. Upper figure was cut from Fig. 1.1 and rotated by 45 degree. Black line indicates cross section of the image bellow with the surface of the sample. Bottom figure suggests domain structure. Direction of polarization vector is indicated by arrows, their length is irrelevant. Color scheme used corresponds roughly to the upper figure. If the bevel domain walls were for example inclined to the opposite direction, they would be charged (heads of arrows will head towards each other).

desired structure or properties (Ref. [15, 16]).

It is indicated by supporting Figs. 1.1,1.2,1.3 that domain properties are strongly dependent on size and external constraints of a material. In powders, ceramics, thin films and single-crystals the domain structure is under different electromechanical conditions. From clamping of grains in ceramics to perfect mechanical clamping in epitaxial thin films where the lattice constant is adjusted to the substrate. Also resulting response is different.

1.1.4 Predictions of domain structure

In principle, although domain structure can be quite complicated, basic types and geometrical properties of domain walls in a ferroelectric material can be usually derived from symmetry, elastic compatibility conditions and electrostatic considerations [4, 17]. For example, this kind of considerations allows one to predict preferred crystallographic orientations of 180 degree and 90 degree domain boundaries in tetragonal $BaTiO_3$ that is classical model materials. Such estimation of material domain structure is demonstrated in Fig. 1.4, where polarization inside the sample is predicted in order to create mutually mechanically compatible domains and non-charged domain walls.

Important tool of today physics, computer simulations are being used in ferroelectric at different levels. Ab-initio quantum mechanic computations, computations at finite temperature as molecular dynamics or Monte-Carlo simulations are usually limited to small number of particles (at best thousands), and therefore are not suitable for predictions of domain structure.

In the past, phase field models using phenomenological potentials appeared in the literature [18, 20, 21]. Phase field simulations enable not only prediction of complicated domain structure, but also its dynamics that is critical for controlling of piezoelectric and dielectric properties of a material.

Internal structure of materials is usually probed by spectroscopic methods. Simulations with carefully chosen parameters can produce valuable insight into processes that take place inside the material and are not directly accessible by experimental observations. Continuous simulations are still, however, limited to relatively small (submicron) areas.

1.1.5 Ginzburg-Landau-Devonshire theory and bulk simulation

In this thesis a continuous generalized Ginzburg-Landau-Devonshire (GGLD) phenomenological model is used to deal with domains and domain walls in bulk ferroelectric perovskite material. A free energy functional is constructed in term of powers of polarization components, its derivatives and components of strain tensor. Polarization and strain are taken as primary and secondary order parameter. Landau potential, exchange gradient, elastic, electrostriction and electrostatic dipole-dipole energy are taken into account in the model.

Time-dependent Landau-Khalatnikov equation governs evolution of polarization field in numerical simulations. Similar phase-field models are used e.g. in simulation of precipitation in alloys, twinning in martensites or ferromagnetics with their own specifics. Assumption of periodicity of polarization and strain fields enable computations Fourier space. Careful choice of mechanical boundary conditions also enables simulation of behavior of a sample under various conditions. Ferroelectric thin films and small grains will be different compared to bulk samples, because there are additional problems concerning e.g. surfaces or substrate clamping (Ref. [1]), but the model can also account for some features of these systems.

Full understanding of evolution of domain structure, response to temperature changes and applied external electric field or stress would require to take into account all features of materials, e.g. influence of internal conductivity (that is small but not always negligible), defects (vacancies, impurities, dopants etc.) or layers at grain boundaries with different chemical composition which can drastically decrease dielectric properties. Although there were several attempts to introduce effects of imperfections into the model (e.g. in Ref. [22, 23, 24]), it is still heuristic approach.

In this work, this defects, imperfections and other random fields are not taken into account unless explicitly stated.

In this work only simple models of defects are used in several simulations.

Important representant of perovskite family of ferroelectrics, $BaTiO_3$, will be discussed. Model can be, after few marginal modifications, also used for description of other perovskites. Due to technological progress in manufacturing higher quality materials and continuing miniaturization of devices this model can produce valuable information in spite of previously described simplifications. Model is very sensitive to correct determination of involved constants. Parameters for barium titanate used in simulations was determined and discussed in [13, 26, 20].

Table 1.1: Sequence of ferroelectric phase transitions in $BaTiO_3$. The symbol of phase transition species is according to [29]. A name consists of three parts. First is a paraelectric point group. Second part indicates orientation of spontaneous polarization with respect to symmetry element (DX(m) and AX(m) means parallel and perpendicular to the X-fold axis (plane), resp). In the end there appears symbol of ferroelectric point group preceded by F (for ferroelectric).

Phase transition	Temperature (K)	Transition species
cubic → tetragonal	398	m3mD4F4mm
tetragonal → orthorombic	281	m3mD2Fmm2
orthorombic → rhombohedral	202	m3mD3F3m

1.2 $BaTiO_3$

$BaTiO_3$ is a typical ferroelectric material and representant of family of perovskites[12]. High temperature paraelectric (with zero spontaneous polarization) phase is cubic. In the corners of the cube there are barium ions, the titanium ions at the body center and oxygen ions at face centers. On cooling down, individual ions slightly shift with respect to one another, electrical dipole is created or changes its orientation and a material undergoes ferroelectric phase transition. In $BaTiO_3$, there is sequence of phase transitions from high-temperature paraelectric cubic $Rm\bar{3}m$ (O_h^1) (ITA 221) to ferroelectric tetragonal $P4mm$ (C_{4v}^1) (ITA 99)[13], orthorombic $Amm2$ (C_{2v}^{14}) (ITA 38) and rhombohedral $R3m$ (C_{3v}^5) (ITA 160) phase. Complete list of phase transition species in $BaTiO_3$ is given in Tab. 1.1. All these phase transitions exhibit peak of dielectric constant. $BaTiO_3$ is therefore a proper ferroelectric material according to classification [8]. First-order character (according to the Ehrenfest classification) of all ferroelectric phase transitions is indicated by discontinuity in physical properties corresponding to the first and higher derivatives of the thermodynamic potential.

$BaTiO_3$ is good insulator with resistivity about $10^{10}\ \Omega\,\mathrm{m}$ at $100\ \mathrm{kV\,m^{-1}}$ [30] for as-grown crystal or ceramics (strongly dependent on purity of material, dopants, electrodes etc.). Electrical conductivity is therefore neglected. Lattice constant is $a = 3.996\ \mathring{A}$ [30]. It is almost the same in all ferroelectric phases (mechanical strain is up to 1% in all phases).

Example of temperature dependence of dielectric constant for $BaTiO_3$ ceramics with various grain size is given in Fig. 1.7.

1.3 Related works

Analytical computation of shapes of domain walls follows the works of W. Cao and L.E. Cross [33]. The authors derived analytical solution for 90 degree and 180 degree domain wall in

[12]Perovskites are relatively simple technologically important compounds with a structure of $CaTiO_3$. Chemical formula is ABO_3. Crystal structure is a primitive cubic with A-cation in the middle, B-cation in the corner and oxygens in the center of edges. Perovskite materials are e.g. ferroelectric $BaTiO_3$, $PbTiO_3$, $KNbO_3$, incipient ferroelectric $SrTiO_3$ and other substances with variety of phase transitions (ferroelectric, anti-ferroelectric, ferroelastic) like $CaTiO_3$, $NaNbO_3$, $PbZrO_3$, $BaZrO_3$.

[13]Space group number (Ref. [50]).

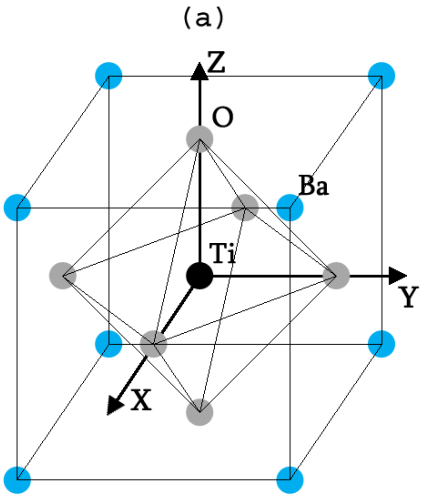

Figure 1.5: Unit cell of $BaTiO_3$ with the position of atoms of barium, titanium and oxygen.

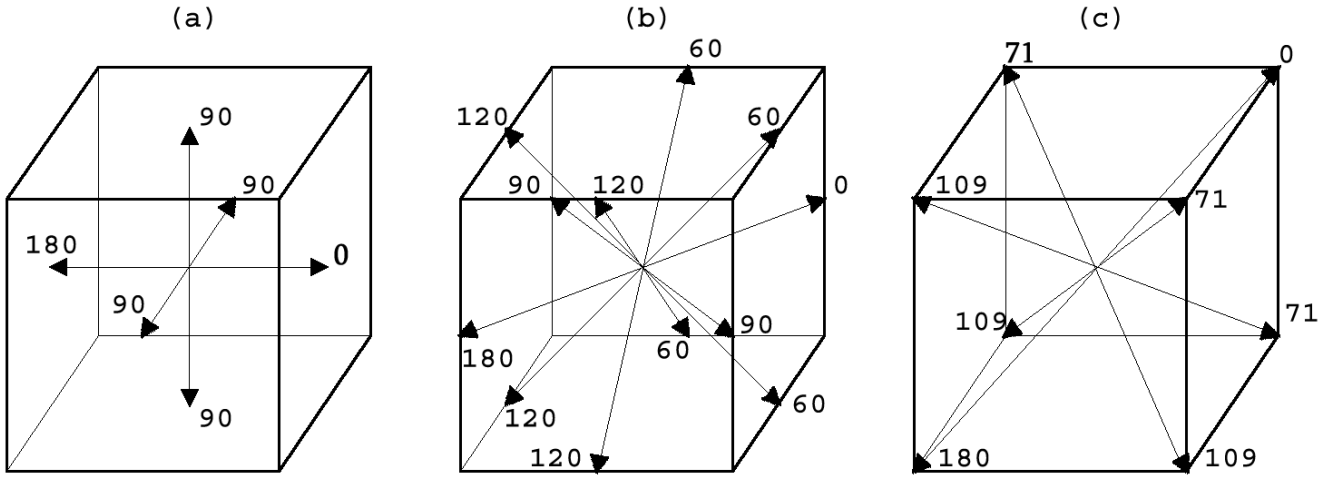

Figure 1.6: Values of spontaneous polarization for (a) tetragonal, (b) orthogonal and (c) rhombohedral symmetry. "0" indicates chosen value of polarization in one side of domain wall, other directions of spontaneous polarization are denoted by the angle between these polarization states.

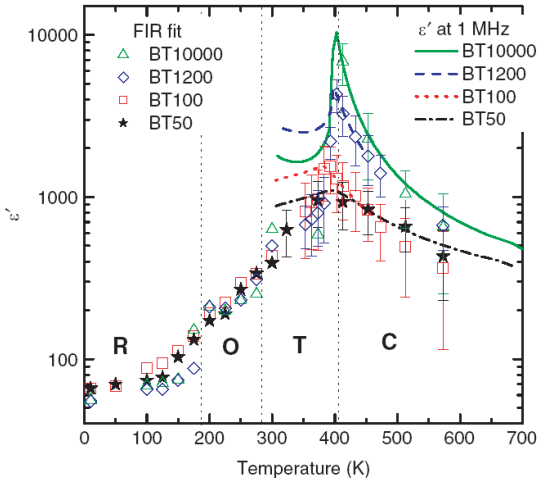

Figure 1.7: Real part of dielectric constant in $BaTiO_3$ ceramics. Size of grain is indicated in nanometers after short-hand BT standing for barium titanate. Symbols and lines represent data from reflectivity fit and dielectric measurements, resp. The discrepancy between data was ascribed to contribution from domain walls, which are included in static dielectric measurements, but not in reflectivity measurements. Figure was taken from Ref. [9].

tetragonal phase. Similar work of X. R. Huang and coauthors [34] deals with 90, 180 and 120 degree domain walls in orthorombic phase. S-wall was discussed in papers published by Janovec, Fousek and Erhart [17, 4, 35].

Simulation of domain structures in ferroelectric perovskites were performed by several groups:

S. Nambu and D. A. Sagala in the article [18] described Ginzburg-Landau-Devonshire model for simulation of evolution of domains. Model is defined in terms of polarization and deformation, which is further eliminated with use of mechanical equilibrium conditions (which was originaly suggested A.G. Khachaturyan [31]). They propose computation in direct space with use of integration kernel for long-range interactions. Electrostatic interaction is, however, not included.

H. L. Hu and L. Q. Chen [19, 20] made use of the method presented in [18]. Electrostatic dipole-dipole interaction is taken into account. Computation on mechanically clamped crystal is performed in Fourier space with use of semi-implicit method [32] that enables considerable increase of time-step.

Similar procedure was used by R. Ahluwaalia [21] to obtain hysteretic behavior under varying external electric field.

W. Zhang and K. Bhattacharya [24, 25] performed simulation in real space for polarization. Elastic field was treated separately and mechanical equilibrium conditions were obtained in each step by separate solving of elastic problem with use of FEM method. Local electric field is obtained by explicit solving of Poisson equation. This approach avoid transformation to Fourier space and therefore does not require periodicity of boundary conditions. Influence of nucleation on the shape of hysteresis curves was tested. Hysteresis of polarization and strain versus electric field is provided for material under different level of external stress.

1.4 Scope and brief overview of the thesis

The main objective of this work is to contribute to knowledge about domain walls and domain formation in ferroelectric material. Firstly, domain walls were inspected using analytical approach and symmetry considerations. Moreover, computational tool for numerical simulations of domain evolution in perovskite ferroelectric material was developed. Individual parts of the thesis were arranged into following chapters:

Introduction: Introduction and scope of the thesis, brief review of related works.

Generalized Ginzburg-Landau-Devonshire model: Definition and description of the model, parameters used in numerical and analytical computations. Elimination of heterogeneous part of the elastic field from the model.

Charge-free elastically compatible domain walls: Analytical description of domain wall profile and other properties. It is assumed that domain wall is of Ising type, charge-free and elastically compatible. Then it is possible to treat it within one-dimensional model which is solvable analytically. Mutually comparison of the walls is possible. Legitimacy of assumptions is discussed.

Dynamics of polarization field: Dynamics of polarization put together with lattice vibrations of optic modes. Soft mode concept is introduced.

Landau-Khalatnikov equation: Time dependent Landau-Khalatnikov equation that governs evolution of polarization is introduced. Variations of the free energy functional that appears at the right hand side of the equation are computed.

Implementation details of computer programs: Used numerical schemes are described. Description of the program for computation of evolution of polarization field are given. Possible configurations are described together with advantages and disadvantages of computation in Fourier space.

Examples of simulations: Several applications of developed program for computation of evolution of domain structure in ferroelectric material are described and discussed.

Conclusions: Conclusions and main results of the thesis.

Future work: Possible directions of future work.

Appendices: Additional information and algebraic calculations used in the thesis are provided. Fourier transform, variation of the free energy, elastostriction kernels, tensors and transformation of coordinates, compatibility relations, point groups.

Chapter 2

Generalized Ginzburg-Landau-Devonshire model

Continuous model is based on a definition of relevant thermodynamic potential. Important features of ferroelectrics – hysteresis (polarization vs. electric field), electrostriction, coupling of polarization and mechanical deformation in $BaTiO_3$ – require introduction of nonlinear terms to the thermodynamic potential [36, 5]. Following several preceding works [37, 18, 19, 20, 21], the excess[1] free energy is expanded in terms of powers of polarization components P_i, its derivatives $P_{i,j}$ and components of strain tensor $e_{ij} = \frac{1}{2}\left(\frac{\partial u_i}{\partial x_j} + \frac{\partial u_j}{\partial x_i}\right)$. Polarization and strain were taken as primary and secondary order parameters, respectively. This approach was firstly demonstrated on $BaTiO_3$ by Devonshire in [37]. The free energy

$$F\left[\{P_i, P_{i,j}, e_{ij}\}\right] = F_{\mathrm{LG}}^{(e)}\left[\{P_i, P_{i,j}\}\right] + F_{\mathrm{Cq}}\left[\{P_i, e_{ij}\}\right] + F_{\mathrm{dep}}\left[\{P_i\}\right] \tag{2.1}$$

consists of three parts: Ginzburg-Landau, Elastostriction and electrostatic part. Polarization is considered to be position-dependent $P_i = P_i(\mathbf{r})$. Ginzburg-Landau part

$$F_{\mathrm{LG}}^{(e)}\left[\{P_i, P_{i,j}\}\right] = \int \mathrm{d}\mathbf{r}\left[f_{\mathrm{L}}^{(e)}\left[\{P_i\}\right] + f_{\mathrm{G}}\left[\{P_{i,j}\}\right]\right] \tag{2.2}$$

represents mechanically clamped potential (denoted by superscript e – see Sec. 2.1) together with Ginzburg gradient part for energy increase due to variation of polarization. Elastostriction part

$$F_{\mathrm{Cq}}\left[\{P_i, e_{ij}\}\right] = \int \mathrm{d}\mathbf{r}\left[f_{\mathrm{C}}\left[\{P_i, e_{ij}\}\right] + f_{\mathrm{q}}\left[\{P_i, e_{ij}\}\right]\right] \tag{2.3}$$

stands for linear elastic and electrostriction energy as introduced by Devonshire in [37, 5]. Heterogeneous part of the elastic strain field can be eliminated assuming that its relaxation towards mechanical equilibrium is much faster then evolution of the polarization field [19] – heterogeneous strain can be determined from local mechanical equilibrium conditions given by Euler-Lagrange equation for deformation. Elimination of the heterogeneous strain is conveniently done in Fourier space by the procedure described for example in Sec. 2.3, where Ref. [18]

[1] The free energy is assumed to consist of two parts: energy of hypothetical cubic state, and energy arising from nonzero order parameters [26].

is followed. Finally, the contribution of electrostatic dipole-dipole interaction $F_{\mathrm{dep}}\left[\{P_i\}\right]$ to the free energy is taken into account in the form

$$F_{\mathrm{dep}}\left[\{P_i\}\right] = -\frac{1}{2}\int \mathrm{d}\mathbf{r}\left[\mathbf{E}_{\mathrm{dep}}(\mathbf{r})\cdot\mathbf{P}(\mathbf{r})\right], \tag{2.4}$$

where $\mathbf{E}_{\mathrm{dep}}$ is local electric field that consists of contribution from dipoles in the system, external electric field and free charges at the electrodes. (E_{dep} is referred to as depolarization field, because electric field originating from surface dipoles can cause decrease of polarization in a sample).

We considered the material as strained cubic in all phases, because depart of lattice parameters in tetragonal, orthorombic and rhombohedral phases are reasonably small and there is a group-subgroup relation between high paraelectric cubic and each ferroelectric point group. On the contrary, there is no such relation between individual ferroelectric point groups. Cubic symmetry of parent parelectric phase considerably simplifies involved tensors and constructed potential[2].

2.1 Landau-Devonshire potential

The Landau free energy functional is systematic expansion of local energy in terms of polarization components. First-order character of phase transitions in $BaTiO_3$ implies the expansion at least up to sixth[3] order in polarization

$$\begin{aligned} f_{\mathrm{L}}^{(\mathrm{e})}\left[\{P_i\}\right] \;=\; & \alpha_1\left(P_1^2+P_2^2+P_3^2\right) \\ & +\alpha_{11}^{(\mathrm{e})}\left(P_1^4+P_2^4+P_3^4\right) \\ & +\alpha_{12}^{(\mathrm{e})}\left(P_1^2P_2^2+P_2^2P_3^2+P_1^2P_3^2\right) \\ & +\alpha_{111}\left(P_1^6+P_2^6+P_3^6\right) \\ & +\alpha_{112}\left(P_1^4(P_2^2+P_3^2)+P_2^4(P_1^2+P_3^2)+P_3^4(P_1^2+P_2^2)\right) \\ & +\alpha_{123}P_1^2P_2^2P_3^2\ . \end{aligned} \tag{2.6}$$

Coefficient $\alpha_1(T)$ is reciprocal susceptibility for zero polarization and is linearly temperature dependent in accordance with Curie-Weiss law which states that temperature dependence of

[2]For particular materials it is necessary to choose appropriate terms of the free energy functional according to the substance under consideration. For example the electristriction is important in ferroelectrics, while magnetostriction in ferromagnetic materials can be negligible. Electrostatic interaction would be suppressed by the presence of free charge carriers that screen local electric fields.

[3]Landau potential is also expanded up to higher orders in order to obtain realistic phase diagram, especially for big strains. Eight order terms in polarization are added to Eqn. 2.6

$$\begin{aligned} & +\alpha_{1111}\left(P_1^8+P_2^8+P_3^8\right) \\ & +\alpha_{1112}\left(P_1^6(P_2^2+P_3^2)+P_2^6(P_1^2+P_3^2)+P_3^6(P_1^2+P_2^2)\right) \\ & +\alpha_{1122}\left(P_1^4P_2^4+P_2^4P_3^4+P_1^4P_3^4\right) \\ & +\alpha_{1123}\left(P_1^4P_2^2P_3^2+P_2^4P_1^2P_3^2+P_3^4P_1^2P_2^2\right)\ . \end{aligned} \tag{2.5}$$

Recently, there have been published stress-free Landau expansion coefficients up to eighth order for $BaTiO_3$ [12] rendered out of phase diagram of the material under large compressive strain. The only temperature-dependent coefficient is $\alpha_1(T)$.

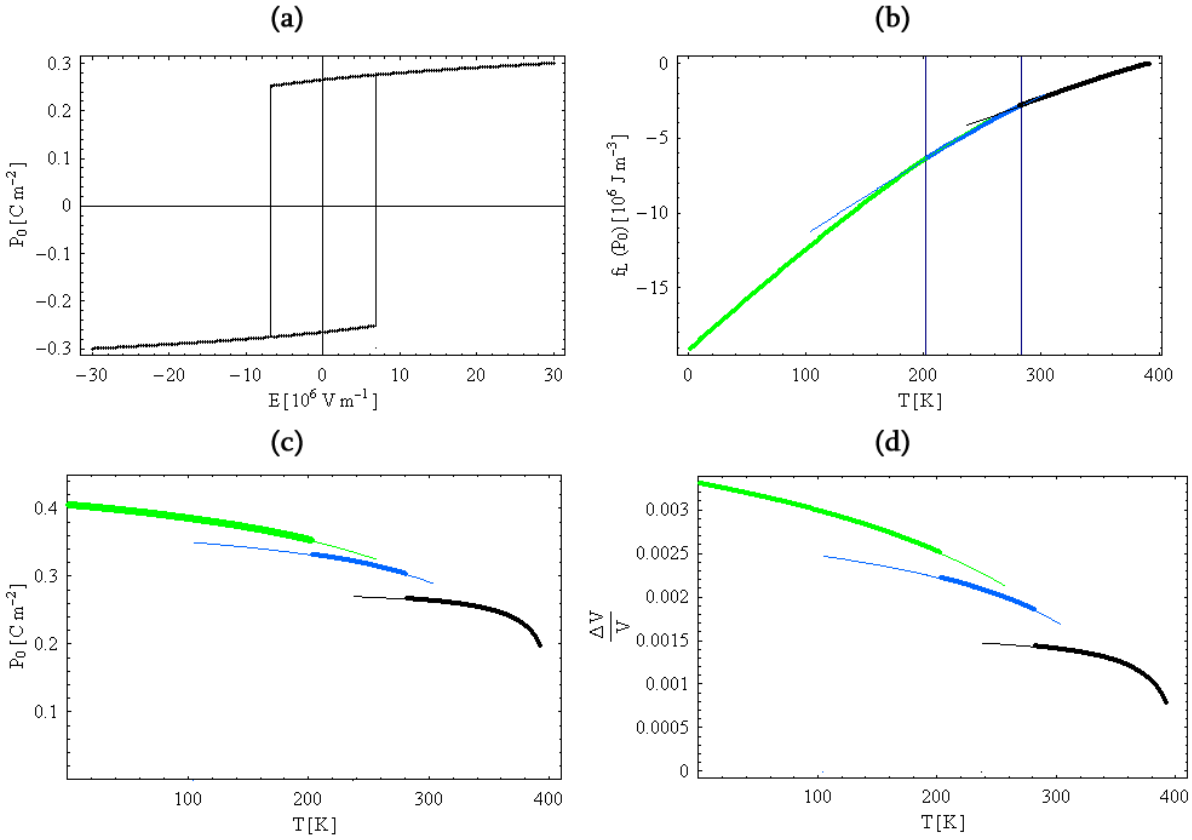

Figure 2.1: (a) Hysteresis in one-dimensional Landau potential constructed for $P_2 = 0$, $P_3 = 0$ with electric field applied along x-direction. (b) Values of minima for tetragonal (black), orthogonal (blue) and rhombohedral (green) phase. Temperature of phase transition is indicated by vertical lines. (c) Value of spontaneous polarization in individual phases. (d) Relative increase of volume in individual phases. Parameters are taken from parameter set "A" in Tab. 2.2.

the susceptibility above the transition point (in cubic state) is $\chi = \chi_0 + \frac{C}{T-T_c}$. In the field of ferroelectrics, where dielectric constant can reach extremely high values, relatively small constant χ_0 coming from electronic polarizability is omitted. Other coefficients can, but might not be temperature dependent.

Sequence of phase transitions in the crystal is given by changes of a position of the absolute minima of the corresponding Landau potential. The Landau energy expansion for cubic symmetry of parent[4] paralelectric phase reads[5]:

Sixth-order expansion (given by the parameter set "A" in Tab. 2.1) is used in analytical and numerical computations in this thesis. Detailed discussion of the shape of sixth-order stress-free Landau potential was given in [13] together with temperature versus electric field phase diagrams. The authors found $\alpha_1(T)$, $\alpha_{11}(T)$ and $\alpha_{111}(T)$ dependence on temperature in the form

$$\alpha_1(T) \quad = \quad 3.34 \times 10^5 \ (T - 381)$$

[4]Tetragonal (C_{4v}), orthorombic (C_{2v}) and rhombohedral (C_{3v}) point groups are subgroups of cubic (O_h) group. However, group subgroup relation does not appear between any two of C_{4v}, C_{2v} and C_{3v} point groups.

[5]In literature, there also appears Landau potential with isotropic coefficient α_{11}.

$$\begin{aligned} \alpha_{11}(T) &= 4.69 \times 10^6 \ (T - 393) - 2.02 \times 10^8 \\ \alpha_{111}(T) &= -5.52 \times 10^7 \ (T - 393) + 2.76 \times 10^9 \ . \end{aligned} \tag{2.7}$$

There are six equivalent states of spontaneous polarization in tetragonal phase, twelve in orthorombic and eight in rhombohedral. They are indicated schematically in Fig. 1.6(a,b,c). Phase transitions are of first-order, therefore minima for a given phase survive even below and above phase transition. Range of existence of minima of all phases in stress-free Landau potential (inspected by negative definitivity of the hessian matrix) are plotted in Fig. 2.1(c). Minima corresponding to tetragonal phase exist for given Landau potential approximately between 237 K and 393 K, orthorombic phase between 104 K and 303 K and rhombohedral phase between 0 K and 256 K. Transition temperatures for this potential are approximately 392 K (C→T), 283 K (T→O) and 202 K (O→R).

The contribution of the elastic field to the free energy is introduced through linear elastic energy

$$\begin{aligned} f_{\mathrm{C}}\left[\{e_{ij}\}\right] &= \frac{1}{2} e_\rho C_{\rho\sigma} e_\sigma \\ &= \frac{1}{2} C_{11}(e_{11}^2 + e_{22}^2 + e_{33}^2) \\ &\quad + C_{12}(e_{22}e_{33} + e_{11}e_{33} + e_{11}e_{22}) \\ &\quad + 2C_{44}(e_{23}^2 + e_{13}^2 + e_{12}^2) \ . \end{aligned} \tag{2.8}$$

Electrostriction energy reads

$$\begin{aligned} f_{\mathrm{q}}\left[\{P_i, e_{ij}\}\right] &= -q_{ijkl} e_{ij} P_k P_l \\ &= -q_{11}(e_{11}P_1^2 + e_{22}P_2^2 + e_{33}P_3^2) \\ &\quad - q_{12}(e_{11}(P_2^2 + P_3^2) + e_{22}(P_1^2 + P_3^2) + e_{33}(P_1^2 + P_2^2)) \\ &\quad - 2q_{44}(e_{12}P_1P_2 + e_{13}P_1P_3 + e_{23}P_2P_3) \\ &= -\sum_{\rho=1}^{6} e_\rho g_\rho \ . \end{aligned} \tag{2.9}$$

Here $C_{\alpha\beta}$ and $q_{\alpha\beta}$ are components of elastic and electrostriction tensor in Voigt notation, $C_{11} = C_{1111}$, $C_{12} = C_{1122}$,$C_{44} = C_{1212}$, $q_{11} = q_{1111}$, $a_{12} = q_{1122}$, but $q_{44} = 2q_{1122}$. Electrostriction stress components g_ρ are defined

$$\begin{aligned} g_1 &= q_{11}P_1^2 + q_{12}P_2^2 + q_{12}P_3^2 \\ g_2 &= q_{12}P_1^2 + q_{11}P_2^2 + q_{12}P_3^2 \\ g_3 &= q_{12}P_1^2 + q_{12}P_2^2 + q_{11}P_3^2 \\ g_4 &= q_{44}P_2P_3 \\ g_5 &= q_{44}P_1P_3 \\ g_6 &= q_{44}P_1P_2 \ . \end{aligned} \tag{2.10}$$

The equilibrium elastic homogeneous state in applied homogeneous stress $\overline{\sigma}$ and local electric field $\mathbf{E}(\mathbf{r})$ is obtained by minimization of the free energy functional with respect to the

Table 2.1: Complete sets of parameters used in the phenomenological GGLD model for $BaTiO_3$. Set "A" was derived in Ref. [26], and is used for computations throughout this thesis. Set "B" is the same except for Landau coefficients, which are taken from Ref. [12]. Set "C" corresponds to parameters use in H.-L. Hu and L.-Q. Chen [20] for three-dimensional numerical simulations († the coefficient α_{11} was repaired in order to reach spontaneous value of polarization given in cited article). Set "D" are coefficients from W. Zhang and K. Bhattacharya [24]. Electrostriction coefficients Q_{ij} are not independent and can be evaluated using Eqn. 2.14.

Parameter	A	B	C	D	Unit [SI]
α_1	-2.772	-3.712	-3.712	-5.178	$10^7\ \mathrm{J\,m\,C^{-2}}$
α_{11}	-6.476	-2.097	-2.790†	4.924	$10^8\ \mathrm{J\,m^5\,C^{-4}}$
$\alpha_{11}^{(e)}$	1.701	6.079	-2.745	–	$10^8\ \mathrm{J\,m^5\,C^{-4}}$
α_{12}	3.230	7.974	49.45	19.695	$10^8\ \mathrm{J\,m^5\,C^{-4}}$
$\alpha_{12}^{(e)}$	-3.441	1.303	49.41	–	$10^8\ \mathrm{J\,m^5\,C^{-4}}$
α_{111}	8.004	1.294	6.497	14.081	$10^9\ \mathrm{J\,m^9\,C^{-6}}$
α_{112}	4.470	-1.950	32.48	–	$10^9\ \mathrm{J\,m^9\,C^{-6}}$
α_{123}	4.910	-2.500	8.121	–	$10^9\ \mathrm{J\,m^9\,C^{-6}}$
α_{1111}	–	3.863	–	–	$10^{10}\ \mathrm{J\,m^{13}\,C^{-8}}$
α_{1112}	–	2.529	–	–	$10^{10}\ \mathrm{J\,m^{13}\,C^{-8}}$
α_{1122}	–	1.637	–	5985.810	$10^{10}\ \mathrm{J\,m^{13}\,C^{-8}}$
α_{1123}	–	1.367	–	–	$10^{10}\ \mathrm{J\,m^{13}\,C^{-8}}$
G_{11}	51	51	51	51	$10^{-11}\ \mathrm{J\,m^3\,C^{-2}}$
G_{14}	0	0	0	0	$10^{-11}\ \mathrm{J\,m^3\,C^{-2}}$
G_{44}	2	2	51	51	$10^{-11}\ \mathrm{J\,m^3\,C^{-2}}$
q_{11}	14.20	14.20	0.00527	10.56	$10^9\ \mathrm{J\,m\,C^{-2}}$
q_{12}	-0.74	-0.74	-0.000275	-1.37	$10^9\ \mathrm{J\,m\,C^{-2}}$
q_{44}	1.57	1.57	0.000582	5.97	$10^9\ \mathrm{J\,m\,C^{-2}}$
C_{11}	27.50	27.50	0.000690	185	$10^{10}\ \mathrm{J\,m^{-3}}$
C_{12}	17.90	17.90	0.000449	111	$10^{10}\ \mathrm{J\,m^{-3}}$
C_{44}	5.43	5.43	0.000135	37	$10^{10}\ \mathrm{J\,m^{-3}}$
$\epsilon_{\mathbf{B}}$	7.35	7.35	1	1	
Q_{11}	0.1104	0.1104	0.1104	0.0114	$\mathrm{m^4\,C^{-2}}$
Q_{12}	-0.0452	-0.0452	-0.0452	-0.0047	$\mathrm{m^4\,C^{-2}}$
Q_{44}	0.0289	0.0289	0.0289	0.0016	$\mathrm{m^4\,C^{-2}}$

Table 2.2: List of parameters of sixth-order Landau potential for characteristic temperatures of individual ferroelectric phases in $BaTiO_3$. Set "B" is derived by Bell in [13]. Temperature dependent coefficients are given in Eqn. 2.7. $\alpha_{11}^{(e)}$ and $\alpha_{12}^{(e)}$ are renormalized according to Eqn. 2.16 and Eqn. 2.17, resp.

Landau coefficient	298 K	208 K	118 K	Unit [SI]
α_1	-2.772	-5.778	-8.784	10^7 J m C^{-2}
α_{11}	-6.476	-10.697	-14.918	10^8 J m^5 C^{-4}
$\alpha_{11}^{(e)}$	1.701	-2.520	-6.741	10^8 J m^5 C^{-4}
α_{12}	3.230	3.230	3.230	10^8 J m^5 C^{-4}
$\alpha_{12}^{(e)}$	-3.441	-3.441	-3.441	10^8 J m^5 C^{-4}
α_{111}	8.004	12.972	17.940	10^9 J m^9 C^{-6}
α_{112}	4.470	4.470	4.470	10^9 J m^9 C^{-6}
α_{123}	4.910	4.910	4.910	10^9 J m^9 C^{-6}

polarization and strain components [26]

$$\frac{\partial}{\partial P_i}\left(f_{\mathrm{L}}^{(e)} + f_{\mathrm{C}} + f_{\mathrm{q}} - \overline{\sigma}\cdot\overline{e} - \mathbf{E}\cdot\mathbf{P}\right) = 0 \tag{2.11}$$

$$\frac{\partial}{\partial e_{ij}}\left(f_{\mathrm{L}}^{(e)} + f_{\mathrm{C}} + f_{\mathrm{q}} - \overline{\sigma}\cdot\overline{e} - \mathbf{E}\cdot\mathbf{P}\right) = 0\ . \tag{2.12}$$

The convention is that negative values means pressure, and positive values stand for traction. Similarly for strain tensor e, negative and positive values represent compression and expansion, respectively. Equation for stress-free ($\sigma = 0$) deformation at zero electric field for homogeneous sample follows immediately from Eqn. 2.12

$$\begin{aligned} e_1 &= Q_{11}P_1^2 + Q_{12}P_2^2 + Q_{12}P_3^2 \\ e_2 &= Q_{12}P_1^2 + Q_{11}P_2^2 + Q_{12}P_3^2 \\ e_3 &= Q_{12}P_1^2 + Q_{12}P_2^2 + Q_{11}P_3^2 \\ e_4 &= Q_{44}P_2P_3 \\ e_5 &= Q_{44}P_1P_3 \\ e_6 &= Q_{44}P_1P_2\ . \end{aligned} \tag{2.13}$$

Mechanical deformation is proportional to square of polarization. Components of electrostriction tensor $Q_{\alpha\beta}$ are defined as

$$\begin{aligned} Q_{11} &= \frac{1}{3}\left[\frac{\hat{q}_{11}}{\hat{C}_{11}} + 2\frac{\hat{q}_{22}}{\hat{C}_{22}}\right] = \frac{C_{11}q_{11} + C_{12}q_{11} - 2C_{12}q_{12}}{(C_{11}-C_{12})(C_{11}+2C_{12})} \\ Q_{12} &= \frac{1}{3}\left[\frac{\hat{q}_{11}}{\hat{C}_{11}} - \frac{\hat{q}_{22}}{\hat{C}_{22}}\right] = \frac{C_{11}q_{12} - C_{12}q_{11}}{(C_{11}-C_{12})(C_{11}+2C_{12})} \\ Q_{44} &= \frac{q_{44}}{C_{44}} \end{aligned} \tag{2.14}$$

with constants

$$\begin{aligned}\hat{C}_{11} &= C_{11}+2C_{12}\\ \hat{C}_{11} &= C_{11}-C_{12}\\ \hat{q}_{11} &= q_{11}+2q_{12}\\ \hat{q}_{11} &= q_{11}-q_{12}\ .\end{aligned} \tag{2.15}$$

Substitution Eqn. 2.13 into $F_{\mathrm{L}}\left[\{P_i\}\right]+F_{\mathrm{Cq}}\left[\{P_i,e_{ij}\}\right]$ leads to the expression for the free energy of homogeneous sample dependent only on polarization. It has the same form as F_{L} with coefficients $\alpha_{11}^{(e)}$, $\alpha_{12}^{(e)}$ instead of α_{11}, α_{12}, resp. The renormalization has the form [18, 37]

$$\begin{aligned}\alpha_{11} &= \alpha_{11}^{(e)}-\frac{1}{6}\left[\frac{\hat{q}_{11}^2}{\hat{C}_{11}}+2\frac{\hat{q}_{22}^2}{\hat{C}_{22}}\right]\\ &= \alpha_{11}^{(e)}-\frac{c_{12}q_{11}(q_{11}-4q_{12})+c_{11}(q_{11}^2+2q_{12}^2)}{2(C_{11}-C_{12})(C_{11}+2C_{12})}\end{aligned} \tag{2.16}$$

$$\begin{aligned}\alpha_{12} &= \alpha_{12}^{(e)}-\frac{1}{6}\left[2\frac{\hat{q}_{11}^2}{\hat{C}_{11}}-2\frac{\hat{q}_{22}^2}{\hat{C}_{22}}+3\frac{q_{44}^2}{C_{44}}\right]\\ &= \alpha_{12}^{(e)}-\left[\frac{C_{11}q_{12}(2q_{11}+q_{12})+c_{12}(q_{11}^2+2q_{12}^2)}{2(C_{11}-C_{12})(C_{11}+2C_{12})}+\frac{1}{2}\frac{q_{44}^2}{C_{44}}\right]\ .\end{aligned} \tag{2.17}$$

Coefficients α_{11} and α_{12} are Landau coefficients for stress-free crystal presented in Ref. [13, 12]. We use them to get constants for mechanically clamped crystal $\alpha_{11}^{(e)}$ and $\alpha_{12}^{(e)}$. Shapes of clamped and stress-free crystal can differ significantly. In Fig. 2.2 there are printed clamped and stress-free potentials for $P_z=0$. Stress-free potential minimum is tetragonal as expected, but clamped potential has its minimum at orthorombic positions.

2.2 Ginzburg gradient contribution to the free energy

Generally, the polarization varies with position in space, $\mathbf{P}=\mathbf{P}(\mathbf{r})$. We assume that polarization components $P_1(\mathbf{r})$, $P_2(\mathbf{r})$, $P_3(\mathbf{r})$ are differentiable functions of position up to second derivatives. Ginzburg contribution to the energy functional from weakly nonlocal interaction is given by quadratic form in polarization gradients for cubic symmetry

$$\begin{aligned}f_{\mathrm{G}}\left[\{P_{i,j}\}\right] &= \frac{1}{2}G_{ijkl}P_{i,j}P_{k,l}\\ &= \frac{1}{2}G_{11}(P_{1,1}^2+P_{2,2}^2+P_{3,3}^2)\\ &\quad +G_{14}(P_{1,1}P_{2,2}+P_{2,2}P_{3,3}+P_{1,1}P_{3,3})\\ &\quad +\frac{1}{2}G_{44}\left(P_{1,2}^2+P_{2,1}^2+P_{2,3}^2+P_{3,2}^2+P_{3,1}^2+P_{1,3}^2\right)\ .\end{aligned} \tag{2.18}$$

The tensorial expression was introduced and explained in Ref. [26]. For cubic symmetry $G_{11}=G_{1111}$, $G_{12}=G_{1122}$ and $G_{44}=G_{1212}$. Tensorial form proves useful for transformation of tensor components into new coordinate systems: G_{ijkl} has the same transformation properties as tensor of elastic constants C_{ijkl} in Eqn. E.5).

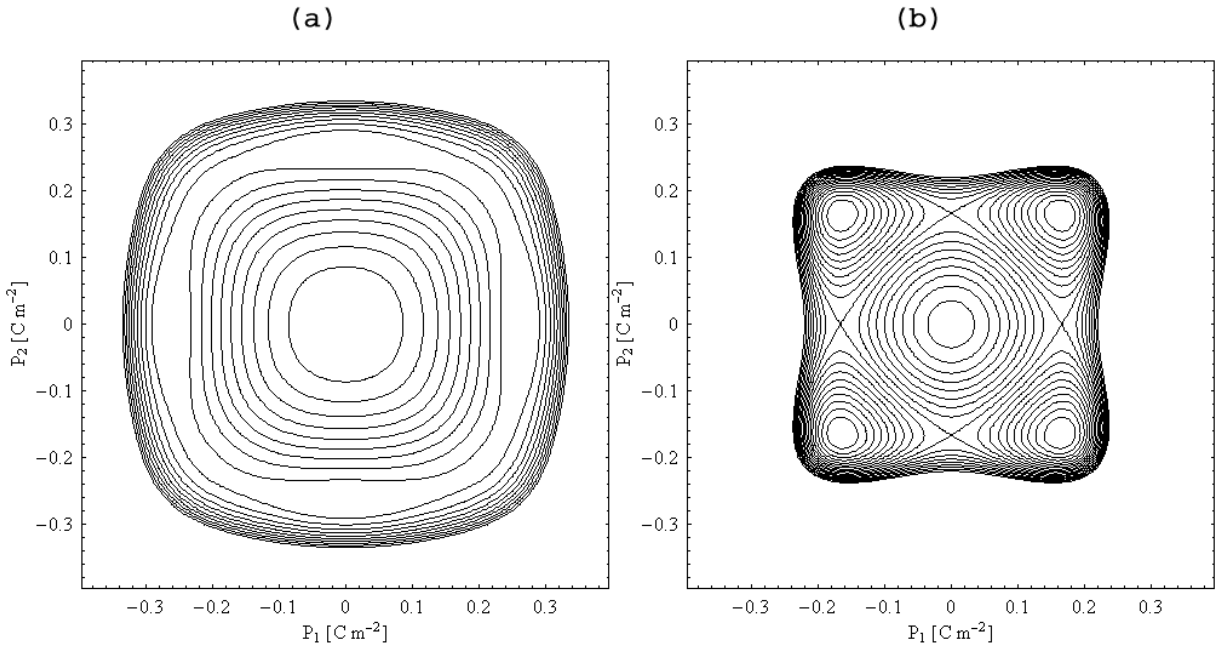

Figure 2.2: Negative values of Landau potential with coefficients according to parameter set "A" from Tab. 2.2 for 298 K. (a) Stress-free Landau potential in tetragonal phase. (b) Clamped Landau potential in tetragonal phase phase has orthorombic minima. Contours are distributed linearly.

It it worth noting that expression for gradient energy appears in several equivalent forms in literature. Most common forms are

$$\begin{aligned} f_{\mathrm{G}}\left[\{P_{i,j}\}\right] &= \frac{1}{2}G_{11}(P_{1,1}^2+P_{2,2}^2+P_{3,3}^2) \\ &\quad +G_{12}(P_{1,1}P_{2,2}+P_{2,2}P_{3,3}+P_{1,1}P_{3,3}) \\ &\quad +\frac{1}{2}G_{44}\left((P_{1,2}+P_{2,1})^2+(P_{2,3}+P_{3,2})^2+(P_{3,1}+P_{1,3})^2\right)\ , \end{aligned} \tag{2.19}$$

where $G_{14}=G_{12}+G_{44}$, and

$$\begin{aligned} f_{\mathrm{G}}\left[\{P_{i,j}\}\right] &= \frac{1}{2}G_{11}(P_{1,1}^2+P_{2,2}^2+P_{3,3}^2) \\ &\quad +H_{12}(P_{1,1}P_{2,2}+P_{2,2}P_{3,3}+P_{1,1}P_{3,3}) \\ &\quad +\frac{1}{2}H_{44}\left((P_{1,2}+P_{2,1})^2+(P_{2,3}+P_{3,2})^2+(P_{3,1}+P_{1,3})^2\right) \\ &\quad +\frac{1}{2}H'_{44}\left((P_{1,2}-P_{2,1})^2+(P_{2,3}-P_{3,2})^2+(P_{3,1}-P_{1,3})^2\right)\ . \end{aligned} \tag{2.20}$$

Here $G_{44}=H_{44}+H'_{44}$ and $G_{14}=H_{12}+H_{44}-H'_{44}$. Previous relations hold thanks to the equality of volume integrals $P_{1,2}P_{2,1}$ and $P_{1,1}P_{2,2}$ in infinite or periodic sample. The former is case of analytic considerations, the latter holds in simulations in periodic space.

It is usually taken for granted [20, 24] that the gradient energy is isotropic[6]. However, in Ref. [26] there was shown that the anisotropy of gradient energy play crucial role in domain formation and evolution process in perovskites.

[6]Gradient energy is isotropic if the coefficients fulfil following condition: $G_{14}=0$ and $G_{44}=G_{11}$.

Even if the gradient energy is isotropic, there can be certain direction of domain walls selected by elastic compatibility conditions. Elastically permissible orientations of walls are discussed in Sec. 3.1).

The gradient energy acts only on inhomogeneous part of polarization and is zero for uniform polarization field.

2.3 Elastic long-range interaction

Ginzburg-Landau-Devonshire potential introduced by the Eqn. 2.1 is defined in terms polarization and strain field. Strain can be split into two parts: homogeneous macroscopic strain $\overline{e}_{ij}$ and heterogeneous strain with zero spatial average $\delta e_{ij}(\mathbf{r})$ which satisfies

$$\int \mathrm{d}\mathbf{r}\ \delta \mathbf{e}_{ij}(\mathbf{r}) = 0\ . \tag{2.21}$$

Homogeneous strain $\overline{e}_{ij}$ is defined by the condition

$$e_{ij}(\mathbf{r}) = \overline{e}_{ij} + \delta e_{ij}(\mathbf{r}) \tag{2.22}$$

and is controlled by macroscopic boundary conditions discussed in Sec. 2.4.

The heterogeneous part of the elastic strain field can be usually eliminated assuming that its relaxation towards mechanical equilibrium is much faster then evolution of the inhomogeneities of the polarization field [19, 18]. In this case, heterogeneous strain is determined from local mechanical equilibrium conditions given by Euler-Lagrange equation

$$\sum_{j=1}^{3} \frac{\partial \sigma_{ij}}{\partial x_j} = \sum_{j=1}^{3} \frac{\partial}{\partial x_j} \left(\frac{\partial f_{\mathrm{Cq}}}{\partial u_{ij}} \right) = 0\ . \tag{2.23}$$

Elimination can be conveniently done using the Fourier transform (defined by relations in (B.1)) of the displacement field components $u_i(\mathbf{r})$ and electrostriction stress components $g_{ij}(\mathbf{r})$.

$$\begin{aligned} u_i(\mathbf{k}) &= \int \mathrm{d}\mathbf{r}\ u_i(\mathbf{r}) e^{-i\mathbf{kr}} \\ g_{ij}(\mathbf{k}) &= \int \mathrm{d}\mathbf{r}\ g_{ij}(\mathbf{r}) e^{-i\mathbf{kr}} \end{aligned} \tag{2.24}$$

Fourier components of the instantaneous equilibrium strain field are expressed in terms of $g_{ij}(\mathbf{k})$ and the directional cosines $\hat{\mathbf{k}} = \mathbf{k}/|\mathbf{k}|$ as follows:

$$u_j(\mathbf{k}) = -\frac{i}{k} \left[\frac{G_j(\mathbf{k})}{d_j} - \frac{D(\hat{\mathbf{k}}) H(\mathbf{k}) \hat{k}_j}{d_j} \right]\ , \tag{2.25}$$

where

$$G_i(\mathbf{k}) \ = \ \sum_{j=1}^{3} \hat{k}_j g_{ij}(\mathbf{k}) \tag{2.26}$$

$$
\begin{aligned}
H(\mathbf{k}) &= \sum_{i=1}^{3} \hat{k}_i G_i(\mathbf{k})/d_i && (2.27)\\
D(\hat{\mathbf{k}}) &= (C_{12}+C_{44})/(1+(C_{12}+C_{44})\,\chi(\hat{\mathbf{k}})) && (2.28)\\
\chi(\hat{\mathbf{k}}) &= \sum_{i} \hat{k}_i^2/d_i && (2.29)\\
d_i(\hat{\mathbf{k}}) &= C_{44}\left(1+\xi\hat{k}_i^2\right) && (2.30)\\
\xi &= (C_{11}-C_{12}-2C_{44})/C_{44}\ . && (2.31)
\end{aligned}
$$

After the substitution of the backward-Fourier-transformed elastic displacement field into the expression for electrostriction and elastic energies we finally get an elastostriction energy (without explicit dependence on elastic field)

$$F'_{\mathrm{Cq}}\left[\{P_i\}\right] = F'_{\mathrm{C}}\left[\{P_i\}\right] + F'_{\mathrm{q}}\left[\{P_i\}\right] = -\frac{1}{2}\frac{1}{(2\pi)^3}\sum_{\rho}\sum_{\sigma}\int \mathrm{d}\mathbf{k}\left[\mathbf{B}_{\rho\sigma}(\hat{\mathbf{k}})g_\rho(\mathbf{k})g_\sigma(-\mathbf{k})\right]\ . \quad (2.32)$$

The matrix $\mathbf{B}(\hat{\mathbf{k}})$ reads

$$B_{\rho\sigma}(\hat{\mathbf{k}}) = \beta_{\rho\sigma}(\hat{\mathbf{k}}) - D(\hat{\mathbf{k}})\theta_\rho(\hat{\mathbf{k}})\theta_\sigma(\hat{\mathbf{k}})\ , \quad (2.33)$$

and its components $\beta_{\rho\sigma}$ and $\theta_\sigma(\hat{\mathbf{k}})$ depend on directional cosines only (see also Ref. [38]).

$$
\begin{aligned}
\beta &= \begin{bmatrix}
\hat{k}_x^2/d_x & 0 & 0 & 0 & \hat{k}_x\hat{k}_z/d_x & \hat{k}_x\hat{k}_y/d_x\\
0 & \hat{k}_y^2/d_y & 0 & \hat{k}_y\hat{k}_z/d_y & 0 & \hat{k}_x\hat{k}_y/d_y\\
0 & 0 & \hat{k}_z^2/d_z & \hat{k}_y\hat{k}_z/d_z & \hat{k}_x\hat{k}_z/d_z & 0\\
0 & \hat{k}_y\hat{k}_z/d_y & \hat{k}_y\hat{k}_z/d_z & \hat{k}_y^2/d_z+\hat{k}_z^2/d_y & \hat{k}_x\hat{k}_y/d_z & \hat{k}_x\hat{k}_z/d_y\\
\hat{k}_x\hat{k}_z/d_x & 0 & \hat{k}_x\hat{k}_z/d_z & \hat{k}_x\hat{k}_y/d_z & \hat{k}_x^2/d_z+\hat{k}_z^2/d_x & \hat{k}_y\hat{k}_z/d_x\\
\hat{k}_x\hat{k}_y/d_x & \hat{k}_x\hat{k}_y/d_y & 0 & \hat{k}_x\hat{k}_z/d_y & \hat{k}_y\hat{k}_z/d_x & \hat{k}_x^2/d_y+\hat{k}_y^2/d_x
\end{bmatrix}\\
\theta_1 &= \hat{k}_x^2/d_x\\
\theta_2 &= \hat{k}_y^2/d_y\\
\theta_3 &= \hat{k}_z^2/d_z\\
\theta_4 &= \hat{k}_y\hat{k}_z\,(1/d_y+1/d_z)\\
\theta_5 &= \hat{k}_x\hat{k}_z\,(1/d_x+1/d_z)\\
\theta_6 &= \hat{k}_x\hat{k}_y\,(1/d_x+1/d_y)\ . && (2.34)
\end{aligned}
$$

Once the $F_{\mathrm{C}}\left[\{e_{ij}\}\right] + F_{\mathrm{q}}\left[\{P_i, e_{ij}\}\right]$ terms in the Ginzburg-Landau-Devonshire free energy functional are replaced by the above expression for quasi-equilibrium elastostriction energy $F'_{\mathrm{Cq}}\left[\{P_i\}\right]$, the total Free energy depends on polarization field only:

$$F' = F'\left[\{P_i, P_{i,j}\}\right]\ . \quad (2.35)$$

Long-range nature of elastostriction interaction appears after transformation from Fourier to the direct space [18]

$$F'_{\mathrm{Cq}}\left[\{P_i\}\right] = -\frac{1}{2}\iint d\mathbf{r}d\mathbf{s}\sum_{\rho=1}^{6}\sum_{\sigma=1}^{6}\Psi_{\rho\sigma}(\mathbf{r}-\mathbf{s})Y_\rho(\mathbf{s})Y_\sigma(\mathbf{r})\ , \quad (2.36)$$

where

$$\Psi_{\rho\sigma}(\mathbf{R}) = \frac{1}{(2\pi)^3}\int d\mathbf{k}\; A_{\rho\sigma}(\hat{\mathbf{k}}) exp\left(-i\mathbf{k}\cdot\mathbf{R}\right) \tag{2.37}$$

is backward Fourier transform of kernels $A_{\rho\sigma}(\hat{\mathbf{k}})$, which are linear combinations of $B_{\rho\sigma}(\hat{\mathbf{k}})$ (definitions of $A_{\rho\sigma}(\hat{\mathbf{k}})$ are given in Sec. D), and the vector $\mathbf{Y}$ is defined as

$$\mathbf{Y} = \left[P_1^2, P_2^2, P_3^2, P_2P_3, P_1P_3, P_1P_2\right] \ . \tag{2.38}$$

in reciprocal as well as in direct space.

2.4 Homogeneous strain and stress

The model enables to control mechanical boundary conditions of the sample in two ways: either by mechanical clamping (where the homogeneous part of elastic deformation is fixed), or by external mechanical stress. Although perfect mechanical clamping is never available in real experiments, it can still be pertinent approximation of external conditions in some cases.

Homogeneous stress $\overline{\sigma}$ consists of two contributions: external stress and internal homogeneous stress rising from electromechanical coupling in the sample

$$\overline{\sigma}_{ij} = \overline{\sigma}_{ij}^{\mathrm{ext}} + \overline{\sigma}_{ij}^{\mathrm{int}} \ . \tag{2.39}$$

Internal stress is attained according to Hook's law

$$\overline{\sigma}_{ij}^{\mathrm{int}} = C_{ijkl}\overline{e}_{kl}^{\mathrm{int}} \ , \tag{2.40}$$

where homogeneous strain comes from average squared polarization

$$\begin{array}{lll} \overline{e}_{ii}^{\mathrm{int}} = & Q_{11}\overline{P_i^2} + Q_{12}\overline{P_j^2} + Q_{12}\overline{P_k^2} & \text{for } \ i \neq j \neq k \\ \overline{e}_{ij}^{\mathrm{int}} = & \frac{1}{2}Q_{44}\overline{|P_i|}\,\overline{|P_j|} & \text{for } \ i \neq j \ . \end{array} \tag{2.41}$$

Crystal, loaded by stress $\overline{\sigma}$, changes macroscopically its shape according to the inverse Hook's law. Note that strain in principal axes as well as shear strain is possible.

Equilibrium is given by Eqn. 2.12, where $\overline{\sigma}$ is not necessarily zero. Strain is expressed in terms of polarization and homogeneous stress and substituted back into the free energy functional. During derivation of these dependencies there appear additional contributions to the free energy.
Firstly, coefficient α_1 is renormalized and turns anisotropic

$$\begin{array}{rcl} \alpha_{1x} &=& \alpha_1 - (Q_{11}\overline{\sigma}_{xx} + Q_{12}(\overline{\sigma}_{yy} + \overline{\sigma}_{zz})) \\ \alpha_{1y} &=& \alpha_1 - (Q_{11}\overline{\sigma}_{yy} + Q_{12}(\overline{\sigma}_{xx} + \overline{\sigma}_{zz})) \\ \alpha_{1z} &=& \alpha_1 - (Q_{11}\overline{\sigma}_{zz} + Q_{12}(\overline{\sigma}_{xx} + \overline{\sigma}_{yy})) \ . \end{array} \tag{2.42}$$

Secondly, there appear new expressions connected with shear stress, that were originally forbidden in cubic Landau expansion.

$$f_{\mathrm{L}}^{(\mathrm{e})\prime}\left[\{P_i\}\right] \;=\; f_{\mathrm{L}}^{(\mathrm{e})}\left[\{P_i\}\right] + \beta_x P_2P_3 + \beta_y P_1P_3 + \beta_z P_1P_2 \ , \tag{2.43}$$

where anisotropic β_x, β_y and β_x are

$$\begin{aligned} \beta_x &= -\frac{q_{44}\overline{\sigma}_{23}}{C_{44}} \\ \beta_y &= -\frac{q_{44}\overline{\sigma}_{13}}{C_{44}} \\ \beta_z &= -\frac{q_{44}\overline{\sigma}_{12}}{C_{44}} \end{aligned} \tag{2.44}$$

In addition, there also appears renormalization of coefficients α_{11} and α_{12} given by Eqn. 2.16 and Eqn. 2.17, which was already discussed in Sec. 2.1.

Finally, there appears term that originates from increase of stored energy due to external stress. It only shifts the zero energy. It is not taken into account, since it does not influence the variations of the free energy functional which are responsible for the evolution of polarization in the model.

If homogeneous mechanical deformation free $\overline{e}$ is prescribed instead of homogeneous stress $\overline{\sigma}$, the procedure is similar. Total stress is computed with use of Hook's law. Internal stress is then obtained from Eqn. 2.40. Finally the external stress $\overline{\sigma}_{ij}^{\mathrm{ext}}$ is computed from Eqn. 2.39 which must be applied in order to fix the deformation of the sample. This stress is then virtually applied to the sample, thus reproducing the clamping of the sample.

2.5 Electrostatic long-range interaction

To describe electrostatic effects, it is necessary to include additional, strongly nonlocal term describing long-range interaction of individual dipoles with electric field of all other dipoles. Electrostatic local electric field from dipoles is possible to write in the form

$$\mathbf{E}_{\mathrm{dep}}(\mathbf{r}) = -\frac{1}{4\pi\epsilon_B\epsilon_0}\int \mathrm{d}\mathbf{s}\left[\frac{\mathbf{P}(\mathbf{s})}{|\mathbf{R}|^3} - \frac{3(\mathbf{P}(\mathbf{s})\cdot\mathbf{R})\mathbf{R}}{|\mathbf{R}|^5}\right] \tag{2.45}$$

with $\mathbf{R} = \mathbf{r} - \mathbf{s}$, and energy increase due to this field is

$$F_{\mathrm{dep}}\left[\{P_i\}\right] = \frac{1}{8\pi\epsilon_0\epsilon_{\mathrm{B}}}\iint \mathrm{d}\mathbf{r}\mathrm{d}\mathbf{s}\left[\frac{\mathbf{P}(\mathbf{r})\cdot\mathbf{P}(\mathbf{s})}{|\mathbf{R}|^3} - \frac{3(\mathbf{P}(\mathbf{r})\cdot\mathbf{R})(\mathbf{P}(\mathbf{s})\cdot\mathbf{R})}{|\mathbf{R}|^5}\right] . \tag{2.46}$$

Here ϵ_{B} stands for relative permittivity of background, coming from electron polarizability and from contributions of higher frequency polar phonon modes[7].

Polarization can be split into two parts, homogeneous and inhomogeneous:

$$\mathbf{P}(\mathbf{r}) = \overline{\mathbf{P}} + \delta\mathbf{P}(\mathbf{r}) \ . \tag{2.47}$$

For inhomogeneous part it holds

$$\int \mathrm{d}\mathbf{r}\ \delta\mathbf{P}(\mathbf{r}) = 0 \tag{2.48}$$

[7]The dynamics of polarization field is bound to the "soft mode": a polar mode with lower frequency (see Sec. 4).

Depolarization energy as compound of three terms then reads

$$F_{\mathrm{dep}}\left[\{P_i\}\right] = F_{\mathrm{dep}}^{\mathrm{het}}[\{\delta P_i\}] + F_{\mathrm{dep}}^{\mathrm{cross}}[\{\overline{P_i}, \delta P_i\}] + F_{\mathrm{dep}}^{\mathrm{hom}}[\{\overline{P_i}\}] \; . \tag{2.49}$$

First contribution, $F_{\mathrm{dep}}^{\mathrm{het}}[\{\delta P_i\}]$, comes from the spatially dependent, inhomogeneous part of polarization. In Fourier space, it has the form (see Sec. C.4)

$$F_{\mathrm{dep}}[\{\delta P_i\}] = \frac{1}{2\epsilon_B\epsilon_0}\frac{1}{(2\pi)^3}\int \mathrm{d}\mathbf{k}\frac{|\delta\mathbf{P}(\mathbf{k})\cdot\mathbf{k}|^2}{k^2} \; . \tag{2.50}$$

with $\mathbf{P}(\mathbf{k})$ is zero for $k = 0$.

The fact, that $\mathbf{P}(\mathbf{k})$ is zero, together with $\overline{\mathbf{P}}(\mathbf{k})$ nonzero (and not well defined) only in point $k = 0$ implies that the cross term $F_{\mathrm{dep}}^{\mathrm{cross}}[\{\overline{P_i}, \delta P_i\}]$ vanish.

Finally, the last part, the contribution of homogeneous part of polarization, reads (see Eqn. 2.4):

$$F_{\mathrm{dep}}^{\mathrm{hom}}[\{\overline{P_i}\}] = -\frac{1}{2}\int \mathrm{d}\mathbf{r}\; \mathbf{E}\cdot\overline{\mathbf{P}} = -\frac{1}{2}\int \mathrm{d}\mathbf{r}\left(-\frac{\overline{\mathbf{P}}}{2\epsilon_B\epsilon_0}\right)\cdot\overline{\mathbf{P}} = \frac{\left(\overline{\mathbf{P}}\cdot\overline{\mathbf{P}}\right)V}{2\epsilon_B\epsilon_0} \; , \tag{2.51}$$

where V is the volume of integration area. It is zero in the case of infinite sample, periodic sample or for sample with ideal compensation of surface charges[8].
Generally, the depolarization field can be evaluated from the equation

$$\mathrm{div}\;\mathbf{E}_{\mathrm{dep}}(\mathrm{r}) = -\frac{1}{\epsilon_B\epsilon_0}\mathrm{div}\;\mathbf{P}(\mathrm{r}) \, . \tag{2.52}$$

[8]For example by short-cut metallic electrodes.

Chapter 3

Charge-free elastically compatible domain walls

Systematic study of elastically compatible domain walls in all ferroelectric phases of $BaTiO_3$ within charge-free assumption div $\mathbf{P} = 0$ is given in the framework of phenomenological GGLD model. Profiles of domain walls are computed analytically for Ising-type[1] domain walls. We give quantitative estimation of thickness and planar energy density of different walls present in $BaTiO_3$ in the whole temperature range of ferroelectric phases.

Study of domain wall provides information about domain wall energy density, mobility, intrinsic pinning or may show limits for modeling particular wall within continuous theory.

GGLD model was previously used for analytical study of domain walls in $BaTiO_3$ and other perovskites materials in tetragonal and orthorombic phase [33, 39, 26, 34]. Ferroelastic S-wall was recently studied for ferroelastic transition $m\bar{3}m \rightarrow mmm$ [35].

In this section we consider single infinite domain wall in a perfect infinite mechanically free crystal, which separates two elastically compatible domain states. Components of polarization and elastic tensor can vary across the domain wall, but introducing several simplifications enables analytical computations.

Firstly, we restrict investigation to head-to-tail arrangement that is strongly preferred by electrostatic dipole-dipole interaction in non-conductive crystal. But even in head-to-tail arrangement there can be charges in domain wall arising from variation of polarization component perpendicular to the wall. In [26] it was shown, that the presence of a dipole-dipole interaction in ideally insulating crystal result in almost perfectly constant component of polarization perpendicular to the domain wall (here shown for T90 wall in Sec. 3.5). Therefore only ideally non-charged (div $\mathbf{P} = 0$) domain walls will be taken into account here.

Second assumption is that there is only one component of polarization that changes through the domain wall. One dimensional problem has analytical solution and allows for comparison of complete set of walls in $BaTiO_3$.

[1] Ising domain wall has just one component of polarization changing through domain wall. This component is in the plane of the wall

3.1 Domain walls

Complete list of permissible ferroelastic domain walls can be obtained from symmetry. Relevant considerations are to be found in Fousek [17], Fousek and Janovec [4] and Janovec [40]. Possible types of domain wall in each of ferroelectric species are discussed. Crystal is considered to be perfect, infinite, composed of two adjacent domains with deformation characterized by two different strain tensors. Domains are separated by a wall of zero thickness. Appearance of spontaneous polarization is always accompanied by occurrence of spontaneous deformation thanks to the electromechanical coupling.

An elastically permissible (or elastically compatible) domain wall with normal [hkl] separating two adjacent domains characterized by strain tensor ${}^1e_{ij}$, ${}^2e_{ij}$ obeys for any in-plane vector $d\mathbf{s}$ ($h\,ds_1 + k\,ds_2 + l\,ds_3 = 0$) relation (Ref. [4])

$$\sum_{k,l=1}^{3} \Delta_{kl} ds_k ds_l = 0 \ , \tag{3.1}$$

where $\Delta_{kl} = {}^1e_{kl} - {}^2e_{kl}$ is the difference between components of strain tensor in adjacent domains. Elastically permissible domain walls can be infinitely large. They separates domains which mechanically fits each other. There are no dislocations and in-plane tensions between adjacent domains.

From symmetry considerations it follows [17], that there are only three possibilities for the number N of domain wall separating two domains:

1. N=0: No mechanically compatible wall exists.

2. N=2: Two mutually perpendicular domain walls exist. Each of them is either W_f-type wall or S-type wall. W_f wall have its orientation fixed with respect to symmetry elements of parent phase while orientation of S-wall is determined only by the value of strain tensor components of incident domains and it can therefore vary with temperature. In the case of polar dielectric one wall of the pair is head-to-tail, the second is head-to-head, as indicated in Fig. 3.1.

3. N=∞: Arbitrary oriented wall is possible (W_∞ wall). Particular orientation of W_∞ domain wall, which were determined from point compatibility considerations might be preffered by anisotropy in domain wall energies.

In a real crystal a wall can be disoriented with respect to obtained directions, if the increase of elastic energy is small.

$BaTiO_3$ with its four ferroelectric phases offers wide variety of elastically permissible domain walls [17]:

In the tetragonal phase there exist 180 degree W_∞ domain wall (T180) and 90 degree (T90) W_f domain walls. Each of them can be either charged or not charged. 90 degree charged and charge-free walls create pairs as discussed for the case $N = 2$.

In the orthogonal phase the situation is more complicated. There is again W_∞ 180 degree domain wall (O180) and 90 degree W_f domain wall (O90) with the same properties as in tetragonal phase. In the case of 60 degree angle between adjacent polarization direction, there exist pairs of mutually perpendicular walls created by one head-to-tail W_f wall and one head-to-head S-type wall. In the case of 120 degree angle the situation is the same but S walls are

Table 3.1: List of conjugate W_f-type and S-type domain walls in orthorombic phase. Chosen direction of spontaneous polarization is [110] ("0" in Fig. 1.6). Subscript c denotes charged domain wall. The constant B stands for $\frac{2e_t}{e_a-e_c}$. Domain walls that are plotted in Fig. 3.1 are indicated by boldfaced angle.

Conjugate vector	W_f-wall	S-wall	Angle
[011]	$[10\bar{1}]_c$	[1B1]	60
[101]	$[0\bar{1}1]_c$	[B11]	60
$[01\bar{1}]$	$[101]_c$	$[1B\bar{1}]$	**60**
$[10\bar{1}]$	$[011]_c$	$[B1\bar{1}]$	60
$[0\bar{1}1]$	[101]	$[1B\bar{1}]_c$	**120**
$[\bar{1}01]$	[011]	$[B1\bar{1}]_c$	120
[011]	$[10\bar{1}]$	$[1B1]_c$	120
[101]	$[01\bar{1}]$	$[B11]_c$	120

charged. As only non-charged walls are discussed here, S-type domain wall will be referred to as O60 and its conjugate W_f wall as O120. Complete list of 60 and 120 degree domain walls for all combination of spontaneous states is given in Tab. 3.1.

In the rhombohedral phase, there exist W_∞ 180 degree domain wall (R180) and pairs of charged and non-charged W_f-type domain walls with mutual angle of polarization being either 109 or 71 degree (R109 and R71 walls).

These domain walls are also schematically depicted in Fig. 3.1.

If necessary, nonequivalent domain walls are further distinguished by their normal (e.g. T180{001}, T180{011}). Possible elastically permissible electrically neutral W_f-type and S-type domain walls and important orientations of 180 degree domain walls are plotted in Fig. 3.1. For completeness, charged W_f-type and S-type domain walls are plotted in Fig. 3.2.

3.2 One-dimensional approximation

Two elastically compatible spontaneous states are chosen and the orientation of the wall is determined. Spontaneous polarization corresponds to boundary values of polarization in infinite distance from the wall. Spontaneous strain in the infinity is computed from Eqn. 2.13. External stress is zero.

New coordinate system is chosen with base vectors $\mathbf{r}, \mathbf{s}, \mathbf{t}$ so that P_r component of polarization vector $\mathbf{P}$ changes its sign through the wall, $\mathbf{s}$ is the normal to the wall and $\mathbf{t}$ component complements orthonormal coordinate system. New coordinate system will be denoted by primes and transformed energy functionals, tensors and vectors will be referred to as primed quantities or denoted by corresponding (r,s,t) indices. Complete set of transformation matrices for elastically permissible domain walls in $BaTiO_3$ is given in Sec. E.3.

All quantities in this approximation vary only along normal to the wall $\mathbf{s}$. Polarization vector and strain tensor are assumed in to have the form $\mathbf{P'} = [P_\mathrm{r}(s), P_\mathrm{s}(\pm\infty), P_\mathrm{t}(\pm\infty)]$ and $e' = [e_{rr}(\pm\infty), e_{ss}(s), e_{tt}(\pm\infty), 2e_{st}(s), 2e_{rt}(\pm\infty), 2e_{rs}(s)]^T$, respectively. The form of the polarization corresponds to the previously mentioned simplifications (div $\mathbf{P} = 0$ implies constant

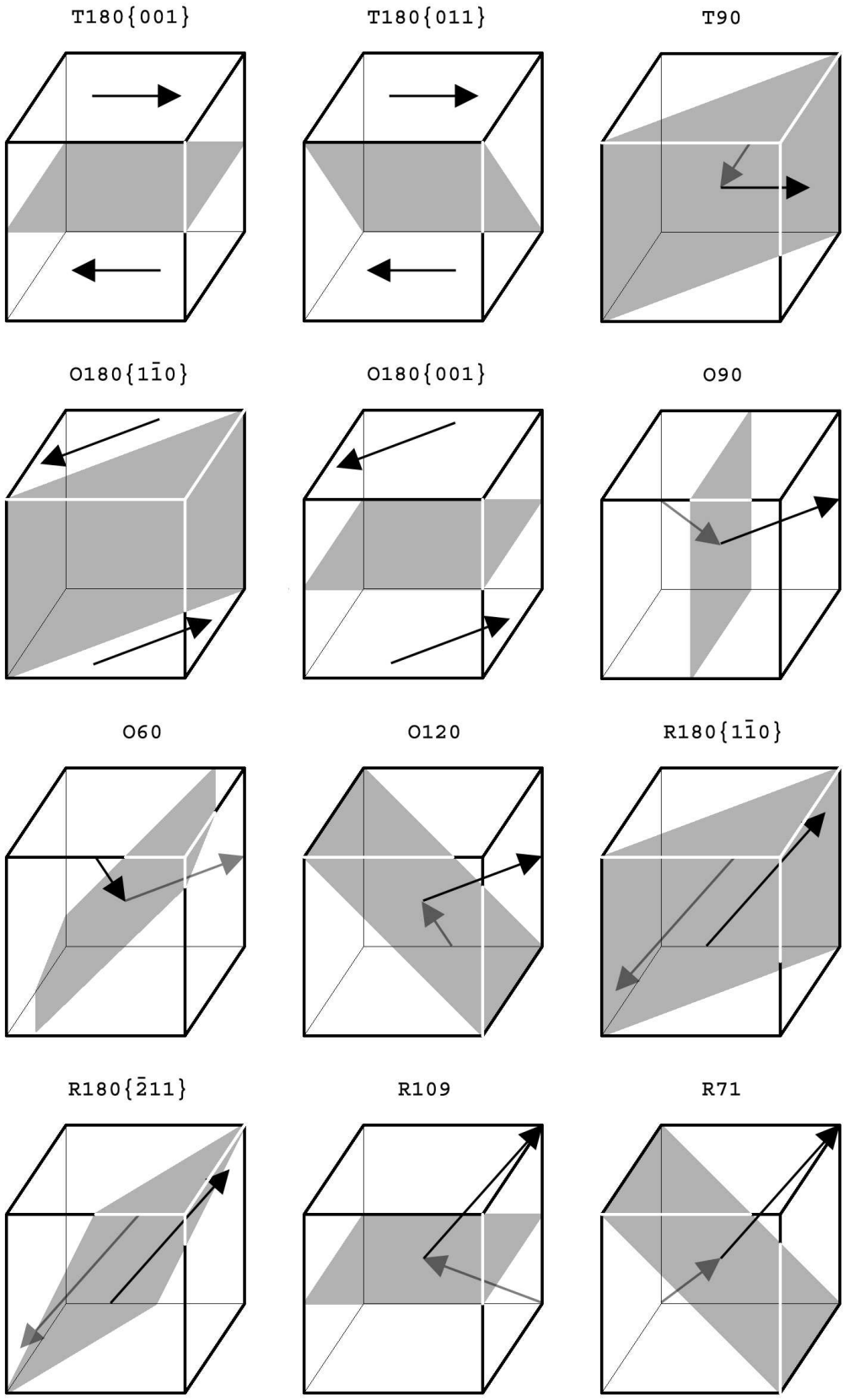

Figure 3.1: Possible non-charged domain walls in $BaTiO_3$ ferroelectric phases. Arrows corresponds to spontaneous polarization values. If it is possible (if domain wall is not 180 degree), the head of the first arrow touch the tail of the second arrow, thus indicating the head-to-tail character of the wall.

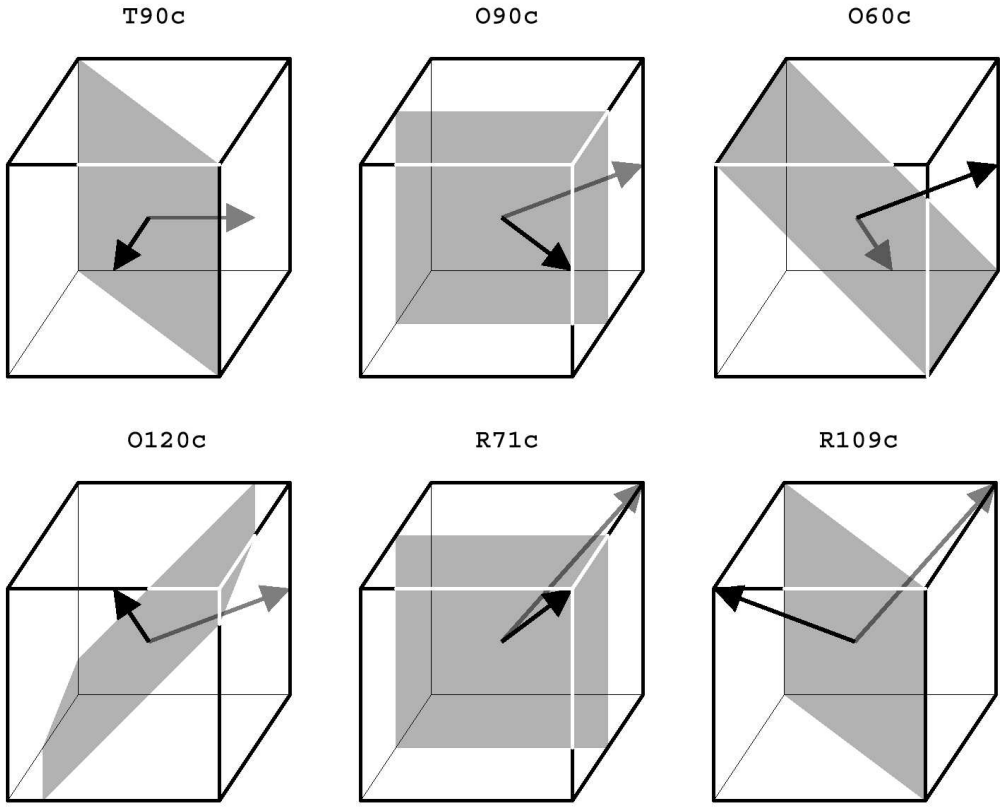

Figure 3.2: Charged W_f-type and S-type domain walls in $BaTiO_3$ ferroelectric phases.

normal component of polarization to the domain wall and only Ising walls with single changing component are taken into account). The form of the strain tensor follows directly from mechanical compatibility and boundary conditions.

Remaining s-dependent components of strain tensor are then computed from Euler-Lagrange mechanical equilibrium condition

$$\sum_{j=1}^{3} \frac{\partial \sigma'_{ij}}{\partial x'_j} = \sum_{j=1}^{3} \frac{\partial}{\partial x'_j} \left(\frac{\partial f'_{\mathrm{Cq}}}{\partial e'_{ij}} \right) = 0 \ , \tag{3.2}$$

where $f' = f' \left[P_{\mathrm{r}}, P_{\mathrm{r},s}, e_{ss}, e_{st}, e_{rs} \right] = f^{(\mathrm{e})\prime} \left[P_{\mathrm{r}} \right] + f'_{\mathrm{G}} \left[P_{\mathrm{r},s} \right] + f'_{\mathrm{Cq}} \left[P_{\mathrm{r}}, e_{ss}, e_{st}, e_{rs} \right]$ is transformed free energy. From boundary conditions for stress and the fact, that only variation is along s direction we get

$$\frac{\partial f'_{\mathrm{Cq}}}{\partial e'_{ij}} + C_{ij} = 0 \tag{3.3}$$

for $ij \in \{ss, rs, st\}$ with the integration constant C_{ij} to be determined from boundary conditions. Boundary conditions for all elastically permissible domain walls in $BaTiO_3$ are given in Tab. 3.2. We finally get dependence of transformed strain tensor component on polarization

$$\begin{aligned} e_{ss} &= e_{ss}(P_r(s)) \\ e_{rs} &= e_{rs}(P_r(s)) \\ e_{st} &= e_{st}(P_r(s)) \ . \end{aligned} \tag{3.4}$$

Euler-Lagrange equation for polarization

$$\sum_{j=1}^{3} \frac{\partial}{\partial x'_j} \frac{\partial f'}{\partial P'_{i,j}} - \frac{\partial f'}{\partial P'_i} = 0 \tag{3.5}$$

reduces to

$$\frac{\partial}{\partial s} \frac{\partial f'}{\partial P_{\mathrm{r},s}} - \frac{\partial f'}{\partial P_{\mathrm{r}}} = 0 \ . \tag{3.6}$$

Obtained strain components Eqn. 3.4 are substituted into Eqn. 3.6. It is possible now to rewrite the Euler-Lagrange equation for polarization in the form

$$g \frac{d^2 p(s)}{ds^2} = 2a_1 p(s) + 4a_{11} p^3(s) + 6a_{111} p^5(s) \ , \tag{3.7}$$

where $p(s)$ stands for $P_{\mathrm{r}}(s)$. Euler-Lagrange potential f_{EL} is obtained by integration[2]:

$$\frac{g}{2} \left(\frac{\partial p}{\partial s} \right)^2 = f_{\mathrm{EL}}(p) \tag{3.8}$$

with

$$f_{EL}(p) = a_1 p^2(s) + a_{11} p^4(s) + a_{111} p^6(s) \ . \tag{3.9}$$

Coefficients a_1, a_{11} and a_{111} include elastic and electrostriction interaction. Euler-Lagrange potential is a double-well potential with two minima given by

$$p_\infty^2 = \frac{-a_{11} + \sqrt{a_{11}^2 - 3a_{111}a_1}}{3a_{111}} \tag{3.10}$$

such that $p_\infty = |P_{\mathrm{r}}(\infty)| = |P_{\mathrm{r}}(-\infty)|$. Following procedure is based on [27]. The differential equation (3.7) has analytical solution

$$p(s) = p_\infty \frac{\sinh(s/\xi')}{\sqrt{A + sinh^2(s/\xi')}} \ , \tag{3.11}$$

where

$$\xi' = \frac{\xi}{\sqrt{A}} \tag{3.12}$$

is determined using the depart from simple *tanh* profile

$$A = \frac{3a_{111}P_\infty^2 + a_{11}}{2a_{111}P_\infty^2 + a_{11}} \ . \tag{3.13}$$

Domain wall thickness is defined (Fig. 3.3) as

$$2\xi = p_\infty \sqrt{\frac{2g}{U}} \tag{3.14}$$

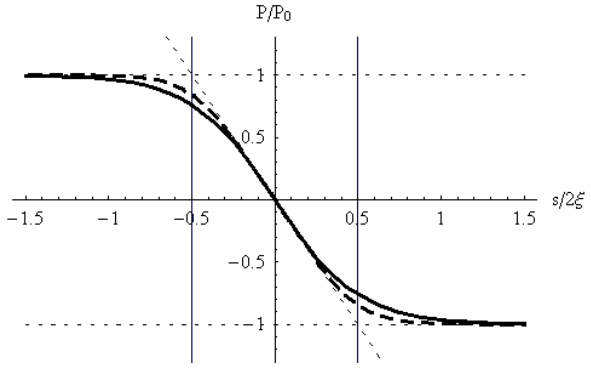

Figure 3.3: Analytical profile of domain wall (Eqn. 3.11). Two domain walls are indicated, continuous line for shape factor $A = 1$, broken line for $A = 3$. Both profiles have the same derivative for $s/2\xi = 0$ and therefore also the same thickness (Eqn. 3.14) that is indicated by vertical lines.

with U being the corresponding energy barrier in Euler-Lagrange potential $f_{EL}(0) - f_{EL}(p_\infty)$

$$U = 2a_{111}p_\infty^6 + a_{11}p_\infty^4 \tag{3.15}$$

The surface energy density of such domain wall is

$$\Sigma = \frac{4}{3}p_\infty\sqrt{2gU}\left[A^{5/2}I(A)\right] \ , \tag{3.16}$$

where

$$I(A) = \frac{3}{4}\int_{-\infty}^{\infty}\frac{cosh^2(t)dt}{(A + cosh^2(t) - 1)^3} \ . \tag{3.17}$$

It has a property $I(1) = 1$. Contribution from the shape correction factor $A^{5/2}I(A)$ is plotted in Fig. 3.4.

[2]It is also possible to obtain coefficients a_1, a_{11} and a_{111} by simple substitution of strain tensor components from Eqn. 3.3 into transformed free energy f'.

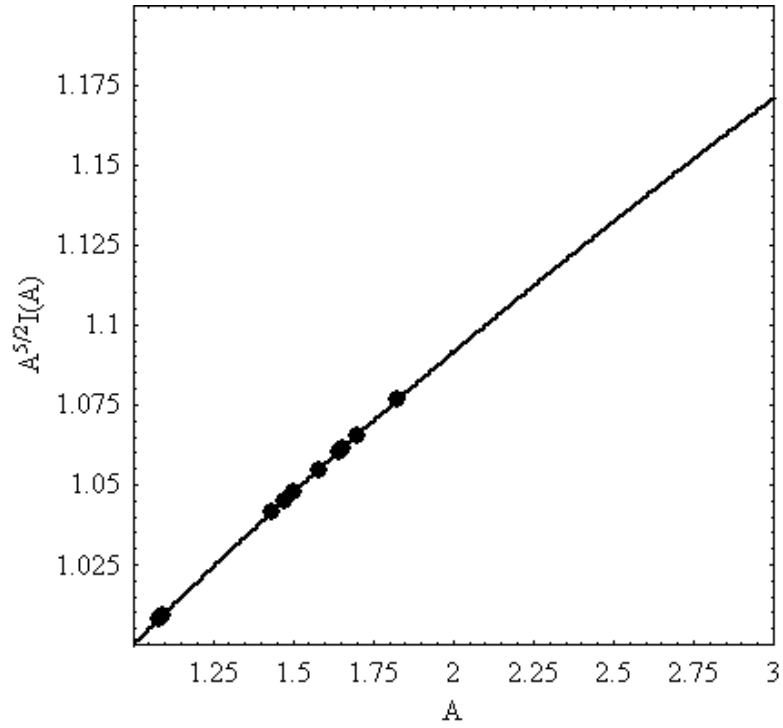

Figure 3.4: Almost linear dependence of correction factor in the expression for domain wall energy density as a function of the shape coefficient A (Eqn. 3.13).

Table 3.2: Base vectors of the new (primed) coordinate system and boundary conditions of inspected domain walls used in computations. Vectors $\mathbf{s}_{O60}$ and $\mathbf{t}_{O60}$ are defined in Eqn. 3.26.

Wall	$\mathbf{r}$	$\mathbf{s}$	$\mathbf{t}$	$\frac{\mathbf{P}(-\infty)}{P_0}$	$\frac{\mathbf{P}(\infty)}{P_0}$	$\mathbf{e}(-\infty)$	$\mathbf{e}(\infty)$
T180{001}	$(1,0,0)$	$(0,0,1)$	$(0,-1,0)$	$(1,0,0)$	$(-1,0,0)$	$(e_\parallel, e_\perp, e_\perp, 0, 0, 0)$	$(e_\parallel, e_\perp, e_\perp, 0, 0, 0)$
T180{011}	$(1,0,0)$	$(0, \frac{1}{\sqrt{2}}, \frac{1}{\sqrt{2}})$	$(0, \frac{-1}{\sqrt{2}}, \frac{1}{\sqrt{2}})$	$(1,0,0)$	$(-1,0,0)$	$(e_\parallel, e_\perp, e_\perp, 0, 0, 0)$	$(e_\parallel, e_\perp, e_\perp, 0, 0, 0)$
T90	$(\frac{1}{\sqrt{2}}, \frac{1}{\sqrt{2}}, 0)$	$(\frac{1}{\sqrt{2}}, \frac{-1}{\sqrt{2}}, 0)$	$(0,0,-1)$	$(1,0,0)$	$(0,-1,0)$	$(e_\perp, e_\perp, e_\parallel, 0, 0, 0)$	$(e_\perp, e_\parallel, e_\perp, 0, 0, 0)$
O180{1$\bar{1}$0}	$(\frac{1}{\sqrt{2}}, \frac{1}{\sqrt{2}}, 0)$	$(\frac{1}{\sqrt{2}}, \frac{-1}{\sqrt{2}}, 0)$	$(0,0,-1)$	$(\frac{1}{\sqrt{2}}, \frac{1}{\sqrt{2}}, 0)$	$(\frac{-1}{\sqrt{2}}, \frac{-1}{\sqrt{2}}, 0)$	$(e_a, e_a, e_c, 0, 0, 2e_b)$	$(e_a, e_a, e_c, 0, 0, 2e_b)$
O180{001}	$(\frac{1}{\sqrt{2}}, \frac{1}{\sqrt{2}}, 0)$	$(0,0,1)$	$(\frac{1}{\sqrt{2}}, \frac{-1}{\sqrt{2}}, 0)$	$(\frac{1}{\sqrt{2}}, \frac{1}{\sqrt{2}}, 0)$	$(\frac{-1}{\sqrt{2}}, \frac{-1}{\sqrt{2}}, 0)$	$(e_a, e_a, e_c, 0, 0, 2e_b)$	$(e_a, e_a, e_c, 0, 0, 2e_b)$
O90	$(0,1,0)$	$(1,0,0)$	$(0,0,-1)$	$(\frac{1}{\sqrt{2}}, \frac{1}{\sqrt{2}}, 0)$	$(\frac{1}{\sqrt{2}}, \frac{-1}{\sqrt{2}}, 0)$	$(e_a, e_a, e_c, 0, 0, 2e_b)$	$(e_a, e_a, e_c, 0, 0, -2e_b)$
O60	$(\frac{1}{\sqrt{2}}, 0, \frac{1}{\sqrt{2}})$	$\mathbf{s}_{O60}$	$\mathbf{t}_{O60}$	$(\frac{1}{\sqrt{2}}, \frac{1}{\sqrt{2}}, 0)$	$(0, \frac{1}{\sqrt{2}}, \frac{-1}{\sqrt{2}})$	$(e_a, e_a, e_c, 0, 0, 2e_b)$	$(e_c, e_a, e_a, -2e_b, 0, 0)$
O120	$(\frac{1}{\sqrt{6}}, \frac{2}{\sqrt{6}}, \frac{-1}{\sqrt{6}})$	$(\frac{1}{\sqrt{2}}, 0, \frac{1}{\sqrt{2}})$	$(\frac{1}{\sqrt{3}}, \frac{-1}{\sqrt{3}}, \frac{-1}{\sqrt{3}})$	$(\frac{1}{\sqrt{2}}, \frac{1}{\sqrt{2}}, 0)$	$(0, \frac{-1}{\sqrt{2}}, \frac{1}{\sqrt{2}})$	$(e_a, e_a, e_c, 0, 0, 2e_b)$	$(e_c, e_a, e_a, -2e_b, 0, 0)$
R180{1$\bar{1}$0}	$(\frac{1}{\sqrt{3}}, \frac{1}{\sqrt{3}}, \frac{1}{\sqrt{3}})$	$(\frac{1}{\sqrt{2}}, \frac{-1}{\sqrt{2}}, 0)$	$(\frac{1}{\sqrt{6}}, \frac{1}{\sqrt{6}}, \frac{-2}{\sqrt{6}})$	$(\frac{1}{\sqrt{3}}, \frac{1}{\sqrt{3}}, \frac{1}{\sqrt{3}})$	$(\frac{-1}{\sqrt{3}}, \frac{-1}{\sqrt{3}}, \frac{-1}{\sqrt{3}})$	$(e_a, e_a, e_a, 2e_b, 2e_b, 2e_b)$	$(e_a, e_a, e_a, 2e_b, 2e_b, 2e_b)$
R180{$\bar{2}$11}	$(\frac{1}{\sqrt{3}}, \frac{1}{\sqrt{3}}, \frac{1}{\sqrt{3}})$	$(\frac{-2}{\sqrt{6}}, \frac{1}{\sqrt{6}}, \frac{1}{\sqrt{6}})$	$(0, \frac{-1}{\sqrt{2}}, \frac{1}{\sqrt{2}})$	$(\frac{1}{\sqrt{3}}, \frac{1}{\sqrt{3}}, \frac{1}{\sqrt{3}})$	$(\frac{-1}{\sqrt{3}}, \frac{-1}{\sqrt{3}}, \frac{-1}{\sqrt{3}})$	$(e_a, e_a, e_a, 2e_b, 2e_b, 2e_b)$	$(e_a, e_a, e_a, 2e_b, 2e_b, 2e_b)$
R109	$(\frac{1}{\sqrt{2}}, \frac{1}{\sqrt{2}}, 0)$	$(0,0,1)$	$(\frac{1}{\sqrt{2}}, \frac{-1}{\sqrt{2}}, 0)$	$(\frac{1}{\sqrt{3}}, \frac{1}{\sqrt{3}}, \frac{1}{\sqrt{3}})$	$(\frac{-1}{\sqrt{3}}, \frac{-1}{\sqrt{3}}, \frac{1}{\sqrt{3}})$	$(e_a, e_a, e_a, 2e_b, 2e_b, 2e_b)$	$(e_a, e_a, e_a, -2e_b, -2e_b, 2e_b)$
R71	$(0,1,0)$	$(\frac{1}{\sqrt{2}}, 0, \frac{1}{\sqrt{2}})$	$(\frac{1}{\sqrt{2}}, 0, \frac{-1}{\sqrt{2}})$	$(\frac{1}{\sqrt{3}}, \frac{1}{\sqrt{3}}, \frac{1}{\sqrt{3}})$	$(\frac{1}{\sqrt{3}}, \frac{-1}{\sqrt{3}}, \frac{1}{\sqrt{3}})$	$(e_a, e_a, e_a, 2e_b, 2e_b, 2e_b)$	$(e_a, e_a, e_a, -2e_b, 2e_b, -2e_b)$

3.3 Results

We applied previously described model to all non-charged elastically compatible domain wall in $BaTiO_3$. Numerical values were taken from Tab. 2.1 set "A". Boundary conditions are provided in Tab. 3.2. Used parameters $\{a_1,\ a_{11},\ a_{111},\ g\}$ and resulting wall characteristics are given in Tab. 3.3. Finally, plots of domain wall thicknesses and energies (for all considered walls, in the whole temperature) range are given in Fig. 3.9.

Profiles of polarization are plotted in original coordinate system. Profiles of strain tensor components through a domain wall was obtained by substitution of $P_r(s) = p(s)$ into Eqn. 3.4 and back transformation into original coordinate system.

3.3.1 T180{001} domain wall

Parameters computed from Tab. 2.1 for tetragonal phase (298 K) have numerical values $P_0 = 0.265$, $e_\parallel = Q_{11}P_0^2 = 7.77 \times 10^{-3}$ and $e_\perp = Q_{12}P_0^2 = -3.18 \times 10^{-3}$.

Procedure described above lead to the equation (3.7) with coefficients

$$\begin{aligned} p_\infty &= P_0 \\ g &= G_{44} \\ a_1 &= \alpha_1 - e_\parallel q_{11} - 2e_\perp q_{12} + \frac{q_{12}^2 P_0^2}{C_{11}} \\ a_{11} &= \alpha_{11}^{(e)} - \frac{1}{2}\frac{q_{12}^2}{C_{11}} \\ a_{111} &= \alpha_{111}\ . \end{aligned} \tag{3.18}$$

From discussion in Sec. 3.4 it follows that these expressions holds for both T180{001} and T180{011} domain wall.

3.3.2 T180{011} domain wall

Coefficients of the equation (3.7) are

$$\begin{aligned} p_\infty &= P_0 \\ g &= G_{44} \\ a_1 &= \alpha_1 - e_\parallel q_{11} + \frac{2C_{12}e_\parallel - 4C_{44}e_\perp}{C'_{11}} \\ a_{11} &= \alpha_{11}^{(e)} - \frac{1}{2}\frac{q_{12}^2}{C'_{11}} \\ a_{111} &= \alpha_{111}\ , \end{aligned} \tag{3.19}$$

where C'_{11} is defined in (3.22). Values of coefficients a_1, a_{11} for T180{001} and T180{011} are numerically very close, a_1, and g are equal. Both domain walls have similar profile in primed coordinates.

3.3.3 T90 domain wall

Coefficients of the equation (3.7) are

$$\begin{aligned} p_\infty &= \frac{P_0}{\sqrt{2}} \\ g &= \frac{(G_{11}-G_{12})}{2} \\ a_1 &= \alpha_1^r + \alpha_{12}^{sr}\frac{P_0^2}{2} + \alpha'_{112}\frac{P_0^4}{4} \\ a_{11} &= \alpha_{11}^r + \alpha'_{112}\frac{P_0^2}{2} \\ a_{111} &= \alpha'_{111} \end{aligned} \tag{3.20}$$

with

$$\begin{aligned} a_1^r &= \alpha_1 - \left[\frac{1}{3}\frac{\hat{q}_{11}^2}{\hat{C}_{11}} + \frac{1}{6}\frac{\hat{q}_{22}^2}{\hat{C}_{22}} - \frac{(q_{11}+q_{12})q'_{12}}{2C'_{11}}\right]P_0^2 \\ a_{11}^r &= \frac{\alpha_{11}^{(e)}}{2} + \frac{\alpha_{12}^{(e)}}{4} - \frac{q'^2_{12}}{2C'_{11}} \\ a_{12}^{rs} &= 3\alpha_{11}^{(e)} - \frac{\alpha_{12}^{(e)}}{2} - \frac{q'_{11}q'_{12}}{C'_{11}} - \frac{\hat{q}_{22}^2}{2\hat{C}_{22}} \\ a'_{111} &= \frac{1}{4}(\alpha_{111}+\alpha_{112}) \\ a'_{112} &= \frac{1}{4}(15\alpha_{111}-\alpha_{112}) \end{aligned} \tag{3.21}$$

derived in [26]. Primes denotes transformed components of elastic and electrostriction tensor.

$$\begin{aligned} C'_{11} &= \frac{C_{11}+C_{12}+2C_{44}}{2} \\ C'_{12} &= \frac{C_{11}+C_{12}-2C_{44}}{2} \\ C'_{66} &= \frac{C_{11}-C_{12}}{2} \\ q'_{11} &= \frac{q_{11}+q_{12}+q_{44}}{2} \\ q'_{12} &= \frac{q_{11}+q_{12}-q_{44}}{2} \\ q'_{66} &= q_{11}-q_{12}\ . \end{aligned} \tag{3.22}$$

T90 wall is approximately 5 times thicker than T180 wall mainly due to anisotropy of gradient terms and low energy barrier. Their energies are comparable.

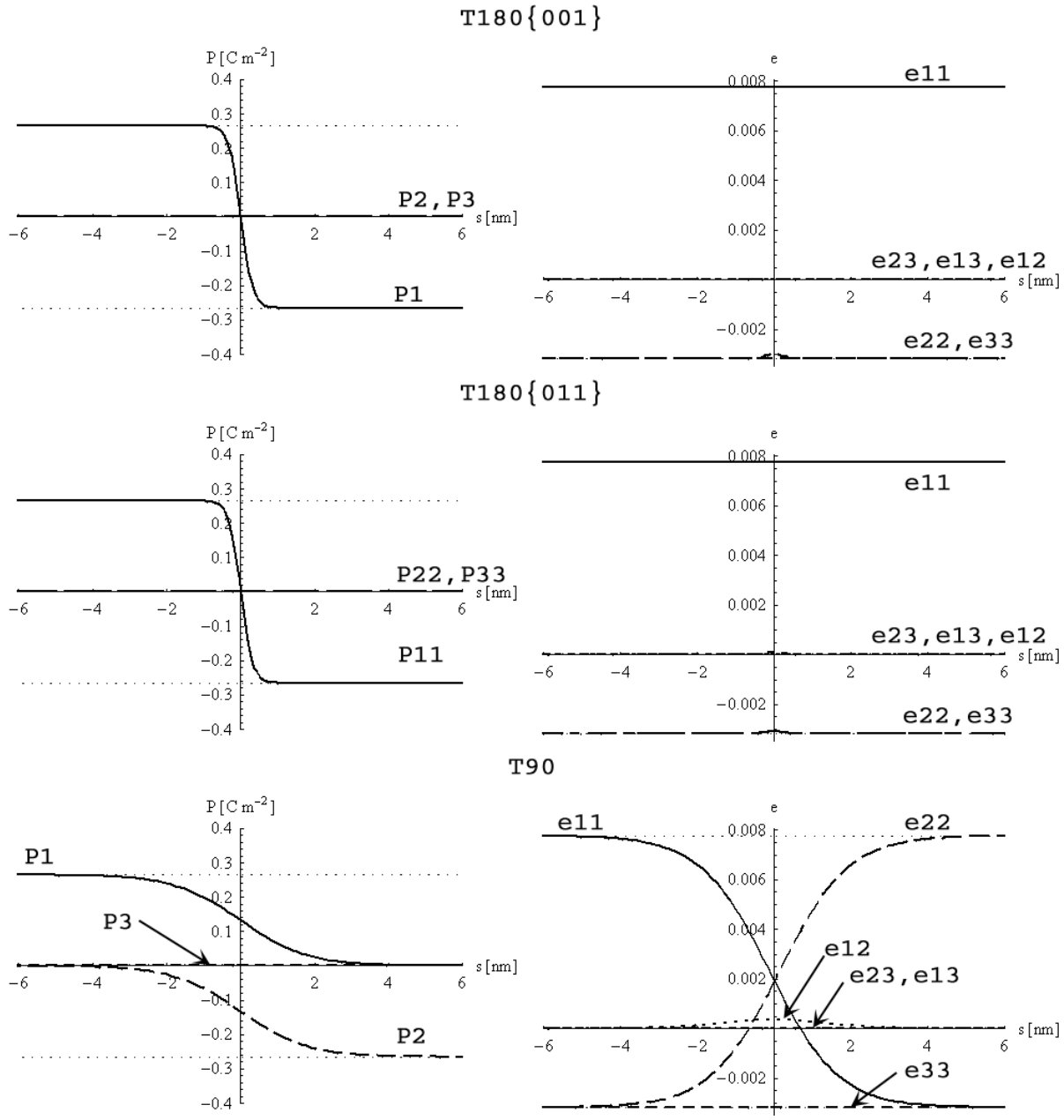

Figure 3.5: Analytical profiles of polarization and strain components inside the T180{001}, T180{011} and T90 wall.

3.3.4 O180{1$\bar{1}$0} domain wall

Numerical values of spontaneous polarization and strain for orthorombic phase (208 K) is $P_0 = 0.331$, $e_a = \frac{Q_{11}+Q_{12}}{2} P_0^2 = 3.58 \times 10^{-3}$, $e_c = Q_{12} P_0^2 = -4.96 \times 10^{-3}$ and $e_b = \frac{Q_{44}}{4} P_0^2 = 0.79 \times 10^{-3}$.

Resulting coefficients are

$$\begin{aligned} p_\infty &= P_0 \\ g &= \frac{G_{11} - G_{12}}{2} \\ a_1 &= \alpha_1 - e_b(q'_{11} - q'_{12}) - e_c q_{12} - e_a(q'_{11} + q'_{12}) + \frac{q'^2_{12}}{C'_{11}} P_0^2 \\ a_{11} &= \frac{\alpha^{(e)}_{11}}{2} + \frac{\alpha^{(e)}_{12}}{4} - \frac{q'^2_{12}}{2C'_{11}} \\ a_{111} &= \frac{1}{4}(\alpha_{111} + \alpha_{112}) \end{aligned} \tag{3.23}$$

with the same primed components of tensors as in Eqn. 3.22.

3.3.5 O180{001} domain wall

Coefficients are

$$\begin{aligned} p_\infty &= P_0 \\ g &= G_{44} \\ a_1 &= \alpha_1 - e_a(q_{11} + q_{12}) - e_b q_{44} + 2e_a q_{12} \frac{C_{12}}{C_{11}} \\ a_{11} &= \frac{\alpha^{(e)}_{11}}{2} + \frac{\alpha^{(e)}_{12}}{4} - \frac{q^2_{12}}{2C_{11}} \\ a_{111} &= \frac{1}{4}(\alpha_{111} + \alpha_{112}) \ . \end{aligned} \tag{3.24}$$

Primed components of tensors are again the same as in Eqn. 3.22.

This domain wall is potentially not stable with respect to deviation of t-component of polarization. Ising assumption may not be correct. Domain wall of Bloch type may appear, instead (see Sec. 3.6 and appropriate graph of numerical solution in Fig. 3.14).

3.3.6 O90 domain wall

It leads to coefficients

$$\begin{aligned} p_\infty &= \frac{P_0}{\sqrt{2}} \\ g &= G_{44} \\ a_1 &= \alpha_1 + \alpha^{(e)}_{12} \frac{P_0^2}{2} + \alpha_{112} \frac{P_0^4}{4} + \left(\frac{q^2_{12}}{2C_{11}} - \frac{q^2_{44}}{4C_{44}} \right) P_0^2 \\ &\quad -e_a(q_{11} + q_{12}) - e_c q_{12} \end{aligned}$$

$$\begin{aligned} a_{11} &= \alpha_{11}^{(e)} + \frac{1}{2}\left(\alpha_{112}P_0^2 - \frac{q_{12}^2}{C_{11}}\right) \\ a_{111} &= \alpha_{111} \end{aligned} \tag{3.25}$$

3.3.7 O60 domain wall

S-type domain walls were reported in Ref. [4, 17]. Its orientation does not generally coincide with any crystallographic direction. Orientation of S-type wall is only dependent on strain tensor components and therefore will depend on temperature through temperature dependence of spontaneous polarization and eventually elastic and electrostriction coefficients.

$$\begin{aligned} \mathbf{r}_{O60} &= \left(\frac{1}{\sqrt{2}}, 0, \frac{1}{\sqrt{2}}\right) \\ \mathbf{s}_{O60} &= \left(\frac{e_a - e_c}{\sqrt{2(e_a-e_c)^2 + 4e_b^2}}, \frac{2e_b}{\sqrt{2(e_a-e_c)^2 + 4e_b^2}}, \frac{e_c - e_a}{\sqrt{2(e_a-e_c)^2 + 4e_b^2}}\right) \\ \mathbf{t}_{O60} &= \left(\frac{-e_b}{\sqrt{(e_a-e_c)^2 + 2e_b^2}}, \frac{e_a - e_c}{\sqrt{(e_a-e_c)^2 + 2e_b^2}}, \frac{e_b}{\sqrt{(e_a-e_c)^2 + 2e_b^2}}\right) . \end{aligned} \tag{3.26}$$

Numerical values of the vectors for temperature 208 K are

$$\begin{aligned} \mathbf{r}_{O60} &= (0.707, 0, 0.707) \\ \mathbf{s}_{O60} &= (0.701, 0.130, -0.701) \\ \mathbf{t}_{O60} &= (-0.092, 0.991, 0.092) \ . \end{aligned} \tag{3.27}$$

Due to complicated transformation the whole computation was performed numerically and therefore analytical expression for coefficients of Euler-Lagrange potential are not provided. Profiles of components polarization and strain for this wall are plotted in Fig. 3.6.

3.3.8 O120 domain wall

Parameters of the one-dimensional Euler-Lagrange equation are $p_\infty = \frac{\sqrt{3}}{2}P_0$, $g = \frac{G_{11}-G_{12}+4G_{44}}{6}$. Expressions for individual parameters of one-dimensional model are too complex to be given explicitly, numerical values of parameters of Eqn.3.7 are given in Tab. 3.3.

This domain wall is potentially not stable with respect to deviation of t-component of polarization. Ising assumption may not be correct. Domain wall of Bloch type may appear, instead (see Sec. 3.6 and appropriate graph of numerical solution in Fig. 3.14).

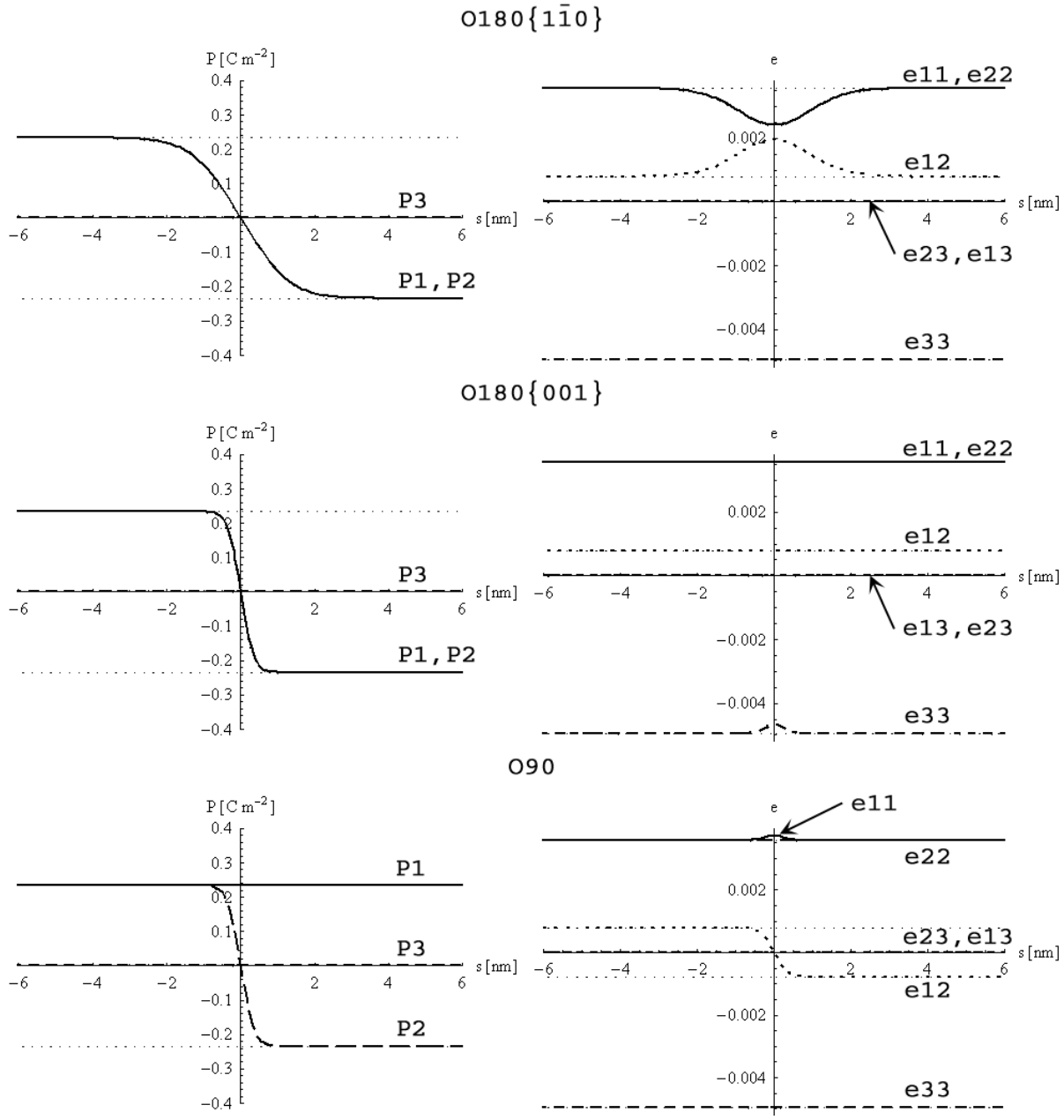

Figure 3.6: Analytical profiles of polarization and strain components inside the O180{1$\bar{1}$0} O180{001} and O90 walls.

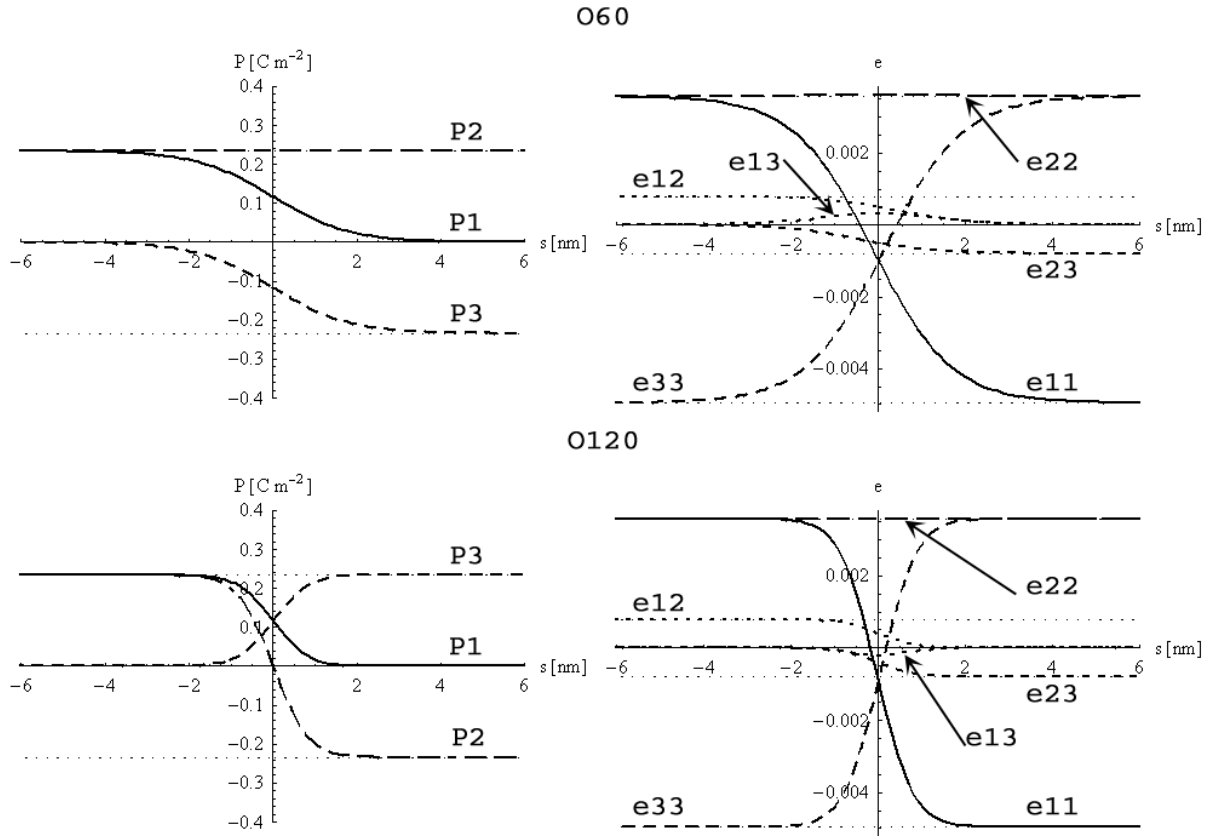

Figure 3.7: Analytical profiles of polarization and strain components inside the O60 and O120 walls.

3.3.9 R180{1$\bar{1}$0} domain wall

Numerical values of spontaneous polarization and spontaneous strain components for rhombohedral phase (118 K) are: $P_0 = 0.381$, $e_a = \frac{Q_{11}+2Q_{12}}{3} P_0^2 = 0.97 \times 10^{-3}$ and $e_b = \frac{Q_{44}}{4} P_0^2 = 0.70 \times 10^{-3}$.

Coefficients of the one-dimensional model are

$$\begin{aligned} p_\infty &= P_0 \\ g &= \frac{G_{11} - G_{12} + G_{44}}{3} \\ a_1 &= \alpha_1 + \frac{1}{6C'_{33}}[C_{12}(e_a(q_{11} + 2q_{12} - 4q_{44}) - 6e_b q_{44}) \\ &\quad -C_{11}(6e_b q_{44} + 3e_a q'_{11}) \\ &\quad -2C_{44}(3e_a(q_{11} + 2q_{12}) + 6e_b q'_{11})] \\ a_{11} &= \frac{\alpha_{11}^{(e)} + \alpha_{12}^{(e)}}{3} - \frac{q'^2_{13}}{2C'_{33}} \\ a_{111} &= \frac{3\alpha_{111} + 6\alpha_{112} + \alpha_{123}}{27} \end{aligned} \tag{3.28}$$

where

$$\begin{aligned} C'_{33} &= \frac{C_{11} + C_{12} + 2C_{44}}{2} \\ q'_{11} &= \frac{q_{11} + 2q_{12} + 2q_{44}}{3} \\ q'_{13} &= \frac{q_{11} + 2q_{12} - q_{44}}{3} \end{aligned} \tag{3.29}$$

This domain wall is potentially not stable with respect to deviation of t-component of polarization. Ising assumption may not be correct. Domain wall of Bloch type may appear, instead (see Sec. 3.6 and appropriate graph of numerical solution in Fig. 3.14).

3.3.10 R180{$\bar{2}$11} domain wall

The analytical expressions for a_1, a_{11}, a_{111} and g are not given for this wall. They are too complicated due to complex transformation of coordinates.

This domain wall is potentially not stable with respect to deviation of t-component of polarization. Ising assumption may not be correct. Domain wall of Bloch type may appear, instead (see Sec. 3.6 and appropriate graph of numerical solution in Fig. 3.14).

The additional minimum (on the contrary to other Ising walls that are unstable) is not rhombohedral. It is orthorombic minimum of Euler-Lagrange potential. For lower temperature this minimum does not exist and the domain wall isstable with respect to a change of t-component (The Ising assumption is correct).

3.3.11 R109 domain wall

$$p_\infty = \frac{P_0}{\sqrt{3}}$$

$$\begin{aligned} g &= G_{44} \\ a_1 &= \alpha_1 + \frac{\alpha_{12}^{(e)} P_0^2}{3} + \frac{\alpha_{112} P_0^4}{9} + \frac{2q_{12}^2 P_0^2}{3C_{11}} - \frac{q_{44}^2 P_0^2}{6C_{44}} \\ &\quad -e_a(q_{11} + 2q_{12}) - e_b q_{44} \\ a_{11} &= \frac{\alpha_{11}^{(e)}}{2} + \frac{\alpha_{12}^{(e)}}{4} + \frac{1}{12}\left[(2\alpha_{112} + \alpha_{123})P_0^2 - \frac{6q_{12}^2}{C_{11}}\right] \\ a_{111} &= \frac{\alpha_{111} + \alpha_{112}}{4} \end{aligned} \tag{3.30}$$

This domain wall is potentially not stable with respect to deviation of t-component of polarization. Ising assumption may not be correct. Domain wall of Bloch type may appear, instead (see Sec. 3.6 and appropriate graph of numerical solution in Fig. 3.14).

3.3.12 R71 domain wall

$$\begin{aligned} p_\infty &= \frac{P_0}{\sqrt{3}} \\ g &= G_{44} \\ a_1 &= \alpha_1 + \frac{2\alpha_{12}^{(e)} P_0^2}{3} + \frac{2\alpha_{112} P_0^4}{9} + \frac{\alpha_{123} P_0^4}{9} \\ &\quad -e_a(q_{11} + 2q_{12}) + \frac{q_{12}^2 P_0^2}{3C'_{33}} - \frac{q_{44}^2 P_0^2}{3C_{44}} \\ a_{11} &= \alpha_{11}^{(e)} + \frac{2\alpha_{112} P_0^2}{3} - \frac{q_{12}^2}{2C'_{33}} \\ a_{111} &= \alpha_{111} \end{aligned} \tag{3.31}$$

with C'_{33} same as in Eqn. 3.29.

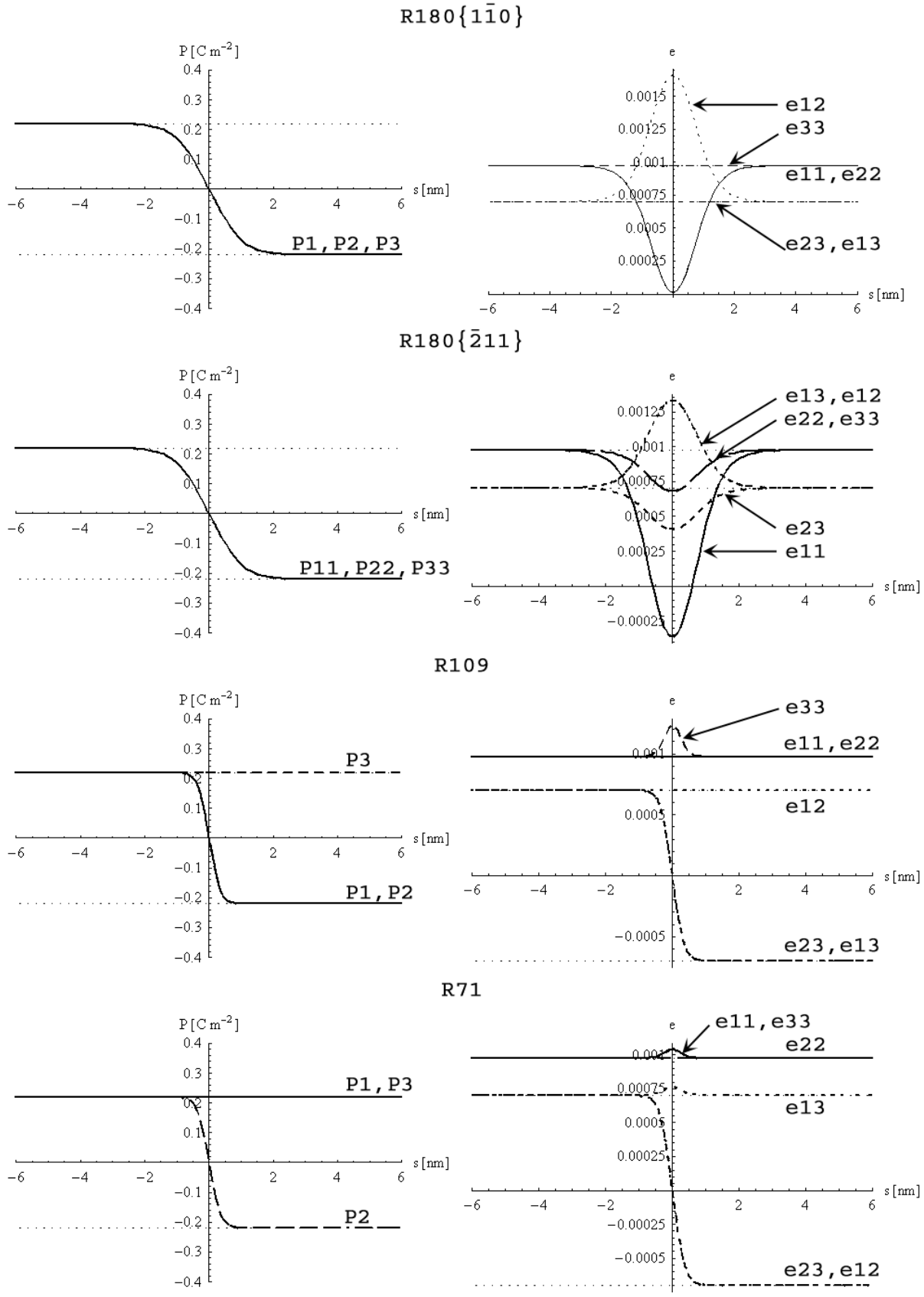

Figure 3.8: Analytical profiles of polarization and strain components inside the R180{1$\bar{1}$0}, R{$\bar{2}$11}, R109 and R71 walls.

Table 3.3: Parameters and computed values for inspected domain walls. † normal given in Tab. 3.2. Domain walls which are appropriate (boundary values corresponds to the global minima of Euler-Lagrange potential) for given ferroelectric phase are boldfaced. Domain walls, which are potentially unstable (see Sec. 3.6) with respect to deviation in t-component of polarization, have its names in parentheses.

Domain wall	2ξ (10^{-9} m)	Σ (10^{-3} $\frac{\mathrm{J}}{\mathrm{m}^2}$)	U (10^{6} $\frac{\mathrm{J}}{\mathrm{m}^3}$)	A (1)	p_∞ ($\frac{\mathrm{C}}{\mathrm{m}^2}$)	g (10^{-11} $\frac{\mathrm{kg\,m^5}}{\mathrm{s^2\,C^2}}$)	a_1 (10^{7} $\frac{\mathrm{kg\,m^3}}{\mathrm{s^2\,C^2}}$)	a_{11} (10^{8} $\frac{\mathrm{kg\,m^7}}{\mathrm{s^2\,C^4}}$)	a_{111} (10^{9} $\frac{\mathrm{kg\,m^{11}}}{\mathrm{s^2\,C^6}}$)
Tetragonal phase (298 K)									
T180{001}	**0.63**	**5.9**	**6.41**	**1.43**	**0.265**	**2.0**	**-14.26**	**1.69**	**8.00**
T180{011}	**0.63**	**5.9**	**6.41**	**1.43**	**0.265**	**2.0**	**-14.26**	**1.69**	**8.00**
T90	**3.59**	**7.0**	**1.45**	**1.09**	**0.188**	**26.5**	**-7.86**	**9.53**	**3.12**
O180{1$\bar{1}$0}	3.60	17.9	3.53	1.57	0.294	26.5	-5.87	-0.64	3.12
(O180{001})	0.93	5.2	3.99	1.50	0.294	2.0	-6.93	-0.02	3.12
O90	0.47	2.5	1.96	1.33	0.208	2.0	-7.59	3.62	8.00
O60	2.68	2.8	0.39	1.08	0.147	26.1	-3.47	7.04	3.12
(O120)	2.29	7.9	2.52	1.37	0.254	10.2	-6.35	1.60	3.41
Orthorombic phase (208 K)									
O180{1$\bar{1}$0}	**2.66**	**31.0**	**8.20**	**1.70**	**0.331**	**26.5**	**-9.71**	**-2.75**	**4.36**
(**O180{001}**)	**0.70**	**8.9**	**8.95**	**1.64**	**0.331**	**2.0**	**-11.67**	**-2.13**	**4.36**
O90	**0.72**	**4.3**	**4.26**	**1.50**	**0.234**	**2.0**	**-11.62**	**-0.08**	**12.97**
O60	**3.62**	**5.5**	**1.09**	**1.08**	**0.166**	**26.1**	**-7.64**	**12.14**	**4.36**
(**O120**)	**1.70**	**13.7**	**5.82**	**1.47**	**0.287**	**10.2**	**-10.82**	**0.50**	**4.92**
(R180{1$\bar{1}$0})	2.66	24.3	6.39	1.76	0.351	18.3	-6.41	-2.23	2.62
(R180{$\bar{2}$11})	2.66	24.3	6.39	1.76	0.351	18.3	-6.41	-2.23	2.62
(R109)	0.87	5.3	4.53	1.55	0.287	2.0	-7.66	-0.71	4.36
R71	0.91	2.5	1.99	1.45	0.203	2.0	-7.50	1.14	12.97
Rhombohedral phase (118 K)									
O180{1$\bar{1}$0}	2.22	41.6	13.11	1.78	0.349	26.5	-13.16	-4.86	5.60
(O180{001})	0.59	11.8	14.03	1.72	0.349	2.0	-14.66	-4.24	5.60
O90	0.61	5.7	6.64	1.61	0.247	2.0	-15.11	-4.02	17.94
O60	2.87	7.5	1.93	1.08	0.175	26.1	-12.17	17.38	5.60
(O120)	1.41	18.4	9.27	1.53	0.302	10.2	-14.93	-0.68	6.44
(**R180{1$\bar{1}$0}**)	**2.13**	**36.0**	**11.81**	**1.83**	**0.381**	**18.3**	**-9.53**	**-3.64**	**3.17**
(**R180{$\bar{2}$11}**)	**2.13**	**36.0**	**11.81**	**1.83**	**0.381**	**18.3**	**-9.53**	**-3.64**	**3.17**
(**R109**)	**0.70**	**7.8**	**7.81**	**1.65**	**0.311**	**2.0**	**-10.84**	**-2.56**	**5.60**
R71	**0.74**	**3.7**	**3.52**	**1.58**	**0.220**	**2.0**	**-10.31**	**-2.42**	**17.94**

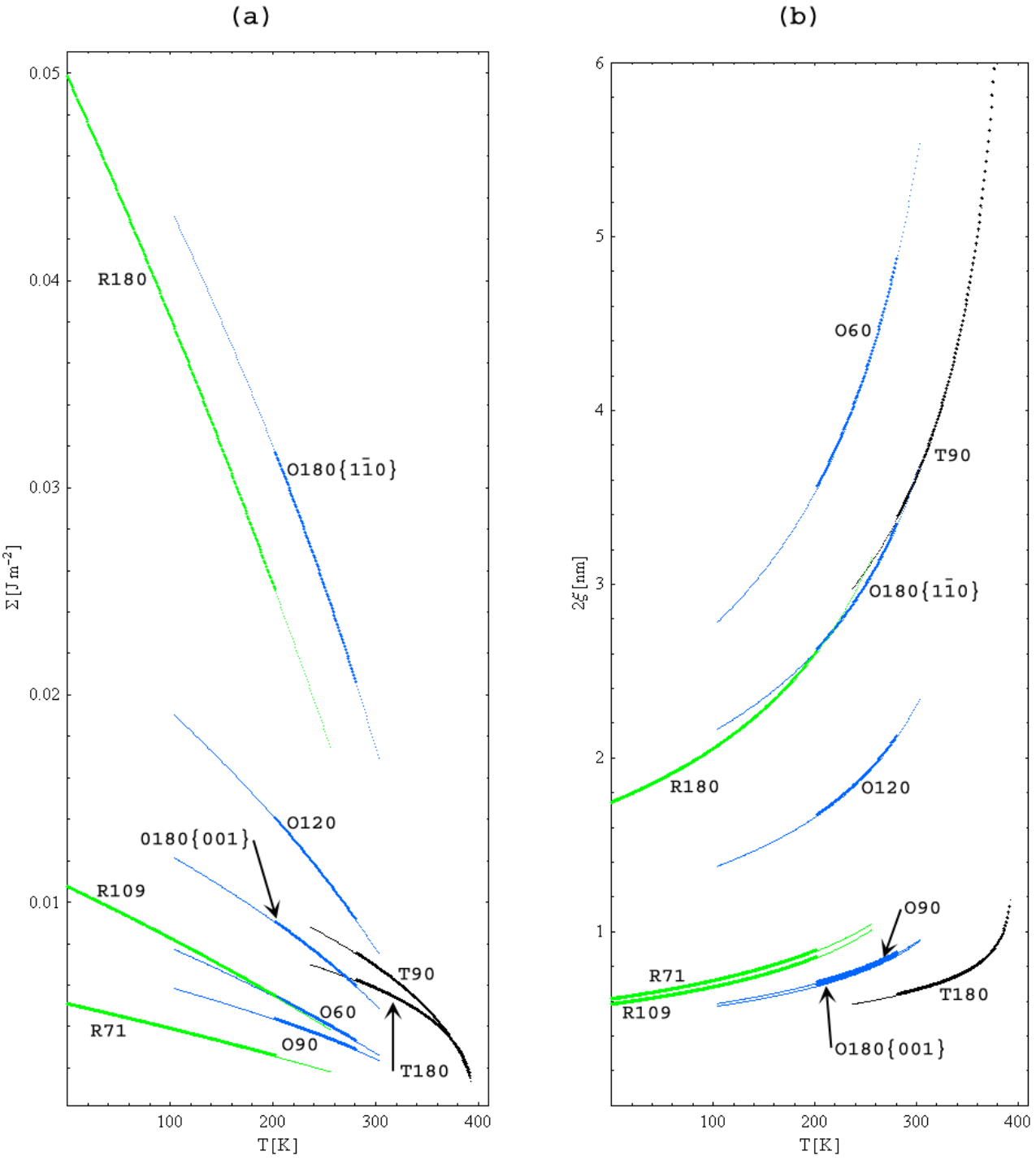

Figure 3.9: (a) Temperature dependence of domain wall energy per unit area. (b) Temperature dependence of domain wall thickness. Both pairs, (O180{001}, O90) and (T180{001}, T180{011}), have similar thickness in wide temperature range and almost merge. Thick lines indicates temperature wall thickness in the range of temperatures that are appropriate for given phase. Thin lines stands for temperature range where boundary states are in local, not global minima it the Euler-Lagrange potential.

Table 3.4: Range of variation of coefficients of W_∞ walls. The wall was rotated along the direction of spontaneous polarization in the whole range of angles. Coefficient a_{111} does not change. Minimum value, maximum value and their difference is given in the table.

Coefficient	Minimum	Maximum	Difference	Unit [SI]
		T180 (298 K)		
a_1	-14.2619	-14.2615	0.0004	10^7 J m C^{-2}
a_{11}	1.69068	1.69090	0.00022	10^8 J m^5 C^{-4}
g	2.0	2.0	0.0	10^{-11} J m^3 C^{-2}
		O180 (208 K)		
a_1	-11.07	-8.32	2.75	10^7 J m C^{-2}
a_{11}	-3.38	-2.13	12.54	10^8 J m^5 C^{-4}
g	2.0	26.5	24.5	10^{-11} J m^3 C^{-2}
		R180 (118 K)		
a_1	-9.53	-9.53	0	10^7 J m C^{-2}
a_{11}	-3.63985	-3.63970	0.00015	10^8 J m^5 C^{-4}
g	18.3	18.3	0.0	10^{-11} J m^3 C^{-2}

3.4 Angle dependence of W_∞ wall thickness

Thickness of domain walls is predominantly determined by the value of gradient coefficient g. Fig. 3.9 shows that the most narrower walls are R71, R109, O90, O180{001}, T180{001} and T180{011}. All of them have $g = 2 \times 10^{-11}$. Thickness of walls increase with increasing g. Equation (3.14) also implies thicker domain walls for materials with larger value of p_∞ (e.g. $PbTiO_3$).

In tetragonal phase, 90 degree domain wall is much thicket than 180 degree wall (3.59 nm compared to 0.63 nm). On the contrary, in orthorombic phase the domain wall O180[1-10] is almost four times thicker than 90 degree domain wall.

Summary of results is given in Tab. 3.3. Temperature dependence of thickness and energy for all domain walls are plotted in Fig. 3.9(a) and Fig. 3.9(b), resp. Energy of increases and thickness decrease with decreasing temperature. This is consequence of relations (3.16),(3.15),(3.14) and increasing value of p_∞ with decreasing temperature as shown in Fig. 2.1(c).

Non-ferroelastic 180 degree domain wall is not limited to any crystallographic direction. Generally, angular dependent coefficients g and also coefficients a_1, a_{11} and a_{111} can (if sufficiently anisotropic) cause change of domain wall thickness and energy. Gradient coefficient is not dependent on angle in tetragonal and rhombohedral phase and variation of Landau expansion coefficients is also insignificantly small (Tab. 3.4). On the contrary, in orthorombic phase there is a strong angular dependence of g and Euler-Lagrange coefficients leading to angular dependence of wall thickness as shown in Fig. 3.10. O180$\{1\bar{1}0\}$ domain wall is almost four times thicker compared to thickness of O180{001} wall.

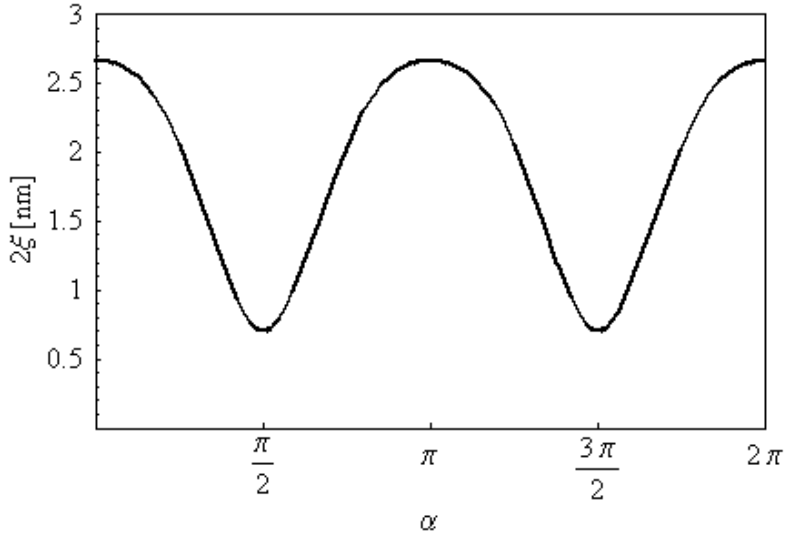

Figure 3.10: Angular dependence of 180 degree domain wall thickness in orthorombic phase phase. $\alpha = 0$ and $\alpha = \frac{\pi}{2}$ corresponds to O180$\{1\bar{1}0\}$ and O180$\{001\}$ wall, resp.

3.5 Discussion of the charge-free assumption

Assumption that P_s is constant may seem rather strong. In this paragraph we show for T90 domain wall that it is reasonable premise. The polarization is assumed in the form $\mathbf{P} = [P_r(s), P_s(s), P_t(\pm\infty)]$. Fixation of P_t will be explained in Sec. 3.6, it is no additional assumption. Two coupled Euler-Lagrange equations are obtained from mechanical equilibrium conditions (3.2) and Euler-Lagrange equation for polarization (3.5)

$$\begin{aligned} G'_{66}P_{r,ss} &= 2a_1^r P_r + 4a_{11}^r P r^3 + 6a'_{111}P_r^5 \\ &+ 2a_{12}^{rs}P_r P_s^2 + 4a'_{112}P_r^3 P_s^2 + 2a'_{112}P_r P_s^4 \\ G'_{11}P_{s,ss} &= 2a_1^s P_s + 4a_{11}^s P s^3 + 6a'_{111}P_s^5 \\ &+ 2a_{12}^{rs}P_r^2 P_s + 4a'_{112}P_r^2 P_s^3 + 2a'_{112}P_r^4 P_s \end{aligned} \tag{3.32}$$

with the same coefficients as derived in Eqn. 3.21 and additional two

$$\begin{aligned} a_1^s &= \alpha_1 - \left[\frac{1}{3}\frac{\hat{q}_{11}^2}{\hat{C}_{11}} + \frac{1}{6}\frac{\hat{q}_{22}^2}{\hat{C}_{22}} - \frac{(q_{11}+q_{12})q'_{11}}{2C'_{11}}\right]P_0^2 \\ a_{11}^s &= \frac{\alpha_{11}^{(e)}}{2} + \frac{\alpha_{12}^{(e)}}{4} - \frac{q'^2_{11}}{2C'_{11}} \ . \end{aligned} \tag{3.33}$$

Integration of both equations leads to an Euler-Lagrange potential

$$\begin{aligned} f'_{\mathrm{EL}}[P_r, P_s] &= a_1^r P_r^2 + a_1^s P_s^2 + a_{11}^r P_r^4 + a_{11}^s P_s^4 + a_{12}^{rs}P_r^2 P_s^2 \\ &+ a_{111}^{rs}(P_r^6 + P_s^6) + a_{112}P_r^2 P_s^2(P_r^2 + P_s^2) \ , \end{aligned} \tag{3.34}$$

which is plotted in the Fig. 3.11(a). Electrostatic interaction is taken into account by including

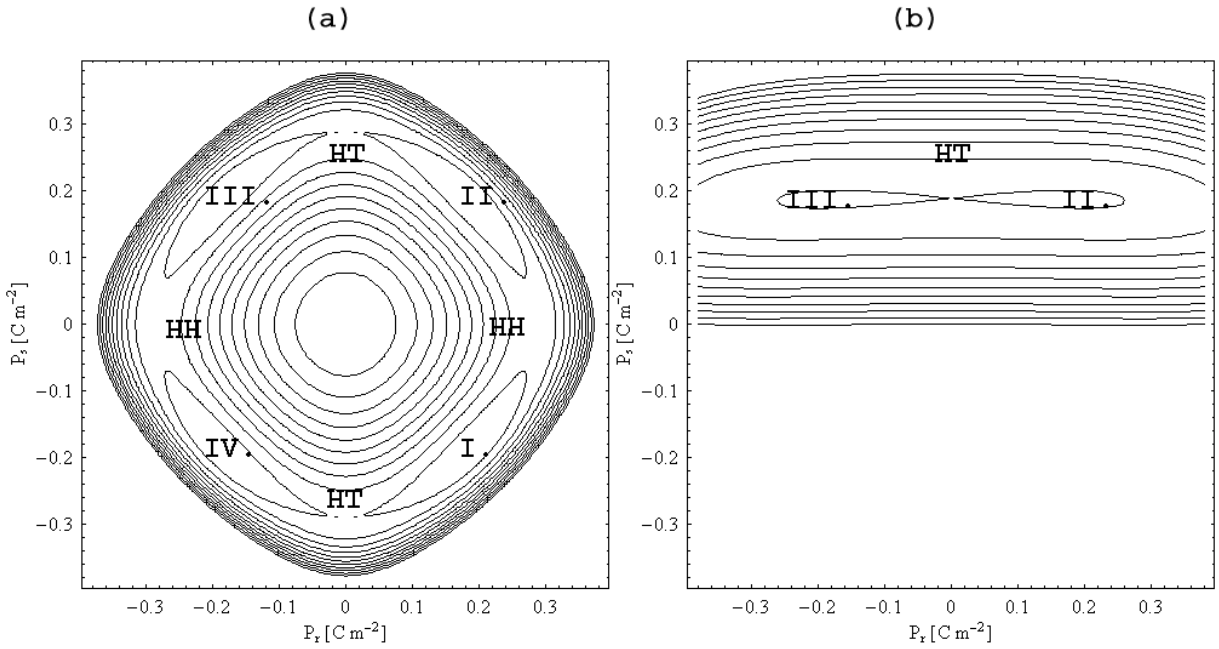

Figure 3.11: Euler-Lagrange potential for T90 wall in $BaTiO_3$; (a) Without depolarization field; (b) With depolarization field. From (a), it is clear that head-to-tail (HT) domain wall is not equivalent with head-to-head (HH) domain wall even without depolarization field (see Ref. [26]). With depolarization field included in (b), there remains only head-to-tail domain wall connecting potential wells II. and III. Contours are distributed linearly.

effect of depolarization electric field. It is computed from Eqn. 2.52 as

$$\mathbf{E}_{\mathrm{dep}} = \left[0, \frac{1}{\epsilon_B \epsilon_0}(-P_s + C_{\mathrm{dep}}), 0\right] \ . \tag{3.35}$$

Integration constant is computed (from condition $E_{\mathrm{dep}}(\pm\infty) = 0$) as $C_{\mathrm{dep}} = P_0/\sqrt{2}$. Electric field is added to Landau potential and the integration is performed. Resulting Euler-Lagrange potential differs only in additional parabolic term in P_s

$$f'_{\mathrm{ELdep}}[P_r, P_s] = f'_{EL}[P_r, P_s] + \frac{1}{2\epsilon_B\epsilon_0}P_s^2 - \frac{1}{\epsilon_B\epsilon_0}\frac{P_0}{\sqrt{2}}P_s \tag{3.36}$$

that, however, totally changes the shape of potential (cross sections of original and changed potential for $P_r = 0$ is shown in Fig. 3.12. Without electrostatic dipole-dipole interaction there are all tetragonal minima present in the Euler-Lagrange potential, but with electrostatic interaction taken into account there persist only minima corresponding to head-to-tail wall. Positions of tetragonal minima remains the same. Least energy path from one minima to the second exhibits almost no variation in P_{s}. It justifies our restriction to ideally charge-free wall with P_s constant.

3.6 Discussion of the Ising assumption

Assumption div $\mathbf{P} = 0$ and just one varying component of polarization through domain wall implies $P_r = P_r(s)$, $P_s = P_s(\pm\infty)$ and $P_t = P_t(\pm\infty)$.

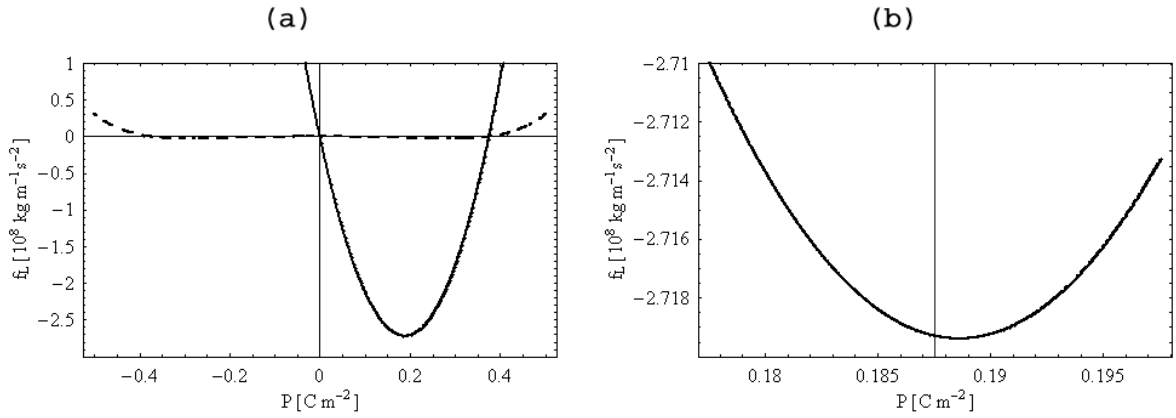

Figure 3.12: (a) Cross section of Euler-Lagrange potential (from Fig. 3.11) for $P_r = 0$. Dashed and full line stands for potential with and without depolarization field, resp. (b) Detail taken from the left plot. Minimum is still slightly shifted from $P_s = P_s/\sqrt{2}$ (value for charge-free domain wall) that is indicated by vertical line.

In fact, there is no reason for P_t to stay constant. Legitimacy of this assumption was therefore examined. The premise of constant P_s remains. Cross-section of Euler-Lagrange[3] potential is plotted in the Fig. 3.13 for temperature corresponding to given ferroelectric phase. Minima of the potential for $[P_r = P_r(+\infty), P_t = 0]$ and $[P_r = P_r(-\infty), P_t = 0]$ correspond to polarization boundary conditions. The only exception is the O60 domain wall, where the boundary values for P_t are non-zero and positive (for boundary conditions consult Tab. 3.2 and appropriate transformation matrices in Sec. E.3). Minima of the Euler-Lagrange potential corresponding to boundary values of polarization are global minima. All minima in the potential corresponds to appropriate phase (e.g. for orthorombic wall there are only orthorombic minima, etc.) with the only exception: side minima in the case of R180$\{\bar{2}11\}$ wall are orthorombic minima. Potential takes into account Landau, elastic and electrostriction contributions, dipole-dipole is taken into account by constant P_s. Components P_r and P_t of polarization find appropriate trajectory in order to minimize simultaneously energy from Euler-Lagrange potential and gradient interaction.

From Fig. 3.13, it is clear that T180, T90, O180$\{1\bar{1}0\}$, O90, O60 and R71 domain walls have unique trajectory from one boundary minimum to the second. One-dimensional assumption is appropriate in these cases and $P_t = P_t(\pm\infty)$.

In the case of O60 domain wall the variation of P_t will be very small and therefore it is reasonable to assume it constant.

For O180$\{001\}$, O120, R180$\{1\bar{1}0\}$, R180$\{\bar{2}11\}$ and R109 wall, the situation is different. Straight connection of boundary minima (through the paraelectric state) is energetically demanding and the polarization in the wall can tend to go around the energy maximum in the middle of the potential. It would decrease Euler-Lagrange energy (at the expense of increase of gradient energy). Therefore $P_t = P_t(s)$ and the wall may be Bloch-like[4]. Another point is that all these walls have relatively high energy (see Fig. 3.9(a)) and therefore lower-energy Bloch variant of the particular wall may be suspected to appear.

[3]Landau potential renormalized by elastic and electrostriction interaction assuming mechanical equilibrium.

[4]Bloch wall exhibits two-dimensional variation of polarization through a domain wall: Polarization rotates in the plane of the wall while normal component to the wall remains zero.

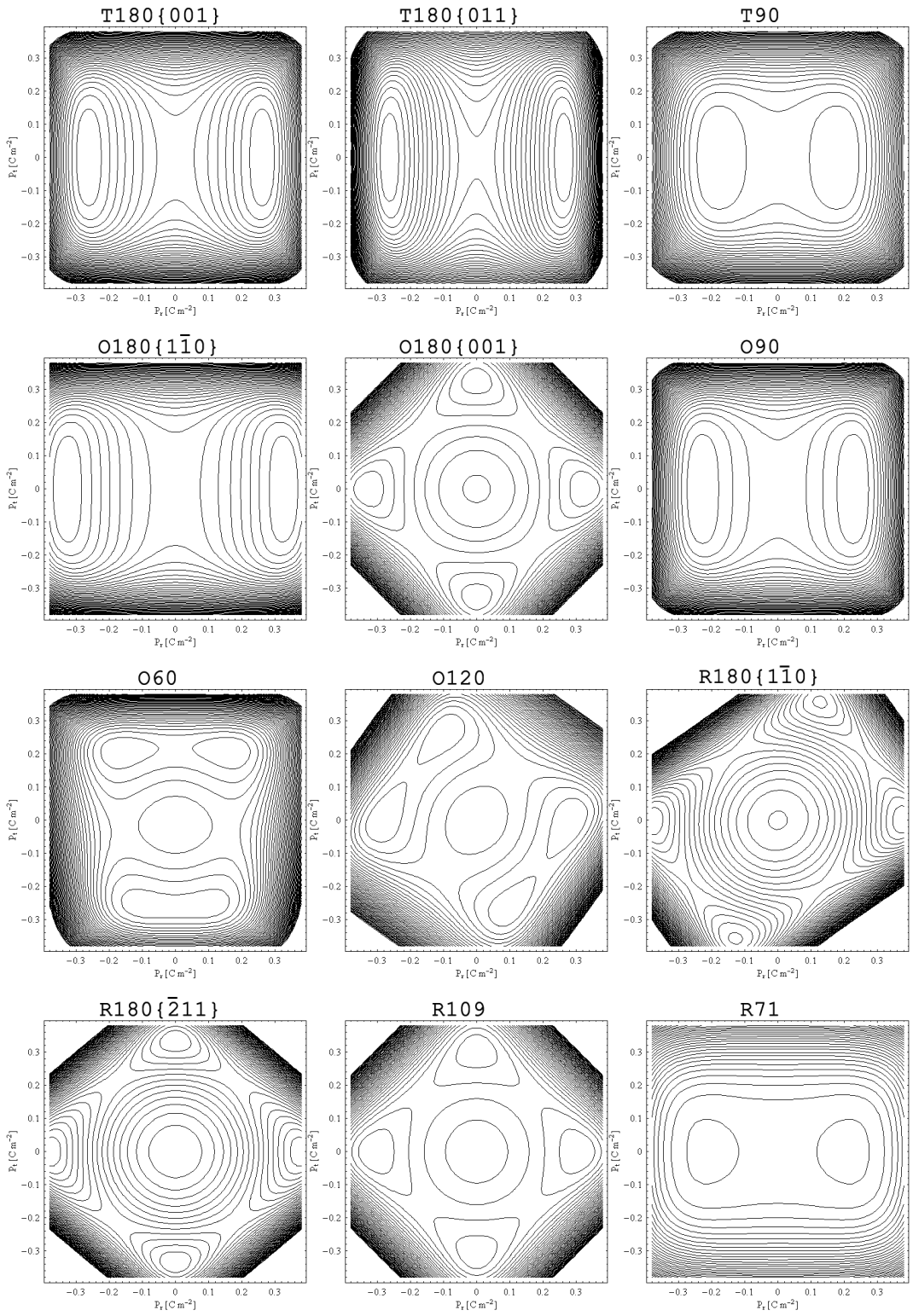

Figure 3.13: Cross sections of Euler-Lagrange potential perpendicular to the direction of domain walls in $BaTiO_3$. In all cases the boundary value of $P_t(\pm\infty)$ is zero, the only exception is O60 degree domain wall where $P_t(\pm\infty)$ is positive. Exact values can be obtained from Tab. A.1Walls O180{001}, O120, R180{1$\bar{1}$0}, R180{$\bar{2}$11} and R109 with side minima corresponding to another spontaneous states appropriate for give phase enables for Bloch domain wall. Side minima are slightly more shallow than minima of boundary states. Contours are distributed linearly.

Analytical solution for two varying components of polarization $P_r(s)$, $P_t(s)$ does not exist, numerical simulation of domain wall profile was performed. Initial conditions were chosen so that $[P_r(s), P_t(s)]$ trajectory goes around the middle peak in energy: $P_r(s)$ component linearly connects values $P_r(-\infty)$ and $P_r(+\infty)$, $\mathrm{P}_t(s)$ is a gaussian curve ($P_t(\pm\infty) = 0$) and finally P_s is fixed to the boundary value (charge-free assumption). The system was then relaxed to the equilibrium. Results are plotted in Fig. 3.14. Polarization component P_t changes through a domain wall.

In the case of O180{001}, R180{$1\bar{1}0$}, R180{$\bar{2}11$} and R109 domain wall, the Bloch-like solution was as expected. $P_t(s)$ starts from one boundary state, almost reach side minimum, and continues to the second boundary state. In all these cases it seems that there exists another solution of Euler-Lagrange equations, which goes over the potential maximum for $\mathbf{P} = 0$.

O120 domain wall, on the contrary, exhibits only one solution (which reach potential maximum for $\mathbf{P} = 0$. $P_t(s)$ changes its sign in the middle of the domain wall for $P_r = 0$.

It will be necessary to check for energy of individual trajectories of in order to decide which is absolutely stable solution of Euler-Lagrange equations.

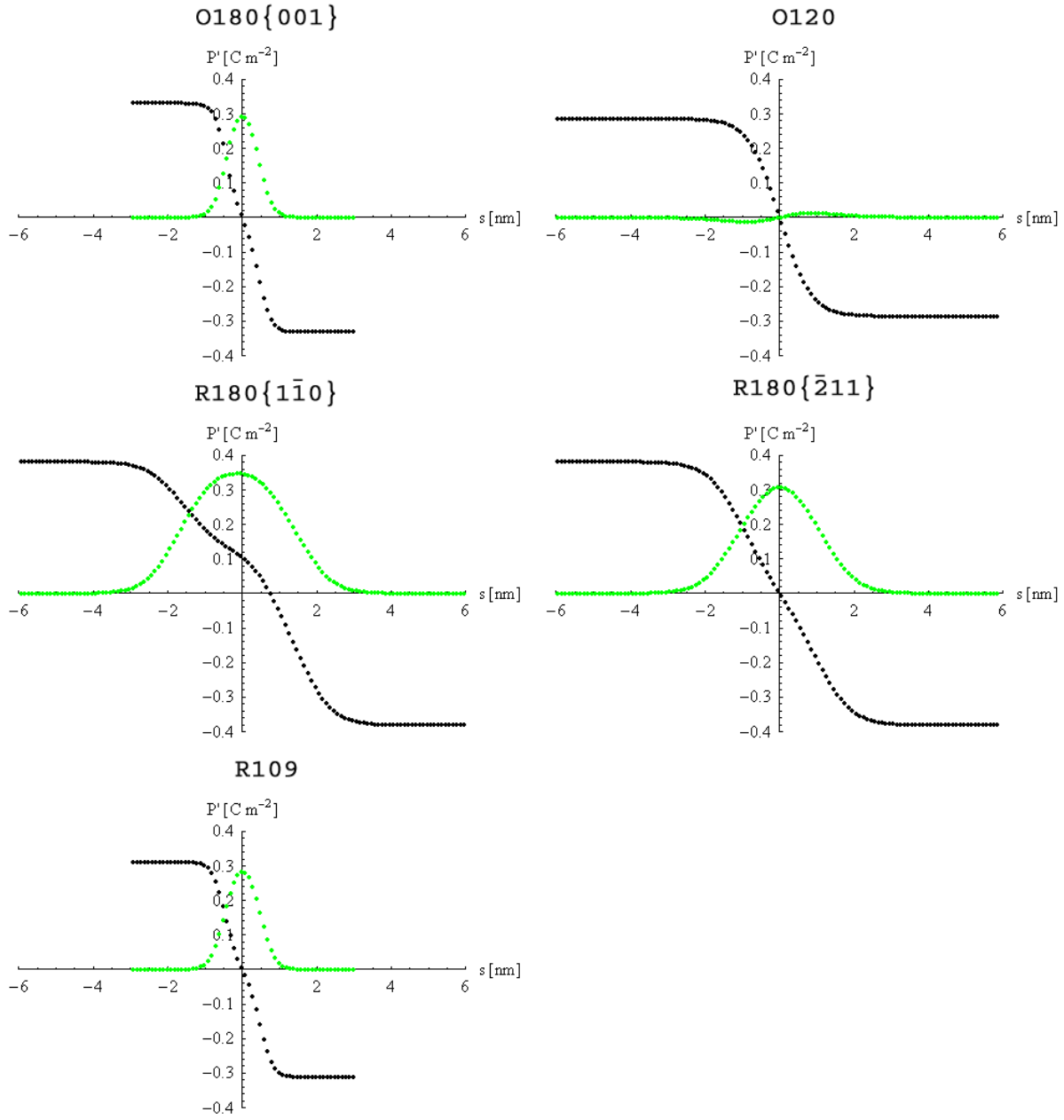

Figure 3.14: Bloch solution of Euler-Lagrange equation for O180{001}, O120, R180{1$\bar{1}$0}, R180{$\bar{2}$11} and R109 domain walls. Profiles were obtained numerically. Black and green curves represent r and t-component of polarization vector. Component s is kept constant, domain wall is charge-free.

Chapter 4

Dynamics of polarization field

4.1 Lattice contribution to the dielectric constant in $BaTiO_3$

There are three basic mechanisms which contributes to the dielectric constant in ferroelectric material: High-frequency electronic polarizability, contribution from lattice vibrations – phonons at approximately THz frequencies and reorientation of polarization at lowest frequencies. Dynamics of polarization in $BaTiO_3$ is determined by lattice vibrations dynamics (especially by modes with lower frequency as is derived in following text).

Polarizability of a material can be inspected by probing of a dielectric response. Frequency-dependent dielectric function can be evaluated from reflection spectra (Fig. 4.1 from Ref. [41] shows reflection spectra for $BaTiO_3$) using Fresnel equation for reflected light in the air

$$R(\omega) = \left| \frac{\sqrt{\epsilon(\omega)} - 1}{\sqrt{\epsilon(\omega)} + 1} \right| . \tag{4.1}$$

Relation between permittivity and optic index of the material for non-magnetic materials is $n(\omega) = \sqrt{\epsilon(\omega)}$. Imaginary part of $R(\omega)$ can be obtained from Kramers-Kronig relations. Complex permittivity was fitted by factorized form of the dielectric function that takes into account contributions from individual optic modes[1]

$$\epsilon(\omega) = \epsilon_\infty \prod_j \frac{\Omega_{jLO}^2 - \omega^2 + i\omega\gamma_{jLO}}{\Omega_{jTO}^2 - \omega^2 + i\omega\gamma_{jTO}} \tag{4.2}$$

involving transverse optic (TO) mode frequency Ω_{jTO} and damping γ_{jTO} constants, longitudinal optic (LO) mode frequency Ω_{jLO} and damping γ_{jLO}. Dielectric strength of the j-th oscillator is computed from fitted parameters using relation

$$\Delta\epsilon_j = \epsilon_\infty \left(\frac{\Omega_{jLO}^2}{\Omega_{jTO}^2} - 1 \right) \prod_{k \neq j} \frac{\Omega_{kLO}^2 - \Omega_{jTO}^2}{\Omega_{kTO}^2 - \Omega_{jTO}^2} = \frac{S_j}{\Omega_{jTO}^2} \tag{4.3}$$

with oscillator strength [42]

$$S_j = \epsilon_\infty \frac{\prod_k \Omega_{kLO}^2 - \Omega_{jTO}^2}{\prod_{k \neq j} \Omega_{kTO}^2 - \Omega_{jTO}^2} . \tag{4.4}$$

[1] Acoustic phonons do not contribute to the dielectric response.

Table 4.1: Frequency, damping and dielectric strength of optic modes in tetragonal phase. Dielectric strengths of oscillators are computed from Eqn. 4.3 with use of fitted Ω_j and γ_j. Data taken from Ref. [41].

Vibrational mode	Ω_j	γ_j	$\Delta\epsilon_j$
$TO_1(E)$	34	100	2000
$LO_1(E)$	80	9	
$TO_2(E)$	181.8	2.8	1.4
$LO_2(E)$	305.6	9	
$TO_3(E)$	306	9	0.05
$LO_3(E)$	465	5	
$TO_4(E)$	482	21	0.4
$LO_4(E)$	706	22	

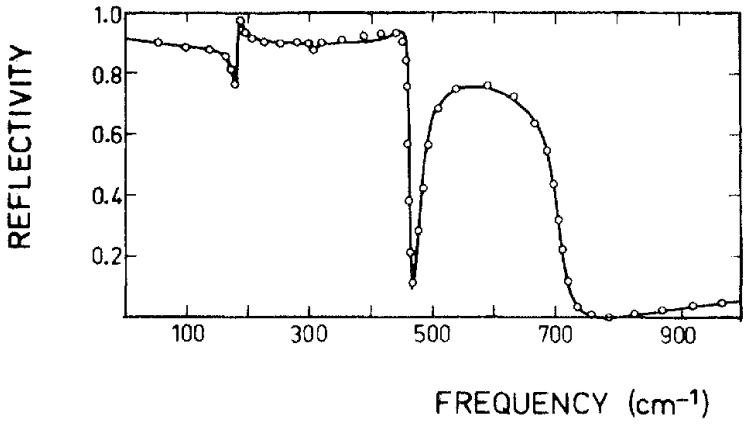

Figure 4.1: Reflection spectra (circles) of $BaTiO_3$ at room temperature (tetragonal phase). Fit with parameters from Tab. 4.1 is indicated by solid line. Figure was taken from Ref. [41], where the reflection data were collected from mono-domain single-crystal.

Static permittivity is expressed in terms of optic permittivity and individual contributions of all polar modes

$$\epsilon_0 = \epsilon(\omega = 0) = \epsilon_\infty + \sum_j \frac{S_j}{\Omega_{jTO}^2} \tag{4.5}$$

Five atoms in a primitive unit cell of $BaTiO_3$ (Fig. 1.5) imply existence of fifteen lattice vibrational modes: twelve optic and three acoustic ones. Longitudinal and transversal optic mode frequencies, dampings and dielectric strengths as measured in tetragonal phase are plotted in Tab. 4.1. Dynamics of polarization is governed by the dynamics of $TO_1(E)$[2] mode (so called Slatter mode). Its dielectric strength is by far the biggest in tetragonal phase. Eigenvector of Slatter mode for room temperature is shown in Fig. 4.2. This mode comes from splitting of cubic Slatter mode with symmetry F_{1u}, which is parent mode for modes with biggest dielectric strength in the whole temperature range. Existence of the mode with low vibrational frequency

[2]E stands for the name of irreducible representation which determine mode transformational properties.

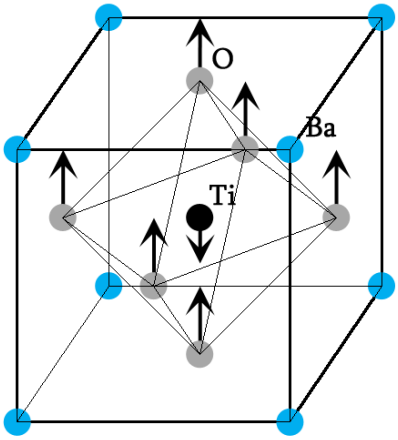

Figure 4.2: Slatter mode which is the soft mode for cubic-to-tetragonal phase transition in $BaTiO_3$.

is explained by so-called soft mode concept.

4.2 Soft mode concept

In the case of displacive phase transitions there exists a lattice vibrational mode whose frequency decrease (softens) when approaching the phase transition temperature. The mode softens in the middle of the Brillouin zone if the phase transition is ferrodistorsive (the case of $BaTiO_3$) or e.g. at the zone boundary for anti-ferrodistortive transition.

When approaching the cubic-to-tetragonal phase transition temperature from above, soft mode frequency follows Cochran law

$$\Omega_{sTO}^2 = A\,(T - T_c)\ , \tag{4.6}$$

where T_c is the Curie temperature[3]. Susceptibility divergence (Curie-Weiss behavior) on cooling at T_c is a consequence of Eqn. 4.5.

On further cooling, ω would become negative. It indicates that the system is at the potential energy maximum with respect to the distortion of the structure with the eigenvector of the soft mode. Mode displacement freezes(the structure relaxes), and then mode[4] hardens again on cooling down.

Existence of soft mode follows also from Lyddane-Sachs-Teller relation[45]

$$\frac{\epsilon_0}{\epsilon_\infty} = \prod_k \frac{\Omega_{k\,LO}^2}{\Omega_{k\,TO}^2}\ . \tag{4.7}$$

Divergence of $\epsilon(\omega = 0)$ implies existence of a transversal mode with property $\Omega_{sTO}^2 \to 0$. In $BaTiO_3$, the Slatter[5] mode is the soft mode for cubic to tetragonal phase transition. The cubic vibrational mode with symmetry F_{1u} is also responsible for displacive character of tetragonal to orthorombic and orthorombic to rhombohedral phase transitions. Other modes are almost temperature independent.

[3] In the case of first-order phase transition it differs from phase transition temperature.
[4] The soft mode splits into two parts – longitudinal and transversal.
[5] Slatter mode in $BaTiO_3$ denotes motion of titan with respect to oxygen

Chapter 5

Landau-Khalatnikov equation

Dynamics of polarization is driven by the lattice mode with the biggest dielectric strength. Extraordinary value of $\Delta\epsilon_{sTO}$ in $BaTiO_3$ compared to remaining vibrations indicates that the dynamics of polarization is determined by the dynamics the soft mode. Frequency γ_{sTO} and damping Ω_{sTO} fulfill relation

$$\gamma_{sTO} > 2\Omega_{sTO} \tag{5.1}$$

and the mode is therefore over-damped.

Consequently, the evolution of the system is assumed to be driven by the dissipative time-dependent Landau-Khalatnikov equation [43]

$$\frac{\partial}{\partial t}P_i(\mathbf{r},t) = -\Lambda\frac{\delta F'}{\delta P_i}(\mathbf{r},t) + \xi_i(\mathbf{r},t)\ , \tag{5.2}$$

where $F'\left[\{P_i(\mathbf{r},t)\}\right]$ is the free energy functional with eliminated elastic part (2.35) and $\xi_i(\mathbf{r},t)$ stands for random force (which is neglected in our computations). Kinetic coefficient Λ was estimated in the Ref. [44] to about $\Lambda = 4\times10^4\ \mathrm{C^2\,kg^{-1}\,m^{-3}\,s}$.

Landau-Khalatnikov equation is an ordinary differential equation in time and can be solved (for given initial and boundary conditions) for polarization field. Since the free energy is obtained by integration over sample domain, variation of energy functional must be computed to get generalized force at the right-hand side of Landau-Khalatnikov equation. Explicit expressions for generalized force used in simulations are derived in this chapter and Sec. C.

5.1 Landau-Khalatnikov Equation in Fourier space

In principle, evolution of $P_i(\mathbf{r})$ field can be calculated straightforwardly from Eqn.5.2, but in the case of periodic boundary conditions in a bulk system, it is convenient to solve an equivalent equation for Fourier components of $P_i(\mathbf{r})$

$$\frac{\partial}{\partial t}\mathcal{F}\left[P_i(\mathbf{r})\right](\mathbf{k},t) = -\Lambda\mathcal{F}\left[\frac{\delta F'}{\delta P_i}(\mathbf{r})\right](\mathbf{k},t)\ , \tag{5.3}$$

since applying discrete Fourier transform greatly simplifies numerical calculations of the long-range forces. It is also favourable from numerical point of view since spectral methods exhibits excellent spatial convergence (perfect agreement with analytical profile even for rough grid

spacing [46, 32]). This approach requires evaluation of Fourier transform of the functional derivative on the right hand side of the Eqn. 5.2

$$\mathcal{F}\left[\frac{\delta F'}{\delta P_i}\right] = \mathcal{F}\left[\frac{\delta F_{\mathrm{L}}^{(\mathrm{e})}}{\delta P_i}\right] + \mathcal{F}\left[\frac{\delta F_{\mathrm{G}}}{\delta P_i}\right] + \mathcal{F}\left[\frac{\delta F'_{\mathrm{Cq}}}{\delta P_i}\right] + \mathcal{F}\left[\frac{\delta F_{\mathrm{dep}}}{\delta P_i}\right] . \tag{5.4}$$

Equations (5.3),(5.4) are equally valid for discrete Fourier transform. Definition of forward and backward discrete three-dimensional Fourier transform $\mathcal{F}_{\mathrm{d}}$ is given explicitly in Sec. B by Eqn. B.8.

On the right hand side of the Eqn. 5.4, there are contributions to a generalized force acting on polarization field. In a numerical approach we search for force acting on each individual discrete point.

5.1.1 Landau energy

Variation in real space is given in Eqn. C.1. Mutual multiplications of $P_i(\mathbf{r})$ in real space corresponds to convolution of Fourier images $P_i(\mathbf{k})$. Computation in reciprocal space would lead to multiple time-demanding convolutions. Therefore, this part is evaluated in direct space with polarization field $P_i(\mathbf{r}) = \mathcal{F}^{-1}[P_i(\mathbf{k})]$. At the end, forward Fourier transform is used to transform Landau force into the reciprocal space.

$$\begin{aligned}\mathcal{F}\left[\frac{\delta F_{\mathrm{L}}^{(e)}[\{P_i\}]}{\delta P_1}\right] &= \mathcal{F}\Big[\mathcal{F}^{-1}[P_1]\left[2\alpha_1 + 4\alpha_{11}\left(\mathcal{F}^{-1}[P_1]\right)^2\right. \\ &+ \left. 2\alpha_{12}\left[\left(\mathcal{F}^{-1}[P_2]\right)^2 + \left(\mathcal{F}^{-1}[P_3]\right)^2\right] + ...\right]\Big] .\end{aligned} \tag{5.5}$$

Similar expressions hold for variation with respect to P_2 and P_3 components of polarization field.

5.1.2 Gradient energy

Functional derivative of gradient energy functional in direct space is derived (Sec. C.2)

$$\frac{\delta F_{\mathrm{G}}[\{P_{i,j}\}]}{\delta P_1} = -G_{11}\frac{\partial^2 P_1}{\partial x^2} - G_{14}\left(\frac{\partial^2 P_2}{\partial x \partial y} + \frac{\partial^2 P_3}{\partial x \partial z^2}\right) - G_{44}\left(\frac{\partial^2 P_1}{\partial y^2} + \frac{\partial^2 P_1}{\partial z^2}\right) , \tag{5.6}$$

and remaining derivatives follows simply from cyclic permutation of indexes. Since differentiation in direct space correspond to multiplication by $i\mathbf{k}$ in Fourier space, resulting Fourier-transformed gradient force is

$$\mathcal{F}\left[\frac{\delta F_{\mathrm{G}}[\{P_{i,j}\}]}{\delta \mathbf{P}}\right](\mathbf{k}) = \mathbf{G}\mathbf{P}(\mathbf{k}) , \tag{5.7}$$

with

$$\mathbf{G} = \begin{bmatrix} G_{11}k_1^2 + G_{44}\left(k_2^2 + k_3^2\right) & G_{14}k_1k_2 & G_{14}k_1k_3 \\ G_{14}k_1k_2 & G_{11}k_2^2 + G_{44}\left(k_1^2 + k_3^2\right) & G_{14}k_2k_3 \\ G_{14}k_1k_3 & G_{14}k_2k_3 & G_{11}k_3^2 + G_{44}\left(k_1^2 + k_2^2\right) \end{bmatrix} . \tag{5.8}$$

Gradient part of generalized force is computed as a product of $\mathbf{P}(\mathbf{k})$ with a quadratic polynomial in k_i. This is used in variants of semi-implicit numerical scheme described in Sec. 6.1.

5.1.3 Elastostriction energy

Calculation in reciprocal space enables computation of long-range elastostriction forces by multiplication of $P_i(\mathbf{k})$ with elastostriction kernels $A_{\rho\sigma}(\hat{\mathbf{k}})$ defined by Eqn. 2.37 and given explicitly in Sec. D. Symmetry of matrix of kernels $A_{\rho\sigma}(\hat{\mathbf{k}})$ ($A_{\rho\sigma}(\hat{\mathbf{k}}) = A_{\sigma\rho}(\hat{\mathbf{k}})$ - see the definition in [18]) is important for derivation (Sec. C.3) of formulas for generalized elastostriction force in Fourier space:

$$\begin{aligned}\mathcal{F}\left[\frac{\delta F'_{\mathrm{Cq}}\left[\{P_i\}\right]}{\delta P_1}\right] &= -\frac{1}{2}\mathcal{F}\Bigg[4P_1\mathcal{F}^{-1}\left[\sum_{\sigma=1}^{6} A_{1\sigma}\mathcal{F}\left[Y_\sigma\right]\right] + 2P_2\mathcal{F}^{-1}\left[\sum_{\sigma=1}^{6} A_{6\sigma}\mathcal{F}\left[Y_\sigma\right]\right] \\ &\quad +2P_3\mathcal{F}^{-1}\left[\sum_{\sigma=1}^{6} A_{5\sigma}\mathcal{F}\left[Y_\sigma\right]\right]\Bigg] \qquad (5.9)\end{aligned}$$

$$\begin{aligned}\mathcal{F}\left[\frac{\delta F'_{\mathrm{Cq}}\left[\{P_i\}\right]}{\delta P_2}\right] &= -\frac{1}{2}\mathcal{F}\Bigg[4P_2\mathcal{F}^{-1}\left[\sum_{\sigma=1}^{6} A_{2\sigma}\mathcal{F}\left[Y_\sigma\right]\right] + 2P_3\mathcal{F}^{-1}\left[\sum_{\sigma=1}^{6} A_{4\sigma}\mathcal{F}\left[Y_\sigma\right]\right] \\ &\quad +2P_1\mathcal{F}^{-1}\left[\sum_{\sigma=1}^{6} A_{6\sigma}\mathcal{F}\left[Y_\sigma\right]\right]\Bigg] \qquad (5.10)\end{aligned}$$

$$\begin{aligned}\mathcal{F}\left[\frac{\delta F'_{\mathrm{Cq}}\left[\{P_i\}\right]}{\delta P_3}\right] &= -\frac{1}{2}\mathcal{F}\Bigg[4P_3\mathcal{F}^{-1}\left[\sum_{\sigma=1}^{6} A_{3\sigma}\mathcal{F}\left[Y_\sigma\right]\right] + 2P_1\mathcal{F}^{-1}\left[\sum_{\sigma=1}^{6} A_{5\sigma}\mathcal{F}\left[Y_\sigma\right]\right] \\ &\quad +2P_2\mathcal{F}^{-1}\left[\sum_{\sigma=1}^{6} A_{4\sigma}\mathcal{F}\left[Y_\sigma\right]\right]\Bigg] . \qquad (5.11)\end{aligned}$$

In two dimensions there are $A_{\rho\sigma}(\hat{\mathbf{k}})$ kernels nonzero where $\rho, \sigma \in \{1, 2, 6\}$, which corresponds to nonzero positions in vector $\mathbf{Y} = [P_1^2, P_2^2, 0, 0, 0, P_1P_2]$.

$$\mathcal{F}\left[\frac{\delta F'_{Cq}\left[\{P_i\}\right]}{\delta P_1}\right] = -\frac{1}{2}\mathcal{F}\left[4P_1\mathcal{F}^{-1}\left[\sum_{\sigma=1}^{6} A_{1\sigma}\mathcal{F}\left[Y_\sigma\right]\right] + 2P_2\mathcal{F}^{-1}\left[\sum_{\sigma=1}^{6} A_{6\sigma}\mathcal{F}\left[Y_\sigma\right]\right]\right] , \qquad (5.12)$$

$$\mathcal{F}\left[\frac{\delta F'_{Cq}\left[\{P_i\}\right]}{\delta P_2}\right] = -\frac{1}{2}\mathcal{F}\left[4P_2\mathcal{F}^{-1}\left[\sum_{\sigma=1}^{6} A_{2\sigma}\mathcal{F}\left[Y_\sigma\right]\right] + 2P_1\mathcal{F}^{-1}\left[\sum_{\sigma=1}^{6} A_{6\sigma}\mathcal{F}\left[Y_\sigma\right]\right]\right] . \qquad (5.13)$$

Kernels $A_{\rho\sigma}(\hat{\mathbf{k}})$ are defined as 0 for $\mathbf{k} = \mathbf{0}$ point of reciprocal space: elastostriction interaction acts only on the heterogeneous part of polarization here. Forces due to heterogeneous strain or stress are taken into account through anisotropy of coefficient $\alpha_1 \rightarrow (\alpha_{1x}, \alpha_{1y}, \alpha_{1z})$ and additional coefficients $(\beta_x, \beta_y, \beta_z)$ in Landau potential as described in Sec. 2.4.

5.1.4 Dipole-dipole electrostatic energy

Functional derivative of dipole-dipole electrostatic part of energy can be written (Eqn. C.12) as

$$\frac{\delta F_{\mathrm{dep}}\left[\{P_i\}\right]}{\delta P_i} = \frac{2}{8\pi\epsilon_0\epsilon_{\mathbf{B}}}\int \mathrm{d}\mathbf{s}\left[\frac{P_i(\mathbf{s})}{|\mathbf{R}|^3} - \frac{R_i\left[\mathbf{P}(\mathbf{s})\cdot\mathbf{R}\right]}{|\mathbf{R}|^5}\right] , \qquad (5.14)$$

using $\mathbf{R} = \mathbf{s} - \mathbf{r}$. Searched expression for variation in Fourier space is obtained as

$$\mathcal{F}\left[\frac{\delta F_{\text{dep}}\left[\{P_i\}\right]}{\delta P_i}\right] = \frac{2}{8\pi\epsilon_0\epsilon_{\mathbf{B}}}\frac{\left(\mathbf{P}(\mathbf{k})\cdot\mathbf{k}\right)k_i}{k^2} \ . \tag{5.15}$$

The right-hand side is defined as zero for $k = 0$, because for periodic boundary condition there is no force coming from homogeneous part of polarization.

Chapter 6

Implementation details of computer programs

6.1 Numerical methods for solving Landau-Khalatnikov equation

Landau-Khalatnikov governing equation (irrespective whether in direct or Fourier space) is first-order ordinary differential equation of the form

$$\frac{\partial \mathbf{P}(\mathbf{x},t)}{\partial t} = f(\mathbf{P}(\mathbf{x},t)) \ , \tag{6.1}$$

with initial conditions $\mathbf{P}(\mathbf{x},t_0) = g(\mathbf{x})$. Here $\mathbf{P}(\mathbf{x},t)$ is field of order parameters and $f(\mathbf{P}(\mathbf{x},t))$ is generalized force (in our case originating from Landau, gradient, elastic, electrostriction and dipole-dipole interaction). To solve the Eqn. 6.1 numerically, the space is equidistantly discretized with step Δ. Time discretization is also equidistant with step τ. Computed $\mathbf{P}(\mathbf{x}, n\tau)$ will be referred to as $\mathbf{P}^n$ and the dependence on space coordinate will not be emphasized. Simplest explicit first-order Euler method

$$\begin{aligned} \mathbf{P}^{n+1} &= \mathbf{P}^n + \tau f(\mathbf{P}^n) \\ \mathbf{P}^0 &= g^0 \end{aligned} \tag{6.2}$$

or second-order

$$\begin{aligned} \mathbf{P}^{n+1} &= \frac{1}{3}\left[4\mathbf{P}^n - \mathbf{P}^{n-1} + 2\tau\left[2f(\mathbf{P}^n) - f(\mathbf{P}^{n-1})\right]\right] \\ \mathbf{P}^0 &= g^0 \\ \mathbf{P}^1 &= g^1 \ , \end{aligned} \tag{6.3}$$

are usually employed for solving equations of this type. g_i^0 and g_i^1 are initial conditions. In these methods, time step is limited by space step as

$$\tau \lessapprox \Delta^2 \ . \tag{6.4}$$

This holds for computation in direct as well as in reciprocal space. Space constraint and the fact, that space grid must be chosen relatively dense to obtain profiles consistent with analytical solution, make Euler methods unusable for simulations of long time periods.

Implementation of an implicit method would eliminate this time-step constraint. Construction of such scheme would be, however, prohibitively difficult due to non-linear Landau part at the right-hand side of Landau-Khalatnikov equation.

Implementation of a semi-implicit scheme offers certain improvement. It was proposed for computations in Fourier space (Refs. [20, 32]) and allows for a considerable increase of the time step. It utilizes the fact that second derivative (present in gradient part of the free energy) is simple multiplication of Fourier image of order parameter by parabolic kernal. Right-hand side of Landau-Khalatnikov equation is therefore split into two parts - gradient force and the rest. First-order Euler scheme with substitution $n \rightarrow n+1$ to the gradient part can be schematically written

$$\mathbf{P}^{n+1}(\mathbf{k}) = \mathbf{P}^{n}(\mathbf{k}) + \tau \left[\tilde{f}(\mathbf{P}^{n}(\mathbf{k})) - k^2 \mathbf{P}^{n+1}(\mathbf{k}) \right] \ , \tag{6.5}$$

where $\tilde{f}$ does not include gradient force any more. This expression can be rewritten in the form

$$\mathbf{P}^{n+1}(\mathbf{k}) = \frac{1}{(1+\tau k^2)} \left[\mathbf{P}^{n}(\mathbf{k}) + \tau \left[\tilde{f}(\mathbf{P}^{n}(\mathbf{k})) \right] \right] \ . \tag{6.6}$$

Similarly, second and third order semi-implicit methods can be constructed

$$\mathbf{P}^{n+1}(\mathbf{k}) = \frac{1}{(3+2\tau k^2)} \left[4\mathbf{P}^{n}(\mathbf{k}) - \mathbf{P}^{n-1}(\mathbf{k}) + 2\tau \left[2\tilde{f}(\mathbf{P}^{n}(\mathbf{k})) - \tilde{f}(\mathbf{P}^{n-1}(\mathbf{k})) \right] \right] \tag{6.7}$$

$$\begin{aligned} \mathbf{P}^0 &= g^0 \\ \mathbf{P}^1 &= g^1 \ , \end{aligned}$$

$$\mathbf{P}^{n+1}(\mathbf{k}) = \frac{18\mathbf{P}^{n}(\mathbf{k}) - 9\mathbf{P}^{n-1}(\mathbf{k}) + 2\mathbf{P}^{n-2}(\mathbf{k}) + 6\tau \left[3\tilde{f}(\mathbf{P}^{n}(\mathbf{k})) - 3\tilde{f}(\mathbf{P}^{n-1}(\mathbf{k})) + \tilde{f}(\mathbf{P}^{n-2}(\mathbf{k})) \right]}{(11+6\tau k^2)} \tag{6.8}$$

$$\begin{aligned} \mathbf{P}^0 &= g^0 \\ \mathbf{P}^1 &= g^1 \\ \mathbf{P}^2 &= g^2 \ . \end{aligned}$$

Semi-implicit time-step is still limited by grid spacing, but it can be now chosen considerably greater than in the case of the Euler algorithm. In the simulations, it is most beneficial to use semi-implicit method of the second or third order(Ref. [32]).

In three dimensions with anisotropic gradient part, the derivation of semi-implicit scheme is slightly more difficult. Suppose that X, Y, Z are number of grid points in individual directions and Δ is grid spacing. Equations of three-dimensional semi-implicit method with use of Kramer's rule reads

$$\begin{aligned} \mathbf{P}_i^{n+1} \ = \ & \sum_{j=0}^{3} S_{ij} \Big[18\mathbf{P}_j^{n}(\mathbf{k}) - 9\mathbf{P}_j^{n-1}(\mathbf{k}) + 2\mathbf{P}_j^{n-2}(\mathbf{k}) \\ & + 6\tau \left[3f_j(\mathbf{P}^{n}(\mathbf{k})) - 3f_j(\mathbf{P}^{n-1}(\mathbf{k})) + f_j(\mathbf{P}^{n-2}(\mathbf{k})) \right] \Big] \end{aligned} \tag{6.9}$$

where matrix **S** with components

$$\begin{aligned}
S_{11} &= \frac{1}{D}\left[-(6\tau)^2\frac{16\pi^4 G_{14}^2}{X^2Z^2\Delta^4}k_2^2k_3^2 + R_{22}R_{33}\right]\\
S_{22} &= \frac{1}{D}\left[-(6\tau)^2\frac{16\pi^4 G_{14}^2}{X^2Z^2\Delta^4}k_1^2k_3^2 + R_{11}R_{33}\right]\\
S_{33} &= \frac{1}{D}\left[-(6\tau)^2\frac{16\pi^4 G_{14}^2}{X^2Y^2\Delta^4}k_1^2k_2^2 + R_{11}R_{22}\right]\\
S_{23} &= \frac{1}{D}\left[6\tau k_2k_3\left(6\tau\frac{16\pi^4 G_{14}^2}{X^2YZ\Delta^4}k_1^2 - \frac{4\pi^2 G_{14}}{YZ\Delta^2}R_{11}\right)\right]\\
S_{13} &= \frac{1}{D}\left[6\tau k_1k_3\left(6\tau\frac{16\pi^4 G_{14}^2}{XY^2Z\Delta^4}k_2^2 - \frac{4\pi^2 G_{14}}{XZ\Delta^2}R_{22}\right)\right]\\
S_{12} &= \frac{1}{D}\left[6\tau k_1k_2\left(6\tau\frac{16\pi^4 G_{14}^2}{XYZ^2\Delta^4}k_3^2 - \frac{4\pi^2 G_{14}}{XY\Delta^2}R_{33}\right)\right]
\end{aligned} \tag{6.10}$$

is the inversion of the matrix **R** with determinant D and components

$$R_{11} = 11 + 6\tau\left[\frac{4\pi^2 G_{11}}{X^2\Delta^2}k_1^2 + \frac{4\pi^2 G_{44}}{X^2\Delta^2}\left(k_2^2+k_3^2\right)\right] \tag{6.11}$$

$$R_{22} = 11 + 6\tau\left[\frac{4\pi^2 G_{11}}{Y^2\Delta^2}k_2^2 + \frac{4\pi^2 G_{44}}{Y^2\Delta^2}\left(k_1^2+k_3^2\right)\right] \tag{6.12}$$

$$R_{33} = 11 + 6\tau\left[\frac{4\pi^2 G_{11}}{Z^2\Delta^2}k_3^2 + \frac{4\pi^2 G_{44}}{Z^2\Delta^2}\left(k_1^2+k_2^2\right)\right] \tag{6.13}$$

$$R_{23} = 6\tau\frac{4\pi^2 G_{14}}{YZ\Delta^2}k_2k_3 \tag{6.14}$$

$$R_{13} = 6\tau\frac{4\pi^2 G_{14}}{YZ\Delta^2}k_1k_3 \tag{6.15}$$

$$R_{12} = 6\tau\frac{4\pi^2 G_{14}}{YZ\Delta^2}k_1k_2, \tag{6.16}$$

Derivatives from the matrix (5.8) were replaced by discrete derivatives in reciprocal space (see Eqn. B.9).

Dipole-dipole interaction can be treated analogically to the gradient interaction in the Fourier space. The variation with respect to polarization can be expressed as product of Fourier image of polarization and a function dependent only on a direction from the origin of the Fourier space. Method can be thus improved.

6.2 Description of programs and their parameters

The evolution of polarization field was solved numerically with use of previously described methods. Simulations were performed for a bulk crystal of $BaTiO_3$ from given initial state with prescribed external electric field, external mechanical conditions (stress or strain) and temperature. Resulting sequence of polarization fields was represented graphically and additional information were extracted from polarization arrays.

In order to keep it simple, four independent programs were designed: program `ferrodo` for computation of polarization evolution, program `drawarray` for preparation of initial conditions, program `view` for displaying images and program `elast_draw` for displaying of elastic field. Special format `*.arr` is used for storage of polarization field (Sec. 6.2.6).

The code is written in C++ programming language with use of external libraries for special objectives. Fourier transform is computed with use of `FFTW` (Fastest Fourier Transform in the West) subroutine library for computation of the discrete Fourier transform [70]. The `cpgplot` variant of Fortran `pgplot` library [71] is used for plotting images. Finally, `getopt` library is used for processing of command-line parameters.

6.2.1 Program `ferrodo`

Program `ferrodo` is designed for computation of evolution of polarization field.

The program is compiled from several source and header files: `ferrodo.cpp` contains main loop of the program and computational routines, `parameters_ferrodo.cpp` is responsible for loading and preprocessing of parameters of the program. Finally, `output_ferrodo.cpp` contains mechanisms for output and saving of computed data. There is additional file `utility.cpp` that contains necessary input/output and complementary routines. All routines are declared in appropriate header files `ferrodo.h`, `parameters_ferrodo.h`, `output_ferrodo.h` and `utility.h`. Compiled program is launched by the command

```
ferrodo --iterations ITERATIONS --x X --y Y --z Z --pdim PDIM --dt DT
--dx DX --steady_temperature STEADY_TEMPERATURE --multlandau MULTLANDAU
--multgrad MULTGRAD --multelast MULTELAST --multel MULTEL --multdipdip
MULTDIPDIP --clamped CLAMPED --palette PALETTE --save_period SAVE_PERIOD
--printinfo_period PRINTINFO_PERIOD --record_period RECORD_PERIOD
--model_parameters_landau MODEL_PARAMETERS_LANDAU --model_parameters_grad
MODEL_PARAMETERS_GRAD --model_parameters_elast MODEL_PARAMETERS_ELAST
--model_parameters_dipdip MODEL_PARAMETERS_DIPDIP --numerical_method
NUMERICAL_METHOD --initial_condition_file INITIAL_CONDITION_FILE --info_filename
info_FILENAME --output_dirname OUTPUT_DIRNAME
```

with following meaning of individual parameters (in parentheses, there is appropriate range of values of a particular parameter):

`--x`	x-dimension of simulation area (integer$\in\{1,2,4,...,2^n,...\}$)
`--y`	y-dimension of simulation area (integer$\in\{1,2,4,...,2^n,...\}$)
`--z`	z-dimension of simulation area (integer$\in\{1,2,4,...,2^n,...\}$)

`--iterations`	Number of iterations in the main loop of the program (integer∈{1,...})
`--pdim`	Dimension of polarization vector (integer∈{1..3}]). For `PDIM=1` is the polarization aligned alon x-direction, for `PDIM=2` it is restricted to xy plane
`--dt`	Value of time step τ (floating point number greater than zero. It must be chosen according to the value of parameter `--dx` in order to give stable scheme)
`--dx`	Grid spacing Δ (floating point number greater than zero)
`--steady_temperature`	Temperature of simulation (floating point number greater than zero)
`--multlandau`	Multiplicative coefficient to Landau generalized force (floating point number, no restriction on value)
`--multgrad`	Multiplicative coefficient to gradient generalized force (floating point number, no restriction on value)
`--multelast`	Multiplicative coefficient to elastostriction generalized force (floating point number, no restriction on value)
`--multel`	Multiplicative coefficient to generalized force from external electric field (floating point number, no restriction on value)
`--multdipdip`	Multiplicative coefficient to electrostatic dipole-dipole generalized force (floating point number, no restriction on value)
`--clamped`	Mechanical boundary conditions (integer: 0: Mechanically free sample in all directions 1: Mechanically clamped sample)
`--palette`	Number of palettes for output as in program `view` (integer∈{0,1,2,3})

`--save_period`	Number of iterations between saving images of polarization field (integer∈{1,...})
`--printinfo_period`	Number of iterations between printing information about status of the program (integer∈{1,...})
`--record_period`	Number of iterations between saving values of tracked physical quantities (integer∈{1,...})
`--model_parameters_landau`	Specification of Landau parameters: (integer: 0: Parameters according to [12] 1: parameters according to [13])
`--model_parameters_grad`	Specification of gradient constants: (integer: 0: According Tab. 2.1A 1: According Tab. 2.1C 2: $G_{11} = 1$, $G_{14} = 0$ and $G_{44} = 1$)
`--model_parameters_elast`	Specification of elastic and electrostriction constants (just integer=0 available corresponding to Tab. 2.1A)
`--model_parameters_dipdip`	Specification of background permittivity (just integer=0 available corresponding to Tab. 2.1A)
`--numerical_method`	Selection from available numerical schemes (integer: 0: First-order Euler 1: Second-order Euler scheme 2: Third-order Euler scheme 3: Semi-implicit third-order scheme)
`--initial_condition_file`	Name of file with initial conditions (string with full path to the `*.arr` file)
`--info_filename`	Name of html file for recording of input parameters of the program (string with full name of the `*.html` file)
`--output_dirname`	Name of temporary directory for output (string with full path)

Parameters are selected in order to answer basic expected usage of the program. It is, however, obvious that given command-line parameters do not cover the whole area of functionality of `ferrodo`. For example it is possible to consider more complicated dependence of temperature, external electric field or mechanical boundary conditions on time, as shown in simulations in following chapter. The program was also used to produce sequences of simulations e.g. when frequency dependence of dielectric constant was simulated. These properties of the program are accessible directly by changes in the source code, which is carefully commented in order to enable alterations according to actual needs.

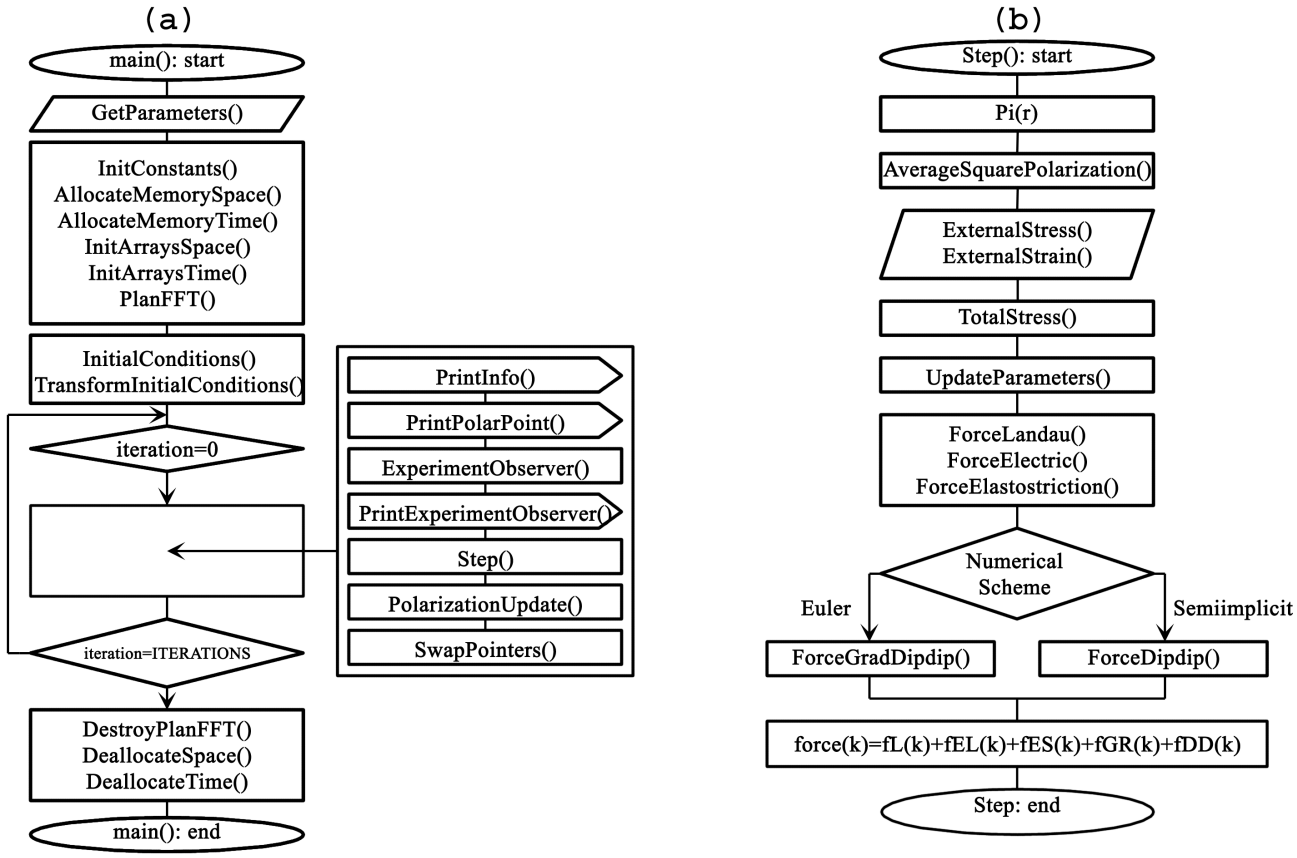

Figure 6.1: (a) Block diagram of the core cycle of the program `ferrodo`. Parentheses indicate names of subroutines, but parameters are not specified explicitly. (b) Routine `Step()` for computation of generalized forces.

Program implicitly runs in three-dimensional space. It may be, however, advantageous to decrease dimensionality of the space. It can be accomplished by setting appropriate value of `Y`, `Y` or `Z` to 1. It effectively results in decreasing of dimension of the problem in that direction so that the space is two-dimensional. One dimensional space is obtained by setting two of `X`, `Y`, `Z` to 1.

The program is initiated from linux shell script with one command line parameter: the name of output directory. The directory is created and the program is launched with all command-line parameters specified in the script. When the program `ferrodo` is finished, the script continues by copying important files from temporary to the output directory.

Basic scheme of the program is indicated in two flow graphs: Fig. 6.1(a) depicts the main cycle of the program. Key component of the loop, the subroutine `step()`, is schematically described in Fig. 6.1(b).

Command line parameters are processed by `GetParameters()` with use of `getopt` library routines immediately after start of the program and the parameters of the GGLD model are obtained.

Allocation and initialization of appropriate structures follows. There are basically two types of data arrays: Those which depends on a number of iterations and those which depends on

a dimension of simulation area. Important representant of the first group is array for storing data tracked during simulation. Arrays in the second group are intended for storing of (two or more) polarization arrays and (one or more) arrays of generalized forces[1]. There are also arrays for elastostriction kernels. Both types of fields are allocated (`AllocateMemorySpace()`, `AllocateMemoryTime()`) and initialized (`InitArraySpace()`, `InitArrayTime()`) based on previously loaded parameters and constants from `InitArrayConstants()`.

Fourier transform is initialized in the subroutine `PlanFFT()`, which tests the fastest scheme for computation of the fast Fourier transform. This can take several minutes for large domains.

Initial polarization array is then loaded, and polarization field is transformed into reciprocal space (`InitialConditions()`, `TransformInitialConditions()`).

The program then repeats routines in the main loop. Firstly, information about simulation stage are written to standard output (screen) by routine `PrintInfo()`. They contains information about program progress in percents, estimated time, elapsed time, actual temperature, actual nonzero components of electric field, external stress and external strain. Polarization array is saved and displayed by `PrintPolarPoint()`. Tracked quantities are then computed by `ExperimentObserver()` routine and displayed by `PrintExperimentObserver()`. Generalized forces in Fourier space are computed in `Step()`, and actual polarization field is updated with use of selected numerical scheme in `PolarizationUpdate()`. Pointers that points to various data arrays are then rotated in order to prepare for the next cycle.

At the end of the program, all fields are de-allocated with use of routines `DestroyPlanFFT()`, `DeallocateSpace()` and `DeallocateTime()`.

Routine `Step()` that computes generalized force from individual contributions to the free energy is the core of the whole program and is described separately in Fig. 6.1(b). It starts by transformation of polarization field into direct space. It is necessary for computation of Landau force which is preformed in direct space (Sec. 5. External stress or strain is then obtained from boundary conditions by `ExternalStress()`, `ExternalStrain()`. Routine `TotalStress()` computes value of individual components of homogeneous stress in order to keep mechanical boundary conditions as discussed in Sec. 2.4. Parameters of GGLD model (e.g. coefficients of Landau potential) are then updated by `UpdateParameters()`. Generalized forces originating from Landau, Electric and Elastostriction force are computed by `ForceLandau()`, `ForceElectric()` and `ForceElastostriction()`, resp. Gradient and dipole-dipole electrostatic force is evaluated either in `ForceGradDipdip()` (if Euler numerical scheme is used) or in `ForceDipDip()` (in case of semi-implicit numerical scheme). At the end of the `Step()` routine, individual contributions to the generalized force are put together.

All simulations were performed on personal computer with 3GHz Pentium4 CPU and 1GB RAM memory. It was possible to perform simulations of polarization fields about $256 \times 256 \times 16$ with three-dimensional order parameter.

[1] Number of necessary field is dependent on chosen numerical scheme (see Sec. 6.1).

6.2.2 List of outputs of the program `ferrodo`

`graph_angles.png`	Only for `PDIM`=2: polarization vector is in plane and it is possible to make histogram of angles of polarization vectors in discrete points. Sequence of these histograms provide two-dimensional graph of dependence of polarization angles on time.
`graph_applied_stress.png`	Time-dependence of external stress applied to the sample. Nonzero for `CLAMPED`=1, zero otherwise.
`graph_elfield.png`	Dependence of external electric field on time.
`graph_external_strain.png`	Time-dependence of homogeneous deformation of the sample.
`graph_maximal_force.png`	Time-dependence maximal value of all components of Landau, gradient, elastostriction, dipole-dipole and total generalized force.
`graph_mean.png`	Time-dependence of mean value of polarization and square of polarization in the sample.
`graph_temperature.png`	Time-dependence of temperature of the sample.
`info.html`	Detail description of initial conditions. Exact explanation is provided for every parameter.
`p__0000000.arr`	Polarization – iteration 0: initial conditions.
`p__0000000v.gif`	Plot of polarization – iteration 0: initial conditions.
`p__0000100.arr`	Polarization – iteration 100.
`p__0000100v.gif`	Plot of polarization – iteration 100.
`p__0000200.arr`	Polarization – iteration 200.
`p__0000200v.gif`	Plot of polarization – iteration 200.
...	

`record_angles.arr`	Data for plot `graph_angles.png`
`record_all.arr`	Record of tracked quantities. Data tracked by the program are: Maximal values of Landau, gradient, elastostriction, dipole-dipole and electric force across the whole simulation area, mean value of polarization, mean value of square of polarization, temperature, external stress, boundary stress, external strain and external electric field.

6.2.3 Program `drawarray`

Program `drawarray` is designed for preparation of initial polarization fields. It contains wide variety of routines designed to produce particular polarization field. It is necessary to combine routines manually, recompile and run the program in order to obtain desired polarization array. Result is saved in a file with a name constructed as `(DIM)d(PDIM)d__(X)[_(Y)][_(Z)]__array.arr`. Bracketed values are changed for appropriate numerical values of parameters with the same meaning as that defined in Sec. 6.2.1. Polarization array is also displayed with use of the `view` program. Quantities in parenthesis stand for integer numbers, dimensions brackets are optionally used according to value`DIM`. The program is launched by the command

```
drawarray [-output_file FILE1]
```

with one optional parameter for name of output `*.gif` file.

6.2.4 Program `view`

Program `view` displays polarization array and save it to the `*.gif` graphical file. Several command-line parameters can alter the functionality of the program. It is launched by the command:

```
view -input_file FILE1 [-output_file FILE2] [-blackwhite] [-arrow] [--palette
NPALETTE]
```

Individual parameters have meaning:

`--input_file`	Name of `*.arr` file with polarization field
`[--output_file]`	Optional name of output `*.gif` file (if omitted, the name is constructed from input name as `FILE1v.gif`)
`[--blackwhite]`	Gray-scale output, feasible e.g. for publication in journals
`[--arrow]`	Draw arrows (only for two-dimensional polarization arrays)
`[--palette]`	Specification of color palette (see Fig. 6.2): 0 Combined palette 1 Tetragonal palette 2 Orthorombic palette 3 Rhombohedral palette

Graphical schemes used for decoration of ferroelectric domain structure is apparent from Fig. 6.2.

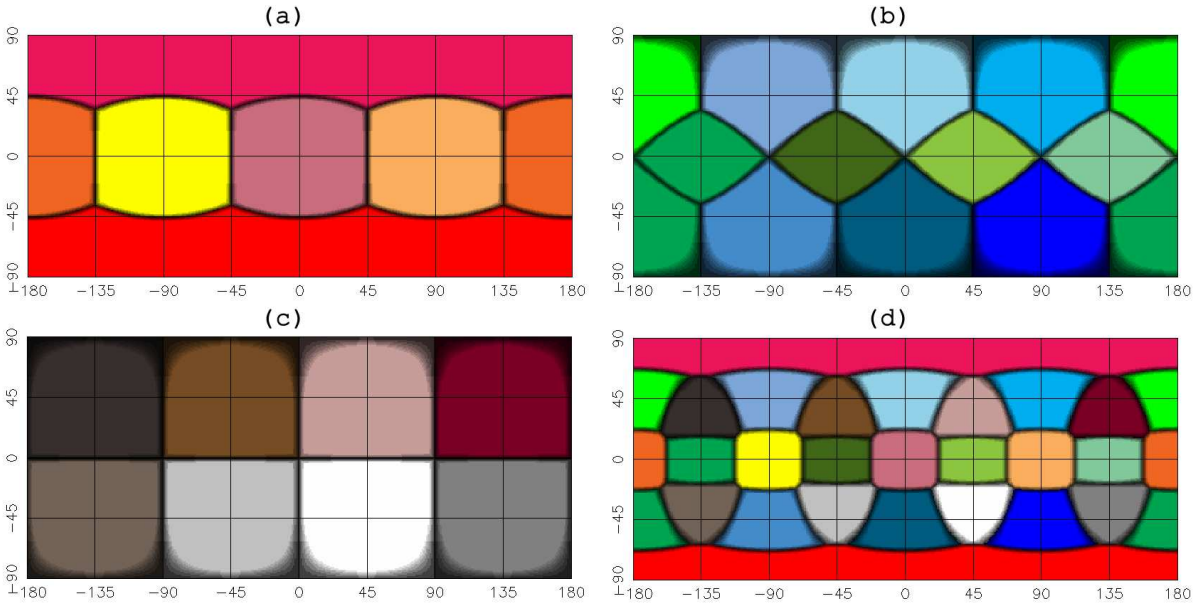

Figure 6.2: Color palettes used for display of different directions of order parameter. (a) tetragonal phase, (b) orthorombic phase, (c) rhombohedral phase, (d) all schemes mixed together. Horizontal axis represents angle in the canvas xy plane, while vertical represents angle of a polarization vector from the canvas.

A color is assigned to every particular direction of spontaneous polarization. Similar direction of polarization have the same color. The color does not depend on the magnitude of the vector. If a direction of polarization is approximately in between two spontaneous values, its color is shaded indicating smooth change from one state to another. For all ferroelectric phases of $BaTiO_3$ a specific color scheme is designed and used. Red, orange and yellow for tetragonal

phase, blue and green for orthorombic phase and brown and grey for rhombohedral phase.

Appropriate color scheme corresponding to the temperature of simulation is used. It is also possible to combine individual schemes when the temperature changes during a simulation and pass through a transition temperature, or if one is interested in phase coexistence at certain temperature. All schemes for individual phases are displayed in Fig. 6.2(a-c), mixed in Fig. 6.2(d).

In the presented scheme any spontaneous direction is unambiguously determined by its color. Color corresponding do the direction of polarization is drawn for every single point individually. Projection of polarization to the plane of an image is also optionally indicated by arrows. These are usually drawn only for selected points, in this work for 32×32 grid. Arrow does not reflect polarization in neighboring points, it simply stands for value of polarization in which it is plotted. In the case of rhombohedral phase, where vector of spontaneous polarization is declined either up or down with respect to canvas plane, white and black color of arrow is used for up and down deviation, resp.

Axis orientation for two-dimensional and three-dimensional plots of polarization fields is given in Fig. 6.3 (a) and (b), resp.

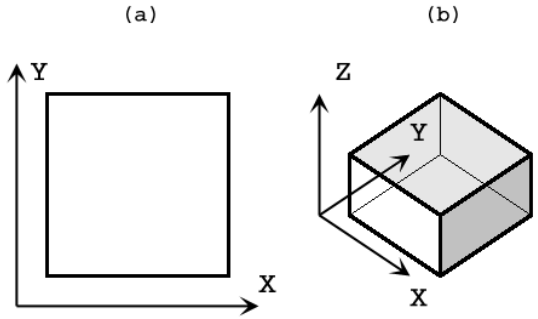

Figure 6.3: Axis orientation in two- and three-dimensional plots.

6.2.5 Program `elast_draw`

The program is designed to compute and display field of elastic displacements and field of components of the strain tensor.

It is launched by the command:

```
elast_draw -input_file FILE1 -x DX
```

File FILE1 must be a file of the type `*.arr` with two-dimensional polarization array. DX is grid spacing. The program then produces following outputs:

`strain_xx.gif`	$e_{11}(\mathbf{x})$ com
`strain_yy.gif`	$e_{22}(\mathbf{x})$ com
`strain_xy.gif`	$e_{12}(\mathbf{x})$ com
`displacement.gif`	Array of e angular gr

6.2.6 Storing of polarization field

Polarization field is stored in files with suffix `*.arr` with purposely designed structure. First line defines dimension of stored field

`#(DIM) X [Y ][Z ](PDIM)`

where `DIM` (standing for dimension of the simulation domain) ranges from 1 to 3. Values in brackets are used according to the value of `DIM`: if `DIM=1`, `DIM=2` or `DIM=3` then X, X and Y, or X, Y and Z must be specified.

After the first header line, there follow sequences of blocks separated by blank lines. Each block represents data for xy plane with increasing z-coordinate. Inside each block, lines corresponds to increasing x-coordinate and each line consists of a sequence of vectors (with dimension PDIM) with increasing y-coordinate:

```
#(DIM)    X    [Y    ][Z    ](PDIM)
P1(1,1,1) P2(1,1,1) P3(1,1,1)         ...  P1(1,Y,1) P2(1,Y,1) P3(1,Y,1)
                ...                   ...              ...
P1(X,1,1) P2(X,1,1) P3(X,1,1)         ...  P1(X,Y,1) P2(X,Y,1) P3(X,Y,1)

P1(1,1,2) P2(1,1,2) P3(1,1,2)         ...  P1(1,Y,2) P2(1,Y,2) P3(1,Y,2)
                ...                   ...              ...
P1(X,1,2) P2(X,1,2) P3(X,1,2)         ...  P1(X,Y,2) P2(X,Y,2) P3(X,Y,2)

                ...                   ...              ...
                ...                   ...              ...

P1(1,1,Z) P2(1,1,Z) P3(1,1,Z)         ...  P1(1,Y,Z) P2(1,Y,Z) P3(1,Y,Z)
                ...                   ...              ...
P1(X,1,Z) P2(X,1,Z) P3(X,1,Z)         ...  P1(X,Y,Z) P2(X,Y,Z) P3(X,Y,Z)
```

6.3 Simulations in one and two dimensions

All simulations are performed in three-dimensional space. Some domain arrangements can, however, exhibit translational symmetry along one or two coordinate axes. In that case it is possible to lower the effective dimension of simulated area (as mentioned before) and consequently reduce computational demands. Consequence of such decrease of the dimension are discussed bellow.

Two-dimensional simulations simply represent three-dimensional material with no variation of the order parameter along third direction, say z-axis.

$$\frac{\partial P_i}{\partial z} = 0 \qquad \forall i \in \{1, 2, 3\} \tag{6.17}$$

Material must not have shear strain in z-component ($u_{23} = 0$, $u_{13} = 0$) in order o to fulfill periodic boundary conditions for elastic displacement. But $u_{33} \neq 0$ in general. Boundary conditions in z-direction (external stress or clamping) are prescribed separately even for two dimensional simulations. Fourier transform in the z-direction is trivial.

Simulations in one-dimensional space equivalent to three-dimensional simulation with

$$\begin{aligned} \frac{\partial P_i}{\partial y} &= 0 \qquad \forall i \in \{1,2,3\} \\ \frac{\partial P_i}{\partial z} &= 0 \qquad \forall i \in \{1,2,3\} \end{aligned} \tag{6.18}$$

and shear strains $u_{23} = 0$, $u_{13} = 0$ and $u_{12} = 0$. External strain or stress is again prescribed in all direction x, y and z separately. Fourier transform in y and z direction is trivial.

Dimension of order parameter is chosen independently on space dimensionality. Polarization can be thus restricted to the xy plane or just to x-component. It enables study of special cases like two dimensional ordering of polarization as in Fig. 1.1 or uniaxial ferroelectrics.

6.4 Possible domain walls in individual configurations

Various combinations of values of `DIM` and `PDIM` enables to simulate various sets of domain walls. For example for PDIM=2 it is not possible to simulate polarization in rhombohedral state.

Furthemore, possible domain walls are also limited by domain dimensions, which is power of two in order to simplify computation of the Fourier transform. Domain walls O60 or $O120_c$ have general direction and therefore their appearance will be either reduced or accompanied by bending and artificial rotation of the wall.

Possible domain walls for individual choice of `DIM` and `PDIM` are comprehensively listed in Tab. 6.1.

Table 6.1: Possible domain walls for various combinations of `DIM` and `PDIM` parameters.

DIM	PDIM	Possible walls	
2D	2D	Tetragonal:	T180{001},T90
		Orthorombic:	O180{1$\bar{1}$0},O180{001},O90
		Rhombohedral:	–
2D	3D	Tetragonal:	T180{001},T180{011},T90
		Orthorombic:	O180{1$\bar{1}$0},O180{001},O90,O120
		Rhombohedral:	R180{1$\bar{1}$0},R109,R71
3D	2D	Tetragonal:	T180{001},T180{011},T90
		Orthorombic:	O180{1$\bar{1}$0},O180{001},O90
		Rhombohedral:	–
3D	3D	All considered domain walls with the exception of O60 ($O120_c$) wall	

6.5 Advantages and disadvantages of simulation in Fourier space

Computation in Fourier space simplifies evaluation of long-range interactions. It is fast and enables to solve numerically Landau-Khalatnikov for large number of steps. It also exhibits excellent spatial convergence (Ref. [46]).

On the contrary, dimension of simulation domain must equal power of two. This can be restrictive for simulation of domain walls with special direction like S-wall in orthorombic $BaTiO_3$. Simulation in Fourier space also requires periodicity of boundary conditions. Model can not be easily accommodated for study of boundary effects. Another limitation comes from the fact that long-range kernels are defined for the whole sample. Therefore, it is impossible to simulate material that composes of several parts with different elastic and electrostriction (or electrical) properties.

Chapter 7

Examples of simulations

In this chapter, possible use of the program `ferrodo` is reviewed on several examples.

Presented simulations of domain structure formation are given together with complete information about parameter values. Individual plots of polarization field are also denoted by number of iterations from the start of the program. Real time in seconds is product of step and numerical value of τ/Λ (time-step divided by the kinetic coefficient from Landau-Khalatnikov equation). Parameters of the GGLD model were taken from parameter set "A" in Tab. 2.1, otherwise it is explicitly specified.

Initial conditions are chosen purposely in order to produce desired domain structure. Examples of initial polarization fields is given in Fig. 7.1. Random field of small polarization vectors with magnitude $0.01P_0$ is shown in Fig. 7.1(a). Remaining two pictures produce stripe structure with T90 and T180{001} domain walls (Fig. 7.1(b) and Fig. 7.1(c), resp.).

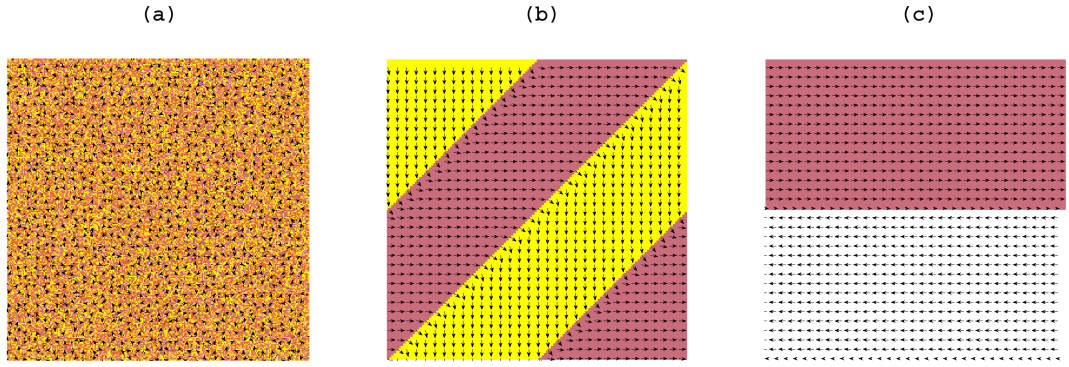

Figure 7.1: Initial polarization arrays used in simulations: (a) Random field representing quenched paraelectric cubic phase. (b) 90 degree charge-free tetragonal domain wall. (c) 180 degree charge-free tetragonal domain wall.

Time step used in simulations were tested with use of the double-step method. Testing simulation was performed twice: at first with chosen time-step (10000 steps) and then with time-step divided by two (20000 steps). Time step was accepted if the Euclidean norm of the difference of resulting polarization arrays fulfilled the condition

$$\frac{\sqrt{\sum_i^X \sum_j^Y \sum_k^Z \sum_d^3 [{}^1P_d(i,j,k) - {}^2P_d(i,j,k)]}}{P_0\sqrt{X \times Y \times Z}} \leq 0.001 \ , \tag{7.1}$$

where ${}^1\mathbf{P}$ and ${}^2\mathbf{P}$ is result of the first and second simulation, resp. This difference was considered for sufficiently small.

7.1 Space accuracy of numerically obtained profiles

Numerical approximation of an analytical profile was tested for 180 degree non-charged domain wall in dependence on the size of the spatial discretization step Δ.

At first, just Landau and gradient interaction were taken into account. We set $a_1 = -2.77 \times 10^7$, $a_{11} = -6.48 \times 10^8$, $a_{111} = 8.00 \times 10^9$ and $g = 51 \times 10^{11}$. Analytically computed profile have thickness $2\xi = 5.5$ nm. Numerical simulations were performed on one-dimensional space array with X=256 points and $\Delta \in \{1.0 \text{ nm}, \ 2.0 \text{ nm}, \ 3.0 \text{ nm}, \ 4.0 \text{ nm}\}$. Vector of polarization is in x-direction. Mechanically free sample relaxes from appropriate initial condition to the equilibrium state. Results are shown in the Fig. 7.2(a). There is almost no deviation from analytical profile for $\Delta = 1.0$ nm, $\Delta = 2.0$ nm and $\Delta = 3.0$ nm lattice spacing. In the case of $\Delta = 4.0$ nm, there is a significant discrepancy, but the derivative in the middle of the domain wall is still well reproduced.

Secondly, elastic and electrostriction interaction were added. Landau constants for this case were taken from Tab. 3.3 for T180{001} domain wall: $a_1 = -14.26 \times 10^7$, $a_{11} = 1.69 \times 10^8$, $a_{111} = 8.00 \times 10^9$. Gradient constant was again $g = 51 \times 10^{11}$. Domain wall thickness was computed to be 3.34 nm. It is slightly narrower than in the previous case. Therefore $\Delta = 0.5$ nm was added. Results of numerical simulations are displayed in Fig. 7.2(b). Again there is perfect agreement with theory up to $\Delta = 2.0$ nm. The results seems also reliable for lattice spacing 3.0 nm and 4.0 nm.

Previous results indicate that upper bound of the lattice spacing, which gives reliable results, is slightly lower than the half of the thickness of a domain wall. In order to give good predictions for finest structure that appears in the simulations (T180, O180{001}, O90, R109 and R71, which are all about 0.7 nm – see Tab. 3.3), we set grid spacing $\Delta = 0.4$ nm in cases when these walls are important.

7.2 Simulation of domain wall profiles

In Sec. 3, analytical computations of domain wall profiles and thickness were performed. Sufficient distance between domain walls can mimic infinite boundary conditions. Resulting profiles are expected to be the same as for analytical computations (Sec. 7.1). For narrower domains, the profile, thickness and the value of spontaneous polarization can different in comparison with analytical predictions.

Numerical simulations of T180{001} and T90 wall in tetragonal phase (at 298 K) with and without dipole-dipole interaction were performed. Coefficients of the model were taken from parameter set "A" in Tab. 2.1. Sample was mechanically free. Initial conditions (Fig. 7.1(c) and Fig. 7.1(b), resp.) produce stripe domain structure. The system relaxed towards equilibrium state. Resulting profiles are plotted in Fig. 7.3 and Fig. 7.4(a,b). Data were taken along the normal to the domain wall. In the insets, there is a schematic plot of a position of the discrete grid with respect to the domain wall and its normal. Numerical profiles were then fitted and a domain wall thickness was estimated from derivatives of fitting functions in the center of the domain wall. Estimates are summarized in Tab. 7.1.

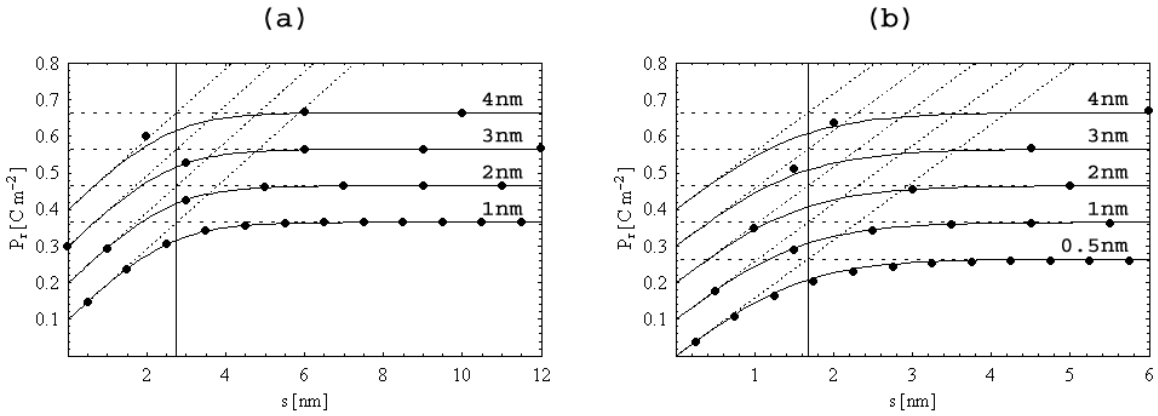

Figure 7.2: Analytically (solid line) and numerically obtained profiles of polarization through domain wall with various grid spacing. (a) Only Landau and gradient interactions are taken into account. (b) Landau, gradient, elastic and electrostriction interaction included. Domain wall thickness is indicated by vertical line. Profiles are shifted in vertical direction for better resolution.

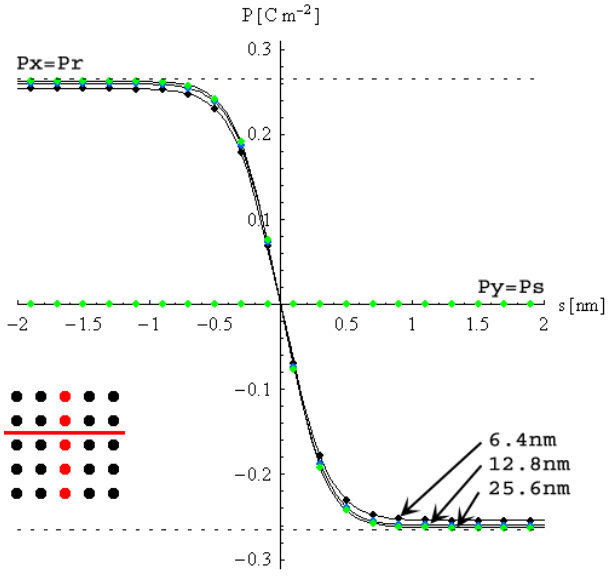

Figure 7.3: T180{001} domain wall in tetragonal $BaTiO_3$ for different distances between domain walls indicated by numbers next to arrows. Distance of walls is indicated by a number next to the profile. Discrete points together with the center of the domain wall (red line) are indicated in the inset.

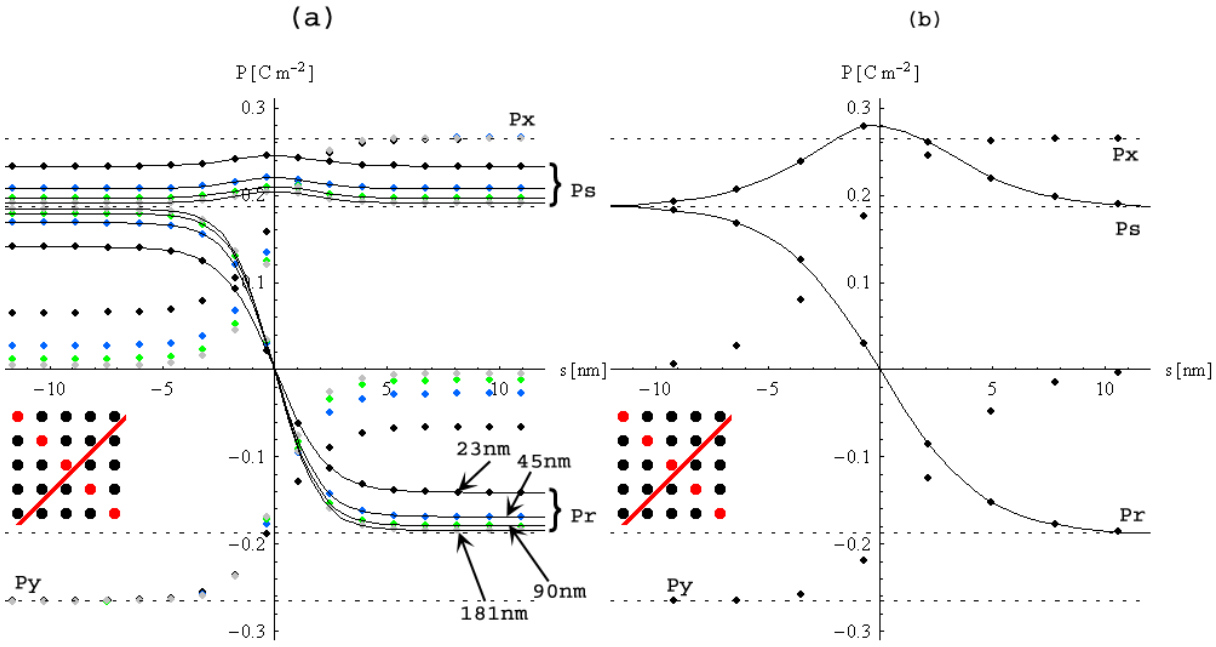

Figure 7.4: Simulation of profiles of T90 wall in tetragonal $BaTiO_3$: (a) Dipole-dipole interaction taken into account. Distances of individual walls are indicated by numbers next to arrows. (b) Without dipole-dipole interaction . Distances of walls the same as in (a), all profiles merge. Discrete points together with the center of the domain wall (red line) are indicated in the inset. P_x, P_y, P_r and P_s components of polarization field are plotted.

Table 7.1: Thicknesses of domain walls extracted from simulations of domain profiles in dependence on the distance of domain walls.

Domain wall		T180{001}			T90 (with F_{dep})				T90 (without F_{dep})
Walls distance	(nm)	6.4	12.8	25.6	23.0	45.0	90.0	181.0	23.0, 45.0, 90.0, 181.0
Thickness	(nm)	0.75	0.71	0.68	6.09	4.52	4.12	3.96	9.23

With increasing distance of walls the thickness approaches the value obtained analytically (0.63 nm for T180{001}, 3.59 nm for T90 with electrostatic interaction and 9.18 nm for T90 without electrostatic contribution). Small discrepancy (about 0.3 nm) for T90 with dipole-dipole interaction clearly originates from small hump in P_s component of polarization which is suppressed in analytical computations by setting P_s constant. Profiles of T90 walls without dipole-dipole interaction are identical irrespective on wall distance.

In the case of T90 wall with the distance of domain walls 22.6 nm, polarization in the middle of domains differs considerably from spontaneous value. It is inclined towards the direction of the wall normal.

Additional simulations confirmed that 90 degree domain structure in stress-free sample extinct for approximately 18 nm distance of walls. It, however, persist for clamped sample in simulations. Such domain structure is also clearly visible in grain in Fig. 1.2(a), thus emphasizing the crucial importance of external clamping and stresses.

7.3 Evolution from noise

7.3.1 Tetragonal phase

Several simulations were performed in order to observe features of a structure of $BaTiO_3$ produced by the model at room temperature. Mechanically free and mechanically clamped sample were taken into account. Both simulations started from noise that represents quenched paraelectric phase (Fig. 7.1(a)). Simulation setup: mesh 2D, 256×256 discrete points, $\Delta = 0.4$ nm, polarization 2D in-plane, $\tau = 2{\times}10^{-10}$, 25000 steps, temperature 298 K. Sequences in Figs. 7.5(a,b) give a picture of temporal evolution of both systems.

In the early stages, the development of the polarization field is governed by gradient and Landau interaction (compare with Fig. 7.6(c)). Polarization fields apparently do not differ much for 500 steps. For 2500 steps, there already exist T180{001} and T90 domain walls in both cases. The difference is still negligible. In following stages, however, the evolution splits.

In stress-free sample (Fig. 7.5(a)), either vertical or horizontal orientation of polarization gradually start prevailing at the expense of the second orientation, which is suppressed. Resulting structure have just 180 degree domain walls. The sample is macroscopically expanded in the x-direction and contracted in y and z direction. Value of spontaneous polarization reaches the spontaneous value in the middle of every domain.

For clamped sample, the boundary conditions cause that the evolution tends to reach domain structure with the same volume of domains with vertical and horizontal orientation of polarization. Resulting structure reveals system of T90 and T180{001} walls. Polarization is

arranged along tetragonal axes, polarization domains are almost relaxed to tetragonal state. The sample have macroscopically dimensions of original cubic sample. This arrangement was observed experimentally [1], and was also indicated by analytical calculations where both T90 and T180{001} walls have approximately the same energy (see Fig. 3.9(a)). Elastically permissible T90 and T180{001} walls are oriented in {110} and {100}, as expected in Sec. 3. All 180 degree domain walls are charge-free and also an overwhelming majority of 90 degree walls is not charged. This is due to strong dipole-dipole electrostatic interaction. Resulting system which is given in Fig. 7.5(b) is not in the equilibrium and will further develop.

A size of ferroelastic domains can be influenced by dimensions of simulation area. Another computation with large sample was performed (Fig. 7.5(c)). Simulation setup: mesh 2D, 1024×1024 points, $\Delta = 1.0$ nm, polarization 2D in-plane, $\tau = 5 \times 10^{-10}$, 100000 steps, mechanically clamped sample, temperature 298 K. Four stripes of ferroelastic domains have properties similar to those described above. The system is apparently not in the equilibrium state but it still slowly develops.

In order to verify the influence of individual interactions to the resulting structure, the dipole-dipole interaction was excluded. Simulation setup: mesh 2D, 256×256 points, $\Delta = 0.4$ nm, polarization 2D in-plane, $\tau = 2 \times 10^{-10}$, mechanically clamped sample, temperature 298 K. Results are displayed in Fig. 7.6(b). Similar domain structure appears as if electrostatic interaction were taken into account. The difference is that approximately half of T90 domain walls are head-to-head or tail-to-tail, i.e. charged. Charged domain walls are indicated by black (head-to-head) and red (tail-to-tail) in Fig. 7.6(b) for 3000 steps. The evolution without electrostatic interaction seems to be slightly faster compared to simulation with complete model.

An additional simulation was performed with only Landau and gradient interaction taken into account. Simulation setup: mesh 2D, 256×256 points, $\Delta = 0.4$ nm, polarization 2D in-plane, $\tau = 2 \times 10^{-10}$, temperature 298 K. Mechanical boundary conditions are irrelevant since there is no link between polarization and unit cell shape without elastostriction interaction. Coefficients α_{11} and α_{12} are substituted instead of $\alpha_{11}^{(e)}$ and $\alpha_{12}^{(e)}$ in order to obtain correct values of spontaneous polarization. The energy of domain walls is now entirely dependent on gradient short-range interaction. It seems that {100} directions of walls prevail during the whole simulation. It is due to the smaller gradient constant in the direction of cubic axis than in diagonal directions (≈ 13.6 times smaller). Polarization domain with $(P_x > 0, P_y = 0, P_z = 0)$ is the larger. It will finally prevail and span the whole sample.

Arrays of generalized forces from the right-hand side of Eqn. 5.4 are plotted in Fig. 7.9 for resulting image of simulation in Fig. 7.5(b). Maximal values of plotted arrays are given in Tab. 7.2. The total force, which is the sum of acting forces, is nonzero and the system will continue its evolution towards equilibrium.

Three-dimensional simulations were also preformed in tetragonal phase.

7.3.2 Orthorombic phase

Similar simulation of domain structure evolution as for tetragonal phase was performed in orthorombic phase in order to track basic features of resulting structure. Simulation setup: mesh 2D, 256×256 points, $\Delta = 4 \times 10^{-10}$, polarization 2D in-plane, $\tau = 2 \times 10^{-10}$, mechanically free sample, temperature 218 K.

Sequence of images of polarization field is displayed in Fig. 7.11. From initial stages there is noticeable fast alignment in fine orthorombic domain structure which subsequently coarsens.

Table 7.2: Maximal values of plotted arrays of generalized forces in Fig. ??.

Field	Component	Maximal value	Unit [SI]
f_{L}	x	36.87	$10^6\ \mathrm{kg\,m\,s^{-2}\,C^{-1}}$
f_{L}	y	33.38	$10^6\ \mathrm{kg\,m\,s^{-2}\,C^{-1}}$
f_{G}	x	3.92	$10^6\ \mathrm{kg\,m\,s^{-2}\,C^{-1}}$
f_{G}	y	3.92	$10^6\ \mathrm{kg\,m\,s^{-2}\,C^{-1}}$
f_{ES}	x	33.02	$10^6\ \mathrm{kg\,m\,s^{-2}\,C^{-1}}$
f_{ES}	y	33.02	$10^6\ \mathrm{kg\,m\,s^{-2}\,C^{-1}}$
f_{DD}	x	13.02	$10^6\ \mathrm{kg\,m\,s^{-2}\,C^{-1}}$
f_{DD}	y	13.02	$10^6\ \mathrm{kg\,m\,s^{-2}\,C^{-1}}$
f_{TO}	x	20.51	$10^6\ \mathrm{kg\,m\,s^{-2}\,C^{-1}}$
f_{TO}	y	18.11	$10^6\ \mathrm{kg\,m\,s^{-2}\,C^{-1}}$

There appears almost exclusively O90 domain walls which have, according to analytical computations, which is energetically far less expensive than O180$\{1\bar{1}0\}$.

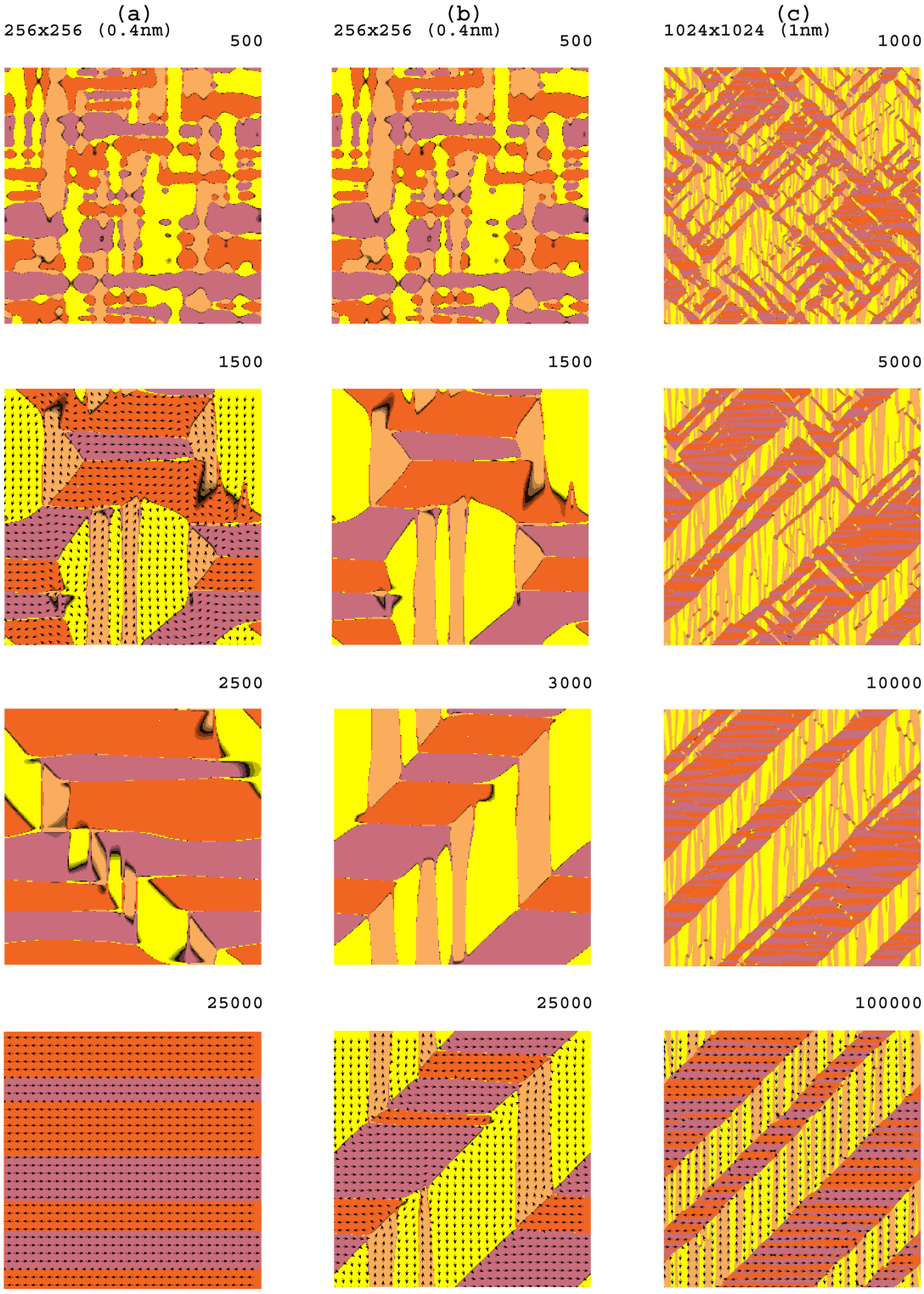

Figure 7.5: Simulation of tetragonal structure evolution from paraelectric state at 298 K. (a) Mechanically free sample with zero external stresses, 256x256 discrete points, (b) Mechanically clamped sample 256x256 discrete points, (c) Mechanically clamped sample, 1024x1024 points.

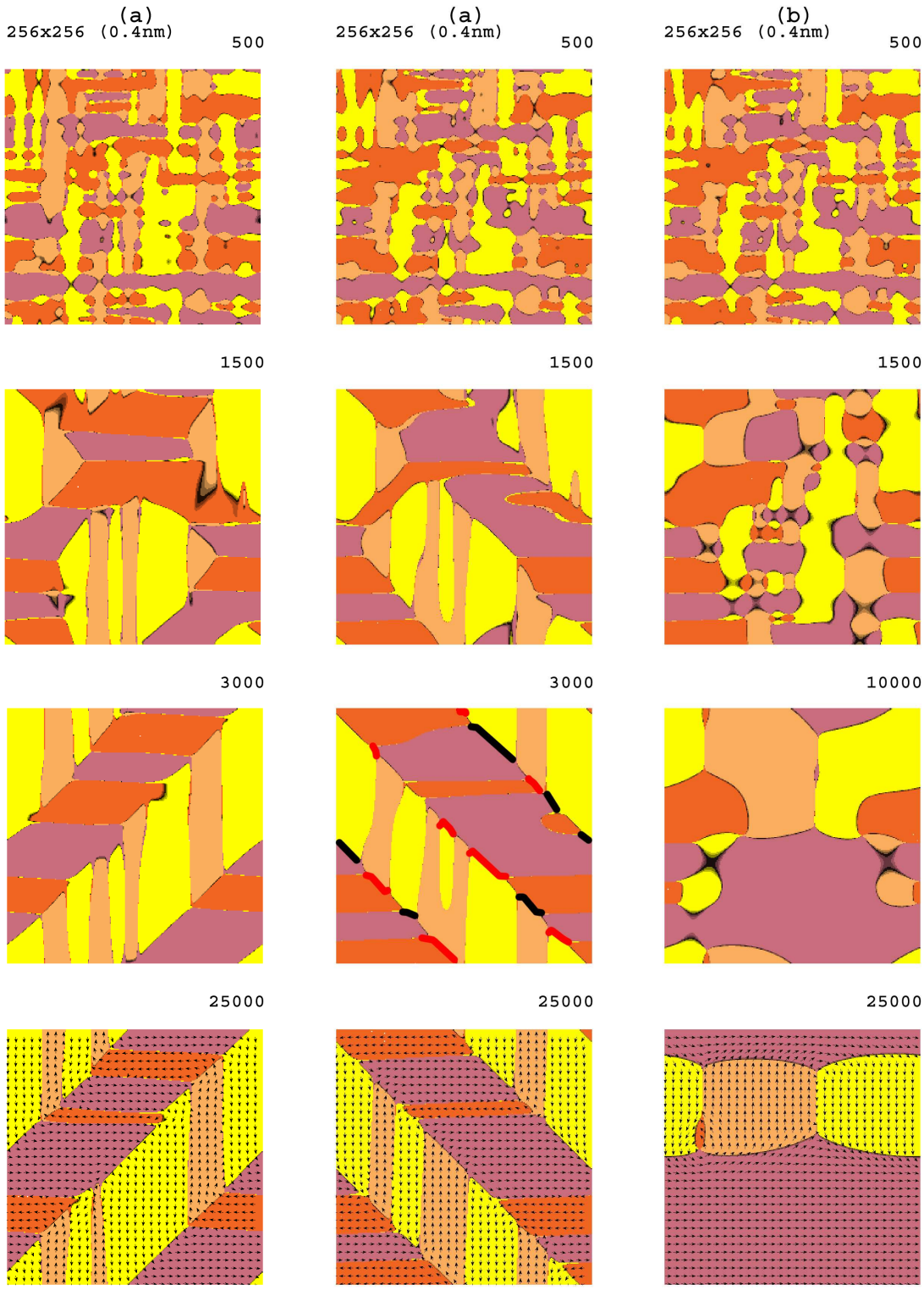

Figure 7.6: Simulation of tetragonal structure evolution from paraelectric state at 298 K. (a) All interactions taken into account, the figure is the same as in Fig. 7.5(b). (b) All but electrostatic interaction taken into account. Charged head-to-head and tail-to-tail walls are present (indicated by black and red curves in the picture for 3000 steps). (c) Only Landau and Gradient interaction taken into account.

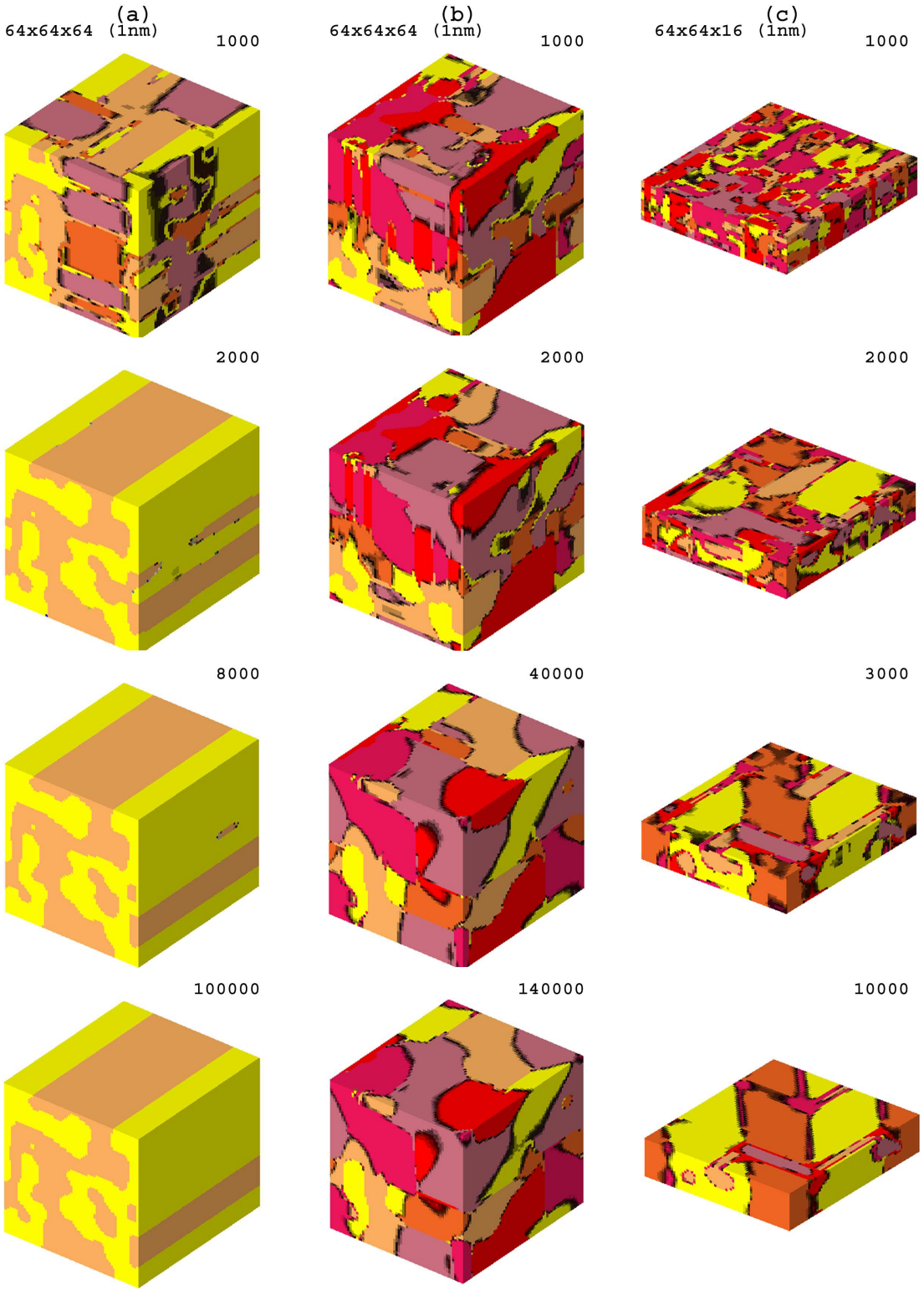

Figure 7.7: Simulations in three-dimensional domain with three-dimensional order parameter: (a) Mechanically free sample. (b) Mechanically clamped sample. (c) Mechanically clamped sample. Arrows indicate the direction of polarization.

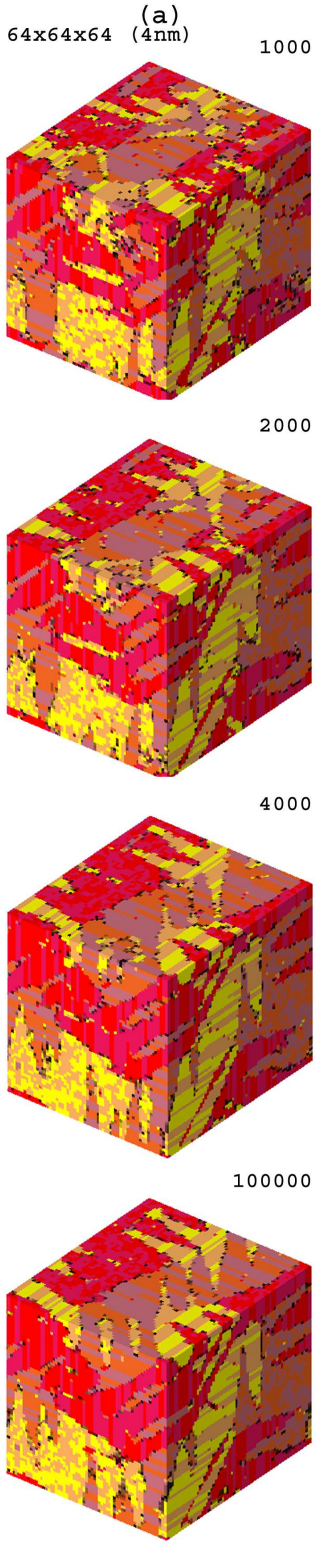

Figure 7.8: Simulations in three-dimensional domain with three-dimensional order parameter: (a) Mechanically free sample.

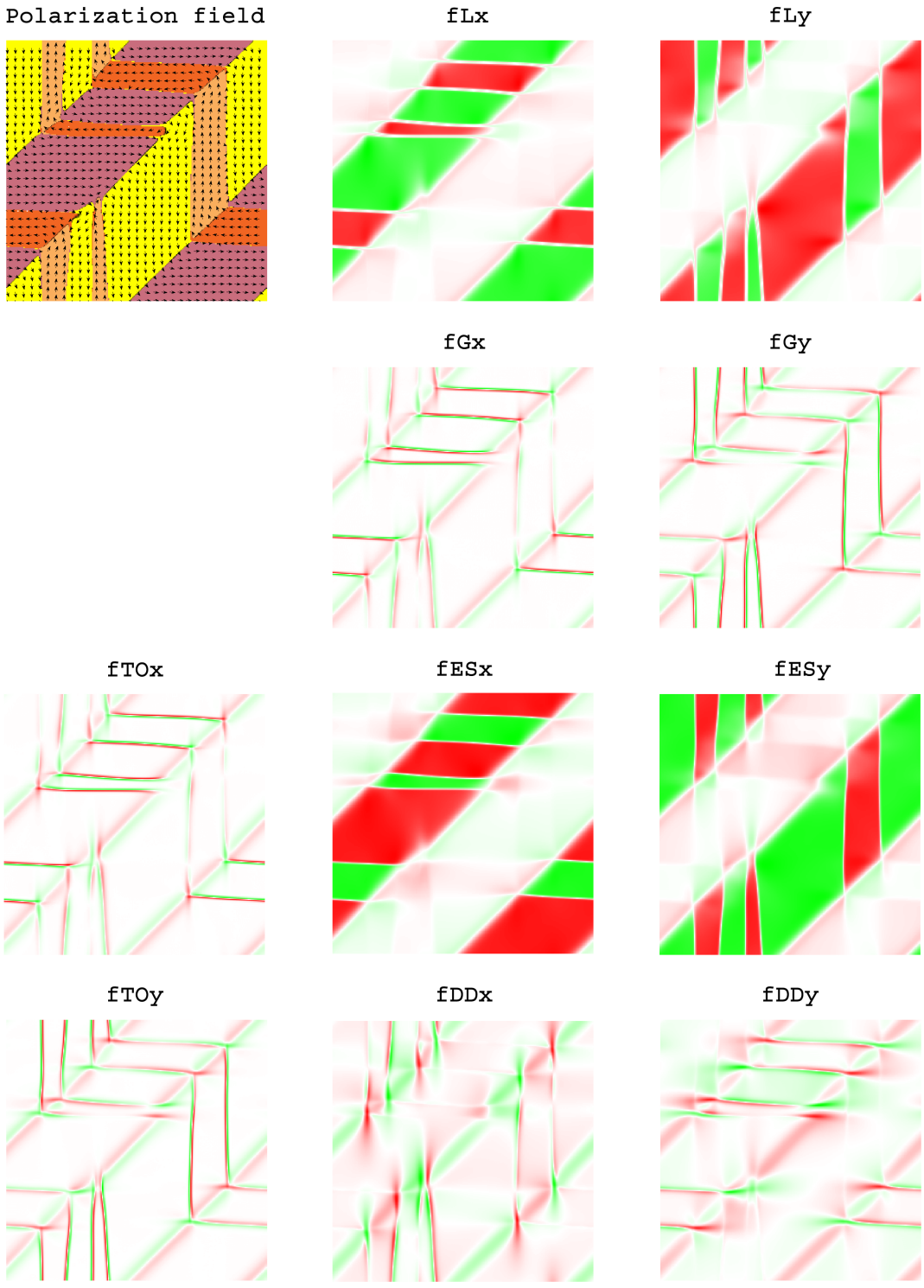

Figure 7.9: The same two-dimensional simulation as in Fig. 7.5(b). Final state of polarization field, local electric field, local elastic displacements and individual components of generalized forces acting in the sample are plotted.

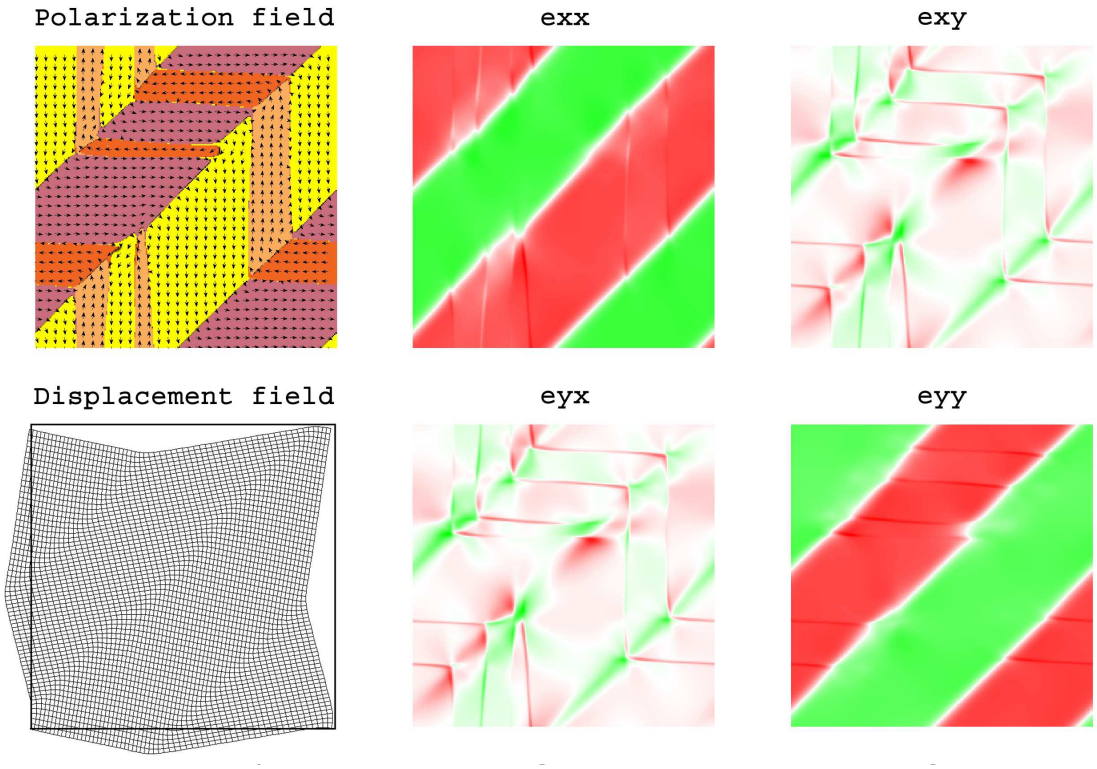

Figure 7.10: Output of the program `elast_draw`. Polarization field was loaded as input file. Bellow is schematic plot of elastic deformation of crystal grid. Finally, on the right-hand side of the image, there are spatially dependent components of elastic strain tensor. Color scheme used is the same as in Fig. 7.9. Maximal values follows. e_{11}: 5.41×10^{-3}, e_{12}: 1.19×10^{-3} and e_{22}: 5.75×10^{-3}

Figure 7.11: Simulation of evolution of polarization field from paraelectric state. (a) Orthorombic phase at temperature 208 K. (b) Rhombohedral phase at 118 K.

7.4 Switching from tetragonal to orthorombic state

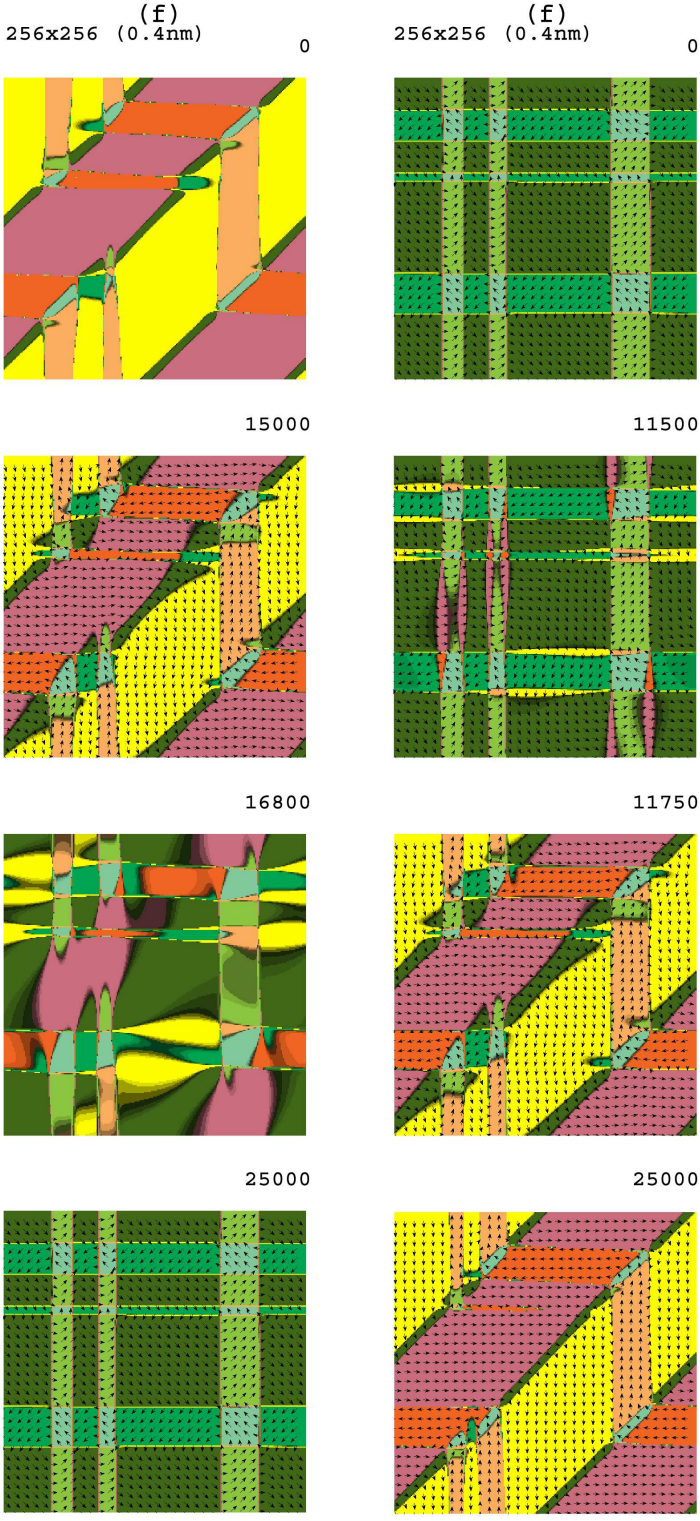

Figure 7.12: Simulations of phase transition between tetragonal and orthorombic state for mechanically clamped sample. (a) Temperature changes linearly 298 K $\rightarrow$ 208 K. (b) Temperature changes linearly 208 K $\rightarrow$ 298 K.

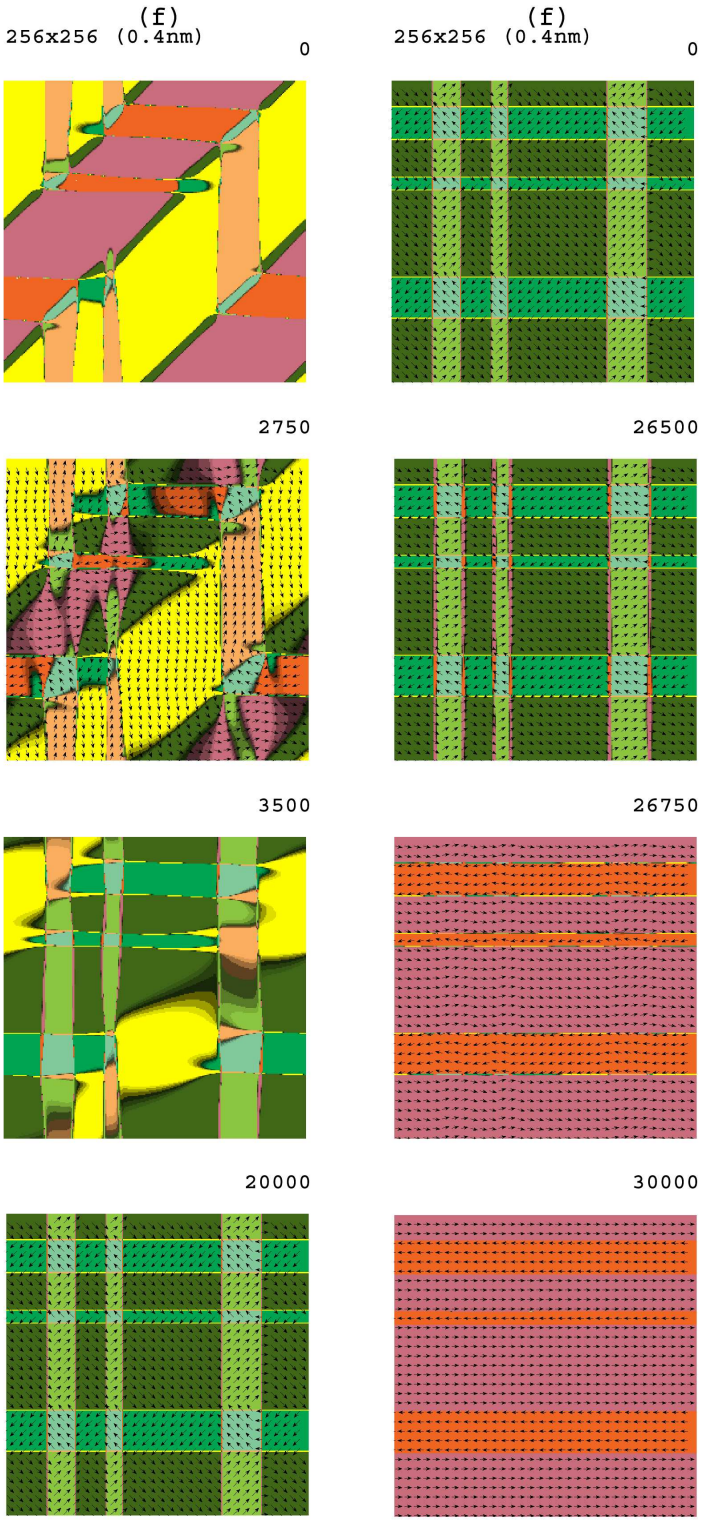

Figure 7.13: Simulations of phase transition between tetragonal and orthorombic state for mechanically stress-free sample. (a) Temperature changes linearly 298 K → 208 K. (b) Temperature changes linearly 208 K → 316 K.

7.5 Comparison with other authors

We compare our results with those published by S. Nambu and D.A. Sagala [18] and H.-L. Hu and L.-Q. Chen [19, 20].

7.5.1 Grid spacing and time step

The time step was chosen $\tau = 5. \times 10^{-10}$ for discrete grid spacing $\Delta = 1.0$ nm in our simulations. Taking into account renormalizations[1], S. Nambu and D.A. Sagala made computations with space step $\Delta = 0.8$ nm and time step $\tau = 6.73 \times 10^{-11}$. While grid spacing is comparable, time step is considerably lower as a consequence of used simple Euler algorithm. On the contrary, H.-L. Hu and L.-Q. Chen, who make use of the semi-implicit numerical scheme, have time their step twice larger as we have ($\tau = 13.50 \times 10^{-10}$). It corresponds to their larger grid spacing ($\Delta = 3.7$ nm).

Our time step is even lower $\tau = 2. \times 10^{-10}$ smaller grid spacing $\Delta = 0.4$ nm. This spacing is used for simulation of finest structures as discussed in Sec. 7.1.

7.5.2 Domain structure

Polarization fields with coexisting T90 and T180 domain walls were also compared. In our simulations in tetragonal phase, there appear T90 and T180$\{001\}$ wall structure as in the Fig. 7.5(b,c). Simulations published by S. Nambu and D.A. Sagala reveal fine T90 wall stripe structure. T180$\{001\}$ walls are, however, neither visible in the provided figures nor discussed. Therefore, it seems that there are no such walls. Slightly different situation is in Ref. [20], where domain walls are not visible in the images, but they are mentioned in the discussion. In the previous work (Ref. [19]) of the same authors, the 180 degree domain walls are again not visible, but their presence may be anticipated from T90 wall structure and the fact that the dipole-dipole interaction was taken into account in their computations. T180 walls are not mentioned in the discussion.

The reason for this sporadic appearance or non-existence of T180$\{001\}$ walls may be in different gradient constants or, more precisely, in resulting energies of domain walls. For given constants of Landau potential (a_1, a_2, a_3), the energy of domain wall in one-dimensional model is determined only by the value of gradient constant g, which is $g = G_{44}$ for T180$\{001\}$ wall and $g = (G_{11} - G_{12})/2$ for T90 wall. According to Eqn. 3.16, the energy of a wall depends on gradient constant as $\sqrt{g}$. We use values $G_{11} = 51$, $G_{12} = -2$ and $G_{44} = 2$, that result in $g_{T180} = 2$ and $g_{T90} = 26.5$. In all previously mentioned works, the gradient interaction was taken isotropic[2]: $G_{11} = 51$, $G_{12} = -51$ and $G_{44} = 51$. Consequently, $g_{T180} = 51$ and $g_{T90} = 51$.

From Tab. 3.3 and Fig. 3.9(b) it is apparent, that the wall energy per area Σ is approximately the same for T90 and T180$\{001\}$ (about 20% difference for room temperature). With coefficients compared articles, we get energy of T90 wall $\sqrt{2}$ higher, but energy of T180$\{001\}$ wall is approximately 5-times higher. It is clear that T180 walls are suppressed in those simulation.

---

[1] S. Nambu and D.A. Sagala using rescaling of variables $t' = (2\alpha_1\Lambda)\, t$, $\mathbf{x}' = \left(\frac{G_{11}}{2\alpha_1}\right)^{1/2} \mathbf{x}$ and $\mathbf{P}' = \frac{\mathbf{P}}{P_0}$. Similarly, H.-L. Hu and L.-Q. Chen using $t' = (\alpha_1\Lambda)\, t$, $\mathbf{x}' = \left(\frac{G_{11}}{\alpha_1}\right)^{1/2} \mathbf{x}$ and $\mathbf{P}' = \frac{\mathbf{P}}{P_0}$.

[2] Value of G_{11} is chosen the same as ours

7.6 Mobility of domain walls in tetragonal phase

Assuming that there is an appreciable contribution to the dielectric constant from motion of domain walls (i.e. polarization reversal at moving interface) at lower frequencies, it is important to know how fast can domain wall move under applied electric field. It is well known that T90 wall in $BaTiO_3$ is able to move relatively easily in comparison with T180 domain wall that almost does not move at room temperature.

Mobility μ_E of domain wall is defined as fraction $\mu_E = v/E_r$, where v is a velocity of domain wall and E_r is component of electric field in the direction of motion. In Ref. [44] it was reasoned that dissipated energy of wall motion equals

$$-\frac{1}{S}\frac{dF}{dt} = \frac{v^2}{\Lambda}\frac{2\Sigma}{G_{11}-G_{12}} \ . \tag{7.2}$$

Energy dissipation can be also expressed as energy decrease by polarization reversal due to applied electric field E_r

$$-\frac{1}{S}\frac{dF}{dt} = 2vP_{r\infty}E_r \ . \tag{7.3}$$

It was finally concluded that the mobility of T90 wall can be expressed as

$$\mu_E = \frac{v}{E_r} = \frac{\Lambda P_0(G_{11}-G_{12})}{\sqrt{2}\Sigma} \ . \tag{7.4}$$

For numerical values $(G_{11}-G_{12}) = 53\times10^{-11}$, $\Lambda = 4\times10^4$, $P_0 = 0.265$ and $\Sigma = 7\times10^{-3}$ (see Tabs. 2.1,3.3), the mobility is $\mu_E = 5.7\times10^{-4}\ \mathrm{m^2\,V^{-1}\,s^{-1}}$.

T90 domain wall is sufficiently large (with thickness about 10 crystal unit cells) smooth (see Sec. 3.3.3), and can be correctly described by continuous model. On the contrary, T180 degree domain wall with thickness less then 2 unit cells (see Sec. 3.3.1) is pinned to a discrete crystal lattice.

Time dependent GGLD model enables simulation of a domain wall motion. Simulations were performed for both T90 and T180{001} domain wall.

Velocity of a domain wall is determined by kinetic coefficient Λ in Landau-Khalatnikov equation[3], by Euler-Lagrange potential[4] and by discretization in numerical simulation. Rough grid enables to study bigger samples, but may create artificially energy barrier for motion of a domain wall. Dependence of wall motion on a spacing of the discrete grid is therefore also inspected for the case of T90 wall.

Model parameters were taken from set "A" in Tab. 2.1. Sample was mechanically free in all directions. For T90 wall, initial conditions were chosen as in Fig. 7.1(b), sufficiently aged in order provide equilibrium state at zero electric field. Three simulations was performed: 64x64 points for $\Delta = 2$ nm, 128x128 points for $\Delta = 1$ nm and 256x256 for $\Delta = 0.4$ nm. The distance of domain walls was 45 nm with the exception of 0.4 nm spacing where it was slightly lower, approximately 36 nm. We perform 10000 steps with τ accustomed to observe motion of the wall properly. Constant electric bias was applied in x-direction and ranges from $E_x = 2\times10^4\ \mathrm{V\,m^{-1}}$ up to $1.024\cdot10^7\ \mathrm{V\,m^{-1}}$.

[3] It was estimated as $\Lambda = 4\times10^4\ \ \mathrm{kg^{-1}\,m^{-3}\,s\,C^2}$.

[4] Euler-lagrange potential for particular structure as discussed in Sec. 3 that is changed e.g. by distance between domain walls, spontaneous values in adjacent domains with electric field, etc.

Domain wall position is (for purpose of this simulation) defined as zero point in linear interpolation of P_r (polarization component perpendicular to the wall) the between two following (in direction of the wall normal) discrete points $P_r^{(i)}$ and $P_r^{(i+1)}$ with opposite signs.

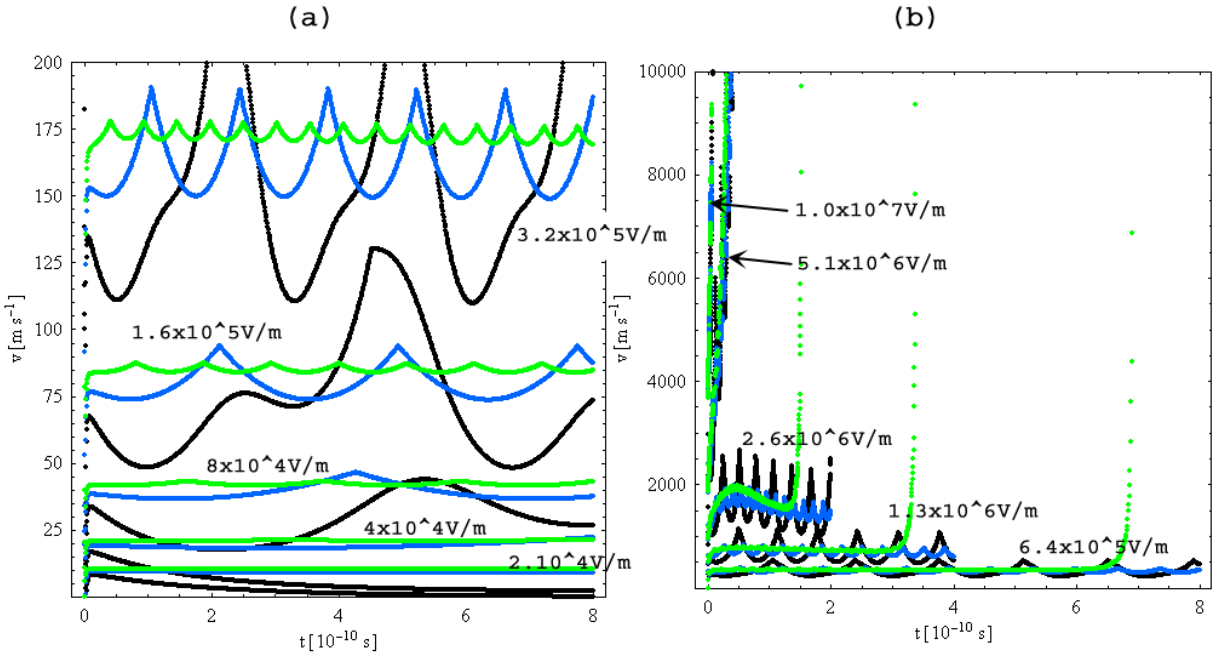

Figure 7.14: Time dependence of a velocity of T90 domain wall in tetragonal phase of $BaTiO_3$. Black: $\Delta = 2$ nm, blue: $\Delta = 1$ nm, green: $\Delta = 0.4$ nm. Values of electric field E_x are provided. (a) Lower values of applied bias, (b) higher values of applied bias.

Results are shown in Fig. 7.14. The simulation was started from initial conditions aged without external field. Therefore, after abrupt application of electric bias, there appear some residual effects in speed as the wall shifts in order to gain equilibrium position under new conditions. Then the velocity varies periodically[5] as grid points reach maximum in potential. For small electric fields (up to 1.28×10^6 V m^{-1}), the velocity remain constant in average, for higher the polarization switches in the whole volume and walls cease exist. It is indicated by extreme increase of wall speed.

For larger Δ, the time-dependence of the velocity is more irregular than for lower Δ. The average is, however, almost the same. It seems that domain the wall speed for $\Delta = 0.4$ nm spacing is systematically slightly higher than the speed for two remaining grid spacing. It is

[5]Speed of domain wall plotted versus time exhibits sharp peaks. Position of T90 domain wall in a system without electric field is not arbitrary, but it is pinned to a certain position with respect to the discrete lattice of a crystal which corresponds to the lowest potential energy. The analogy in numerical simulation is pinning with respect to discretization grid. Energy increase if the wall is displaced from this equilibrium position. The energy of the system vary periodically with the period of the grid. For the moment lets expect simple $sin(x)$ variation of energy with domain wall position. If sufficient electric field is applied, the energy increase is no longer periodic, but it is monotonically decreasing function of position, e.g. $F(x) = sin(x) - 1.2x$ (Fig. 7.15(a)). Velocity of a wall dependent on position may be obtained as derivative of energy with respect to position $v(x) = dF(x)/dx = -cos(x) + 1.2$ (Fig. 7.15(b)). Position dependence of the domain wall on time $s(t)$ can be evaluated from $ds(t)/dt = v(s(t))$ (Fig. 7.15(c)). Finally, required dependence of the wall speed on time reads $v(t) = v(s(t))$ (Fig. 7.15(d)). The shape of $v(t)$ exhibit similar peaks as in Fig. 7.14, exact shape would result from proper choice of $F(x)$.

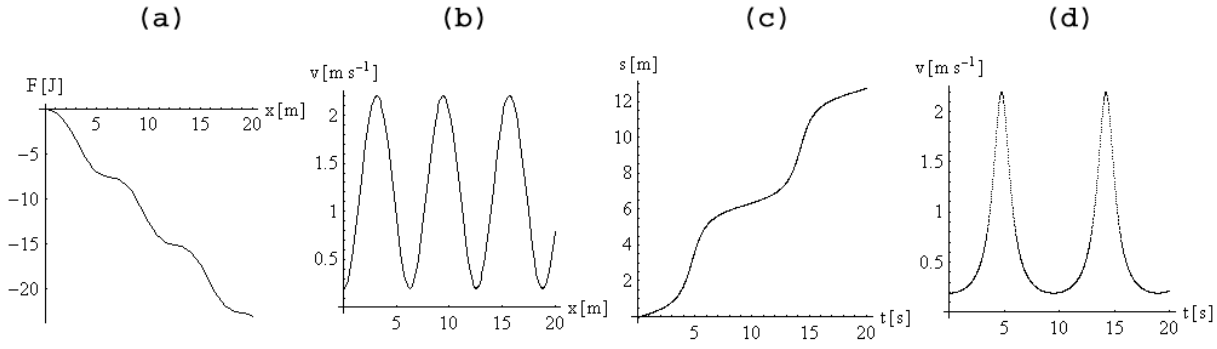

Figure 7.15: Explanation of sharp peaks in a domain wall speed versus time plot.

Table 7.3: Approximate mobility of T90 domain wall in tetragonal $BaTiO_3$ for grid spacing $\Delta = 0.4$ nm.

$E_r\,[10^4\ \mathrm{Vm^{-1}}]$	2	4	8	16	32	64	128	256
$E_x\,[10^4\ \mathrm{Vm^{-1}}]$	1.4	2.8	5.7	11.3	22.6	45.2	90.5	181.0
$\mu_E\,[10^{-4}\ \mathrm{m^2\,V^{-1}\,s^{-1}}]$	7.1	7.4	7.6	7.7	7.7	7.8	8.8	9.7

likely due to smoother shape that decreases energy barrier for domain wall to overcome. Effect of closer domain walls can be also partially responsible.

Values of estimated mobility of T90 domain wall are listed in Tab. 7.3 together with component of electric field normal to domain wall E_r. Resulting mobility is higher than that estimated in Eqn. 7.4. This discrepancy (about 25%) exhibits evident tendency to decrease for lower fields.

Similar simulation was performed for T180{001} domain wall with grid spacing $\Delta = 0.4$ nm. For larger values of Δ, the speed was either zero or to high to be tracked properly. The same setup as in previous case was used. Electric field E_x now ranges from $E_x = 32 \times 10^4\ \mathrm{V\,m^{-1}}$ to $E_x = 4.1 \times 10^7\ \mathrm{V\,m^{-1}}$. Domain wall velocity as well as the distance of the wall from its original position is displayed in Fig. 7.16. From comparison with Fig. 7.14 it is clear that mobility of T90 wall is lower than that of T90 wall. The mobility of T180{001} domain wall for increasing electric field E_x is estimated in Tab. 7.4.

Table 7.4: Approximate mobility of T180{001} wall in tetragonal $BaTiO_3$ for grid spacing 4 nm.

$E_x\,[10^4\ \mathrm{V\,m^{-1}}]$	32.0	64.0	128.0	256.0	512.0	1024.0	2048.0	4096.0
$\mu_E\,[10^{-4}\ \mathrm{m^2\,V^{-1}\,s^{-1}}]$	0.00	0.8	0.8	0.8	0.8	0.8	0.9	

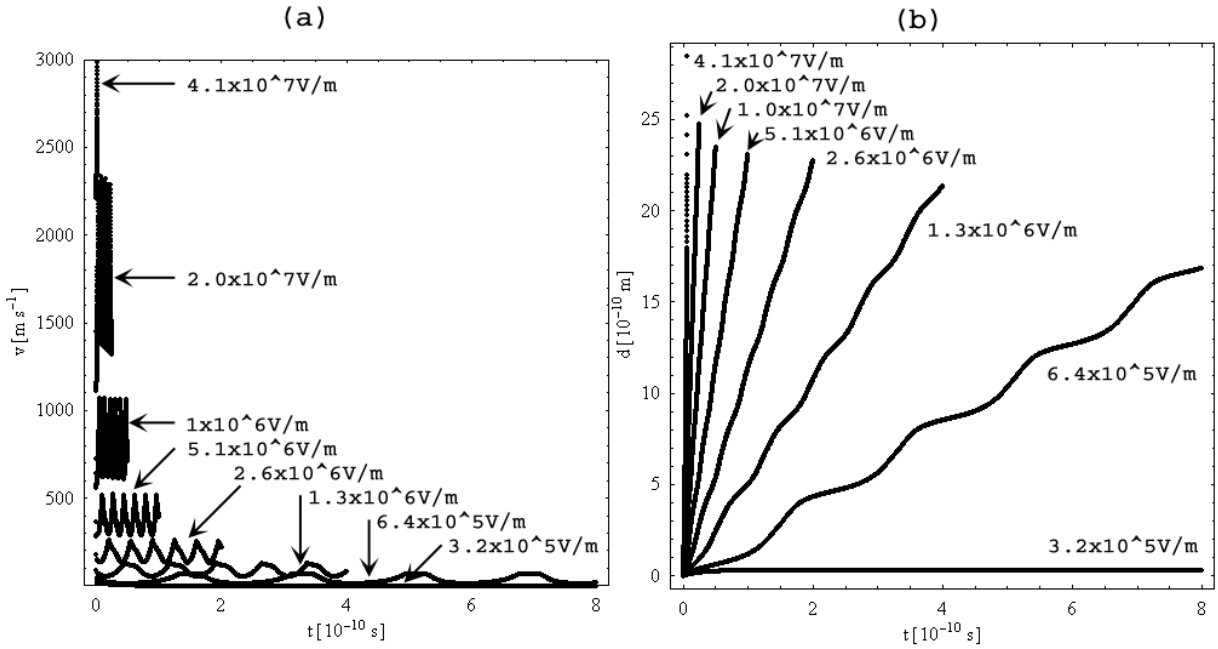

Figure 7.16: (a) Velocity of T180{001} domain wall in tetragonal phase of $BaTiO_3$ for $\Delta =$ 0.4 nm. (b) Distance of T180{001} wall from its original position. Values of electric field E_x given next to appropriate curves.

Chapter 8

Conclusions

In this thesis, analytical and numerical modeling of domain wall properties using GGLD phenomenological model is presented.

Profiles of domain walls were computed analytically within GGLD model within charge-free approximation. This approach enables to compare all domain walls in $BaTiO_3$ from different points of view (e.g. thickness and energy density). Estimates of wall thicknesses provides valuable information about validity and limits of continuous phenomenological approach.

Computer program for simulation of evolution, formation and coarsening of domain structure in ferroelectric perovskite materials was developed and tested. Results obtained with use of this computational tool were discussed and compared with other published simulations and with exact analytical solutions.

Recently estimated gradient constants and background permittivity [26] were used in calculations. This choice has crucial impact on domain wall thicknesses and other properties.

8.1 Analytical computation of wall profiles

Shape of complete set of elastically compatible domain walls were predicted analytically within div $\mathbf{P} = 0$ approximation that implies constant projection of polarization to the direction of domain wall normal. In order to obtain one-dimensional model, which is solvable analytically, only one of polarization components varies across domain wall. Both assumptions and their influence on result were discussed.

Thickness and energy per area was computed for all domain walls. Three temperatures were chosen that correspond to tetragonal (298 K), orthorombic (208 K) and rhombohedral (118 K) phase. Resulting values and all parameters for one dimensional model are given in Tab. 3.3. In addition, temperature dependence of thickness and energy of domain wall per area is provided in Fig. 3.9.

Charge-free assumption was found reasonable in all cases. On the contrary, it was found that Ising assumption can lead to an unstable profile in several cases. These are: O180{001}, O120, R180$\{1\bar{1}0\}$, R180$\{\bar{2}11\}$ and R109 walls. Cross section of the Euler-Lagrange potential (perpendicular to the normal of domain wall) shows additional minimum for non-zero component P_t (as indicated by the diagrams in Fig. 3.14). Simple numerical simulations (with two-dimensional degree of polarization) revealed appearance Bloch-type domain wall.

All results can be easily recomputed and verified since analytical expressions are provided. It also enables to use this results for another material with similar structure.

8.2 Numerical simulation of domain evolution

Numerical approach enables to study complicated structures for which analytical solution does not exist. It also enables observation of the dynamics of polarization field evolution, appearance of domains, their coarsening and behavior of polarization under changing electrical and mechanical conditions or changing temperature.

The computational tool `ferrodo` for modeling of the evolution of a polarization field was developed. It enables independent choice of dimensionality of space domain and also dimensionality of the order parameter – polarization. Mechanical and electrical boundary conditions together with temperature of the sample can be prescribed and can vary during simulation. Polarization fields and other obtained results and data are saved to files and displayed in the form of images. Several tests of the program and also examples of use are provided.

Tests indicate that maximal spacing of a discrete grid is about half the thickness of the simulated domain wall. With this or lower spacing, the analytical results are well reproduced by numerically obtained profiles.

Evolution of polarization from quenched paraelectric cubic phase was performed for all phases. In tetragonal phase, both 90 degree and 180 degree domains coexist in stripe domain structure. It match experimental observations. Electrostatic dipole-dipole interaction influences crucially resulting architecture of polarization field.

Results comparable to other published simulations were obtained [28] using the same parameter set.

Interference of domain walls was discussed in dependence on their mutual distance in stress-free sample. With dipole-dipole interaction taken into account, the value of spontaneous polarization in the middle of the T90 domain decreases with decreasing distance of walls. On the contrary, without dipole-dipole interaction the wall profile is almost independent on wall distance.

Mobility of domain wall in dependence on grid size and magnitude of external electric field was estimated numerically. Relatively good agreement with theoretical results was acquired for 90 degree domain wall in tetragonal phase of $BaTiO_3$.

Chapter 9

Future work

9.1 Implementation of absolutely stable algorithm

Although simple Euler method is sometimes used in simulations, it is inappropriate for solving such demanding problems. Time step of stable method is restricted by square of the spatial step. Recently published semi-implicit method, which is also used for simulations presented in this thesis, enables great improvement of time step, but still suffers from limitation of time step by the spatial step.

In recent years there appeared absolutely stable methods for similar problems. Significant advance in numerics was achieved namely in the branch of modeling of metals and alloys, where Cahn-Hillard equation is used for simulation of precipitation and chemical ordering during solidification [47, 48]. Absolutely stable algorithms was also proposed for Allen-Cahn dynamics in Ref. [48].

This innovative method might be applicable to GGLD model driven by Landau-Khalatnikov governing equation. It would offer faster simulations with bigger time-step. Euler and semi-implicit method will nevertheless remain as a reference.

9.2 Generalization of boundary conditions

Original concern in bulk material and consequent periodicity of polarization and displacement field seems rather restrictive for certain applications of the numerical model. Generalization of boundary conditions as in Ref. [24] would be beneficial.

To do this, it will be necessary to perform computation in real space, which will require profound changes in the kernel of the program. It is expected, that local electric field and equilibrium strain field will be computed separately with use of Poisson equation and Euler-Lagrange equation for mechanical equilibrium, resp. (with appropriate boundary conditions). Evolution of polarization field will be then computed with use of Landau-Khalatnikov governing equation in real space.

In the case of both previously mentioned changes (implementation of absolutely stable algorithm and generalization of boundary conditions), the existence of the working and verified reference simulation kernel will be highly valuable.

9.3 Simulation of chemical ordering and appearance of nanoclusters

Giant dielectric and piezoelectric coefficients in relaxor ferroelectrics are often ascribed to chemical ordering - appearance of polar nanoclusters is associated to a certain degree of occupational order in the B-site perovskite sublattice. It would be interesting to simulate the behavior of polarization field in a lattice with realistic chemical correlations. It can be simulated for example using an appropriate Cahn-Hillard equation for diffusion of ions in the crystal lattice.

Appendix A

Additional materials for analytical approach

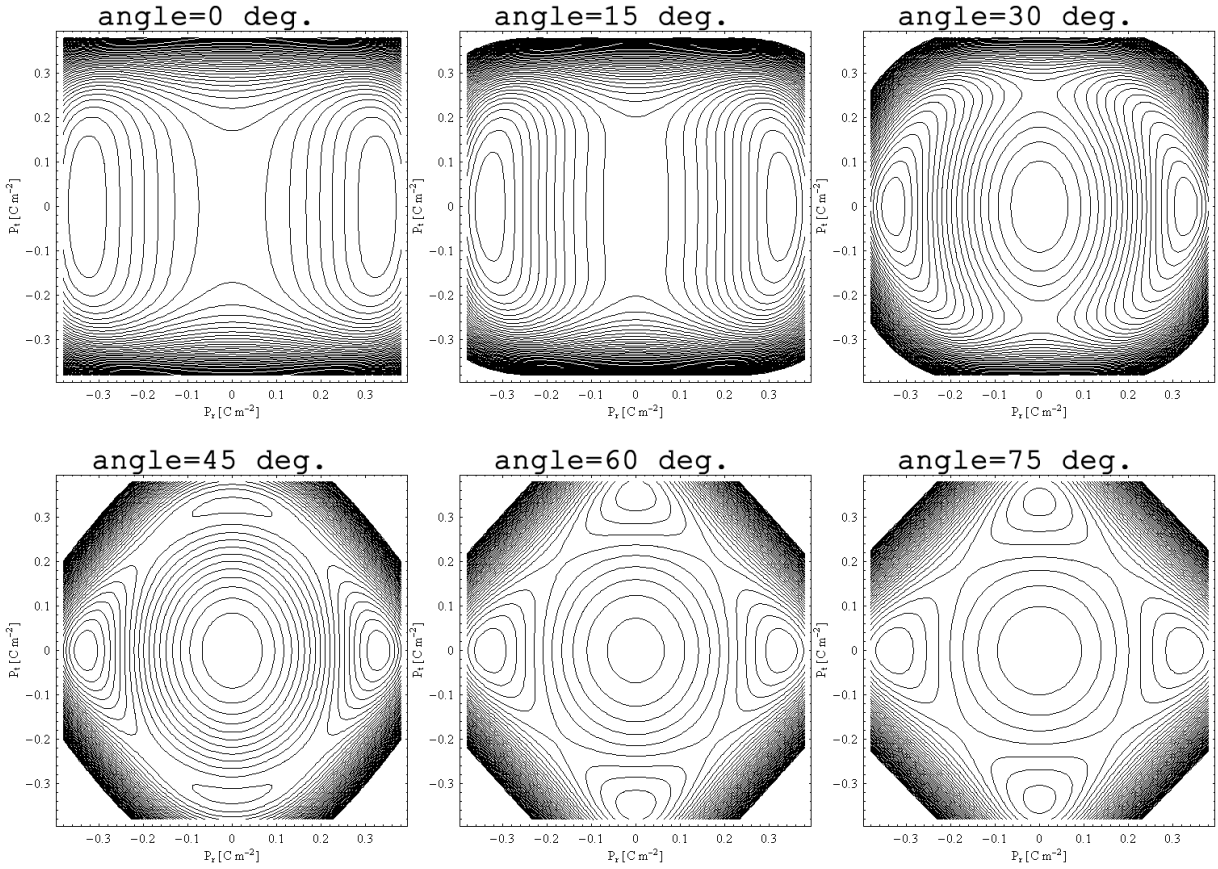

Figure A.1: Cross sections of Euler-Lagrange potential in orthorombic phase for T=208 K. Cross sections are made in rt plane, which is perpendicular to a particular O180 domain wall. Component P_s of the polarization is fixed to the boundary value (see e.g. Tab. A.1). The direction of the wall changes between $[1\bar{1}0]$ and [001], which are directions of O180$\{1\bar{1}0\}$ and O180$\{001\}$ domain walls. Appearance of side minima is clearly visible. Angles denotes deviation from $[1\bar{1}0]$ direction. Contours are distributed linearly.

Table A.1: Values of polarization vector in the infinity and in the middle of the domain wall.

Original coordinate system

Wall	$\mathbf{P}(-\infty)$	$\mathbf{P}(\infty)$	$\mathbf{P}(0)$
T180{001}	(0.265,0.000,0.000)	(-0.265,0.000,0.000)	(0.000,0.000,0.000)
T180{011}	(0.265,0.000,0.000)	(-0.265,0.000,0.000)	(0.000,0.000,0.000)
T90	(0.265,0.000,0.000)	(0.000,-0.265,0.000)	(0.133,-0.133,0.000)
O180{1$\bar{1}$0}	(0.234,0.234,0.000)	(-0.234,-0.234,0.000)	(0.000,0.000,0.000)
O180{001}	(0.234,0.234,0.000)	(-0.234,-0.234,0.000)	(0.000,0.000,0.000)
O90	(0.234,0.234,0.000)	(0.234,-0.234,0.000)	(0.234,0.000,0.000)
O60	(0.234,0.234,0.000)	(0.000,0.234,-0.234)	(0.117,0.234,-0.117)
O120	(0.234,0.234,0.000)	(0.000,-0.234,0.234)	(0.117,0.000,0.117)
R180{1$\bar{1}$0}	(0.220,0.220,0.220)	(-0.220,-0.220,-0.220)	(0.000,0.000,0.000)
R180{$\bar{2}$11}	(0.220,0.220,0.220)	(-0.220,-0.220,-0.220)	(0.000,0.000,0.000)
R109	(0.220,0.220,0.220)	(-0.220,-0.220,0.220)	(0.000,0.000,0.220)
R71	(0.220,0.220,0.220)	(0.220,-0.220,0.220)	(0.220,0.000,0.220)

Transformed coordinate system

Wall	$\mathbf{P}'(-\infty)$	$\mathbf{P}'(\infty)$	$\mathbf{P}'(0)$
T180{001}	(0.265,0.000,0.000)	(-0.265,0.000,0.000)	(0.000,0.000,0.000)
T180{011}	(0.265,0.000,0.000)	(-0.265,0.000,0.000)	(0.000,0.000,0.000)
T90	(0.188,0.188,0.000)	(-0.188,0.188,0.000)	(0.000,0.188,0.000)
O180{1$\bar{1}$0}	(0.331,0.000,0.000)	(-0.331,0.000,0.000)	(0.000,0.000,0.000)
O180{001}	(0.331,0.000,0.000)	(-0.331,0.000,0.000)	(0.000,0.000,0.000)
O90	(0.234,0.234,0.000)	(-0.234,0.234,0.000)	(0.000,0.234,0.000)
O60	(0.166,0.195,0.210)	(-0.166,0.195,0.210)	(0.000,0.195,0.210)
O120	(0.287,0.166,0.000)	(-0.287,0.166,0.000)	(0.000,0.166,0.000)
R180{1$\bar{1}$0}	(0.381,0.000,0.000)	(-0.381,0.000,0.000)	(0.000,0.000,0.000)
R180{$\bar{2}$11}	(0.381,0.000,0.000)	(-0.381,0.000,0.000)	(0.000,0.000,0.000)
R109	(0.311,0.220,0.000)	(-0.311,0.220,0.000)	(0.000,0.220,0.000)
R71	(0.220,0.311,0.000)	(-0.220,0.311,0.000)	(0.000,0.000,0.000)

Table A.2: Values of strain tensor in the infinity and in the middle of the domain wall. All inspected domain walls are listed. Voigt notation is used, $e_\sigma = 2e_{ij}$ for $\sigma > 3$ and $i \neq j$.

Original coordinate system			
Wall	$\mathbf{e}(-\infty)$	$\mathbf{e}(\infty)$	$\mathbf{e}(0)$
T180{001}	(7.77,-3.18,-3.18,0.00,0.00,0.00)	(7.77,-3.18,-3.18,0.00,0.00,0.00)	(7.77,-3.18,-2.99,0.00,0.00,0.00)
T180{011}	(7.77,-3.18,-3.18,0.00,0.00,0.00)	(7.77,-3.18,-3.18,0.00,0.00,0.00)	(7.77,-3.09,-3.09,0.19,0.00,0.00)
T90	(7.77,-3.18,-3.18,0.00,0.00,0.00)	(-3.18,7.77,-3.18,0.00,0.00,0.00)	(1.92,1.92,-3.18,0.00,0.00,0.74)
O180{1$\bar{1}$0}	(4.37,2.79,-4.96,0.00,0.00,0.00)	(4.37,2.79,-4.96,0.00,0.00,0.00)	(2.42,2.42,-4.96,0.00,0.00,3.90)
O180{001}	(3.58,3.58,-4.96,0.00,0.00,1.59)	(3.58,3.58,-4.96,0.00,0.00,1.59)	(3.58,3.58,-4.66,0.00,0.00,1.59)
O90	(3.58,3.58,-4.96,0.00,0.00,1.59)	(3.58,3.58,-4.96,0.00,0.00,-1.59)	(3.72,3.58,-4.96,0.00,0.00,0.00)
O60	(3.58,3.58,-4.96,0.00,0.00,1.59)	(-4.96,3.58,3.58,-1.59,0.00,0.00)	(-1.00,3.62,-1.00,-1.00,0.62,1.00)
O120	(3.58,3.58,-4.96,0.00,0.00,1.59)	(3.58,3.58,-4.96,-1.59,0.00,0.00)	(-0.91,3.58,-0.91,-0.79,-0.44,0.79)
R180{1$\bar{1}$0}	(0.97,0.97,0.97,1.40,1.40,1.40)	(0.97,0.97,0.97,1.40,1.40,1.40)	(0.01,0.01,0.97,1.40,1.40,3.32)
R180{$\bar{2}$11}	(0.97,0.97,0.97,1.40,1.40,1.40)	(0.97,0.97,0.97,1.40,1.40,1.40)	(-0.36,0.68,0.68,0.81,2.66,2.66)
R109	(0.97,0.97,0.97,1.40,1.40,1.40)	(0.97,0.97,0.97,-1.40,-1.40,1.40)	(0.97,0.97,1.24,0.00,0.00,1.40)
R71	(0.97,0.97,0.97,1.40,1.40,1.40)	(0.97,0.97,0.97,-1.40,1.40,-1.40)	(1.04,0.97,1.04,0.00,1.53,0.00)

Transformed coordinate system			
Wall	$\mathbf{e}'(-\infty)$	$\mathbf{e}'(\infty)$	$\mathbf{e}'(0)$
T180{001}	(7.77,-3.18,-3.18,0.00,0.00,0.00)	(7.77,-3.18,-3.18,0.00,0.00,0.00)	(7.77,-2.99,-3.18,0.00,0.00,0.00)
T180{011}	(7.77,-3.18,-3.18,0.00,0.00,0.00)	(7.77,-3.18,-3.18,0.00,0.00,0	(7.77,-3.00,-3.18,0.00,0.00,0.00)
T90	(2.30,2.30,-2.18,0.00,0.00,10.94)	(2.30,2.30,-2.18,0.00,0.00,-10.94)	(2.30,1.55,-2.18,0.00,0.00,0.00)
O180{1$\bar{1}$0}	(4.37,2.78,-4.96,0.00,0.00,0.00)	(4.37,2.78,-4.96,0.00,0.00,0.00)	(4.37,0.47,-4.96,0.00,0.00,0.00)
O180{001}	(4.37,-4.96,2.79,0.00,0.00,0.00)	(4.37,-4.96,2.79,0.00,0.00,0.00)	(4.37,-4.66,2.79,0.00,0.00,0.00)
O90	(3.58,3.58,-4.96,0.00,0.00,1.59)	(3.58,3.58,-4.96,0.00,0.00,-1.59)	(3.58,3.72,-4.96,0.00,0.00,0.00)
O60	(-0.69,-0.47,3.36,2.18,0.00,8.61)	(-0.69,-0.47,3.36,2.18,0.00,-8.61)	(-0.69,-1.04,3.36,2.63,0.00,0.00)
O120	(2.69,-0.69,0.21,6.32,-3.65,5.84)	(2.69,-0.69,0.21,-6.32,-3.65,-5.84)	(2.69,-1.12,0.21,0.00,-3.65,0.00)
R180{1$\bar{1}$0}	(2.38,0.27,0.27,0.00,0.00,0.00)	(2.38,0.27,0.27,0.00,0.00,0.00)	(2.38,-1.65,0.27,0.00,0.00,0.00)
R180{$\bar{2}$11}	(2.38,0.27,0.27,0.00,0.00,0.00)	(2.38,0.27,0.27,0.00,0.00,0.00)	(2.38,-1.65,0.27,0.00,0.00,0.11)
R109	(1.68,0.97,0.27,0.00,0.00,1.98)	(1.68,0.97,0.27,0.00,0.00,-1.98)	(1.68,1.23,0.27,0.00,0.00,0.00)
R71	(0.97,1.68,0.27,0.00,0.00,1.98)	(0.97,1.68,0.27,0.00,0.00,-1.98)	(0.97,1.80,0.27,0.00,0.00,0.00)

Appendix B

Fourier Transform

B.1 Continuous Fourier transform

Definition of the Fourier transform used in this work is

$$\begin{aligned} \mathcal{F}\left[f(\mathbf{r})\right](\mathbf{k}) &= f(\mathbf{k}) = \int \mathrm{d}\mathbf{r} f(\mathbf{r}) e^{-i\mathbf{kr}} \\ \mathcal{F}^{-1}\left[f(\mathbf{k})\right](\mathbf{r}) &= f(\mathbf{r}) = \frac{1}{(2\pi)^3} \int \mathrm{d}\mathbf{r} f(\mathbf{r}) e^{i\mathbf{kr}} \ . \end{aligned} \tag{B.1}$$

The convolution of functions in direct space corresponds to multiplication of their Fourier images

$$\int \mathrm{d}\mathbf{r}_1 \Phi(\mathbf{r}_1 - \mathbf{r}) = \frac{1}{(2\pi)^6} \iint \mathrm{d}\mathbf{k}_1 \mathrm{d}\mathbf{k} \int \mathrm{d}\mathbf{r}_1 P(\mathbf{k}_1)\Phi(\mathbf{k}) e^{i(\mathbf{k}_1 + \mathbf{r}_1 - \mathbf{r})} = \mathcal{F}^{-1}\left[P(\mathbf{k})\Phi(\mathbf{k})\right] \ . \tag{B.2}$$

Key relations for derivation Fourier transform of electrostatic dipole-dipole interaction are (Ref. [49])

$$\mathcal{F}\left[\frac{1}{|\mathbf{R}|}\right] = \frac{4\pi}{|\mathbf{k}|^2} \ , \tag{B.3}$$

where $|\mathbf{R}| = \sqrt{x^2 + y^2}$. Using sequence of derivatives in direct space

$$\frac{\partial^2}{\partial x^2}\left(\frac{1}{|\mathbf{R}|}\right) = -\frac{|\mathbf{R}|^2 + 3R_x^2}{|\mathbf{R}|^5} \tag{B.4}$$

$$\frac{\partial^2}{\partial x \partial y}\left(\frac{1}{|\mathbf{R}|}\right) = \frac{R_x R_y}{|\mathbf{R}|^5} \ , \tag{B.5}$$

we get immediately

$$\mathcal{F}\left[-\frac{|\mathbf{R}|^2 + 3R_x^2}{|\mathbf{R}|^5}\right] = -4\pi \frac{k_x^2}{|\mathbf{k}|^2} \tag{B.6}$$

$$\mathcal{F}\left[\frac{3R_x R_y}{|\mathbf{R}|^5}\right] = -4\pi \frac{k_x k_y}{|\mathbf{k}|^2} \ . \tag{B.7}$$

B.2 Discrete Fourier transform

The discrete Fourier transform is defined according to Ref. [70] as

$$\begin{aligned}\mathcal{F}_{\mathrm{d}}\left[f(\mathbf{r}_{\mathrm{d}})\right](\mathbf{k}_{\mathrm{d}}) = & \sum_{x=0}^{R_1-1}\sum_{y=0}^{R_2-1}\sum_{z=0}^{R_3-1} f([x,y,z])exp\left[-2\pi i\left(u\frac{x}{R_1}+v\frac{y}{R_2}+w\frac{z}{R_3}\right)\right] \\ \mathcal{F}_{\mathrm{d}}^{-1}\left[f(\mathbf{k}_{\mathrm{d}})\right](\mathbf{r}_{\mathrm{d}}) = & \frac{1}{R_1R_2R_3}\sum_{u=0}^{R_1-1}\sum_{v=0}^{R_2-1}\sum_{w=0}^{R_3-1} f([u,v,w])exp\left[2\pi i\left(x\frac{u}{R_1}+y\frac{v}{R_2}+z\frac{w}{R_3}\right)\right] ,\end{aligned} \tag{B.8}$$

where $\mathbf{r}_{\mathrm{d}}$, $\mathbf{k}_{\mathrm{d}} \in (\{1,2,..,R_1\},\{1,2,..,R_2\},\{1,2,..,R_3\})$ stands for "discrete" point in direct and Fourier space, resp. $\mathbf{r}_{\mathrm{d}} = [x,y,z]$, $\mathbf{k}_{\mathrm{d}} = [u,v,w]$. Here, R_d is the number of discrete points in a particular direction. Normalization of transformed variables is performed for backward transform only. Discrete derivatives in Fourier space are

$$\mathcal{F}_{\mathrm{d}}\left[\frac{\partial f}{\partial x}(\mathbf{r}_{\mathrm{d}})\right](\mathbf{k}_{\mathrm{d}}) = \frac{2\pi k_{dx}}{R_1\Delta}\mathcal{F}_{\mathrm{d}}\left[f(\mathbf{r}_{\mathrm{d}})\right](\mathbf{k}_{\mathrm{d}}) , \tag{B.9}$$

where Δ is regular lattice spacing which we consider equal in all directions. Similarly, second derivatives are computed as

$$\begin{aligned}\mathcal{F}_{\mathrm{d}}\left[\frac{\partial^2 f}{\partial x^2}(\mathbf{r}_{\mathrm{d}})\right](\mathbf{k}_{\mathrm{d}}) &= \frac{4\pi^2 k_{dx}^2}{R_1^2\Delta^2}\mathcal{F}_{\mathrm{d}}\left[f(\mathbf{r}_{\mathrm{d}})\right](\mathbf{k}_{\mathrm{d}}) \\ \mathcal{F}_{\mathrm{d}}\left[\frac{\partial^2 f}{\partial x\partial y}(\mathbf{r}_{\mathrm{d}})\right](\mathbf{k}_{\mathrm{d}}) &= \frac{4\pi^2 k_{dx}k_{dy}}{R_1R_2\Delta^2}\mathcal{F}_{\mathrm{d}}\left[f(\mathbf{r}_{\mathrm{d}})\right](\mathbf{k}_{\mathrm{d}}) .\end{aligned} \tag{B.10}$$

Appendix C

Variation of the free energy functional

On the right-hand side of the Landau-Khalatnikov equation (5.2), there is a variation of the free energy functional (with eliminated elastic field) with respect to a component of polarization. Functional consists of four parts: Landau, gradient, elastostriction and electrostatic. Changes of individual parts of the free energy functional are computed with respect to small variation of $P_i(\mathbf{x})$ by $\delta P_i(\mathbf{x})$.

C.1 Landau energy variation

Variation of Landau energy with respect to component P_1 (other components can be obtained by cyclic permutation $(1 \to 2, 2 \to 3, 3 \to 1)$ reads

$$\begin{aligned}
&\frac{\delta F_{\mathrm{L}}^{(e)}\left[\{P_i\}\right]}{\delta P_1} = \\
&= \lim_{t\to 0}\frac{1}{t}\int_\Omega \mathrm{d}\mathbf{x}[\alpha_1\left[\left[(P_1(\mathbf{x})+t\delta P_1(\mathbf{x}))^2+P_2^2(\mathbf{x})+P_3^2(\mathbf{x})\right]-\left[P_1^2(\mathbf{x})+P_2^2(\mathbf{x})+P_3^2(\mathbf{x})\right]\right] \\
&\quad +\alpha_{11}\left[\left[(P_1(\mathbf{x})+t\delta P_1(\mathbf{x}))^4+P_2^4(\mathbf{x})+P_3^4(\mathbf{x})\right]-\left[P_1^4(\mathbf{x})+P_2^4(\mathbf{x})+P_3^4(\mathbf{x})\right]\right]+...] \\
&= \lim_{t\to 0}\int_\Omega \mathrm{d}\mathbf{x}[\alpha_1\left[2P_1(\mathbf{x})\delta P_1(\mathbf{x})+t(\delta P_1(\mathbf{x}))^2\right] \\
&\quad +\alpha_{11}\left[4P_1^3(\mathbf{x})\delta P_1(\mathbf{x})+6tP_1^2(\mathbf{x})(\delta P_1(\mathbf{x}))^2\right]+...] \\
&= \int_\Omega \mathrm{d}\mathbf{x}\left[2\alpha_1 P_1(\mathbf{x})\delta P_1(\mathbf{x})+4\alpha_{11}P_1^3(\mathbf{x})\delta P_1(\mathbf{x})+...\right]\ . \qquad \text{(C.1)}
\end{aligned}$$

Variation with respect to value P_i in a particular point $\mathbf{r}$ can be evaluated by setting $\delta P(\mathbf{x}) = \delta_{\mathbf{r}}(\mathbf{x})$

$$\begin{aligned}
\frac{\delta F_{\mathrm{L}}^{(e)}\left[\{P_i\}\right]}{\delta P_1(\mathbf{r})} &= P_1(\mathbf{r})[2\alpha_1+4\alpha_{11}P_1^2(\mathbf{r})+2\alpha_{12}\left(P_2^2(\mathbf{r})+P_3^2(\mathbf{r})\right) \\
&+ 6\alpha_{111}P_1^4(\mathbf{r})+2\alpha_{112}\left(P_2^4(\mathbf{r})+P_3^4(\mathbf{r})+2P_1^2(\mathbf{r})(P_2^2(\mathbf{r})+P_3^2(\mathbf{r}))\right) \\
&+ 2\alpha_{123}P_2^2(\mathbf{r})P_3^2(\mathbf{r}) \\
&+ 8\alpha_{1111}P_1^6(\mathbf{r})+2\alpha_{1112}\left(P_2^6+(\mathbf{r})P_3^6(\mathbf{r})+3P_1^4(\mathbf{r})(P_2^2(\mathbf{r})+P_3^2(\mathbf{r}))\right) \\
&+ 4\alpha_{1122}P_1^2(\mathbf{r})\left(P_2^4(\mathbf{r})+P_3^4(\mathbf{r})\right) \\
&+ 2\alpha_{1123}\left(2P_1^2(\mathbf{r})P_2^2(\mathbf{r})P_3^2(\mathbf{r})+P_2^2(\mathbf{r})P_3^2(\mathbf{r})(P_2^2(\mathbf{r})+P_3^2(\mathbf{r}))\right)]\ . \qquad \text{(C.2)}
\end{aligned}$$

C.2 Gradient energy variation

Ginzburg gradient energy functional is expressed in terms of derivatives of polarization. Here, for simplicity, energy functional is expected in the form

$$F_{\mathrm{G}}\left[P_{1,1}\right] = \int_{\Omega} \mathrm{dx} \frac{G_{11}}{2} \left(\frac{\partial P_1(x)}{\partial x}\right)^2 \ , \tag{C.3}$$

with P_1 dependent just on x. The variation is derived

$$\begin{aligned}
\frac{\delta F_{\mathrm{G}}\left[P_{1,1}\right]}{\delta P_1} &= \frac{G_{11}}{2} \lim_{t\to 0} \frac{1}{t} \left[\int_{\Omega} \mathrm{dx} \left[\frac{\partial (P_1(x) + t\delta P_1(x))}{\partial x}\right]^2 - \int_{\Omega} \mathrm{dx} \left[\frac{\partial P_1(x)}{\partial x}\right]^2 \right] \\
&= \frac{G_{11}}{2} \lim_{t\to 0} \int_{\Omega} \mathrm{dx} \left[2\frac{\partial P_1(x)}{\partial x}\frac{\partial \delta P_1(x)}{\partial x} + t\frac{\partial \delta P_1(x)}{\partial x}\right] \\
&= \frac{G_{11}}{2} \int_{\Omega} \mathrm{dx} \left[2\frac{\partial P_1(x)}{\partial x}\frac{\partial \delta P_1(x)}{\partial x}\right] \\
&= \frac{G_{11}}{2} \left[2\frac{\partial P_1(x)}{\partial x}\delta P_1(x)\right]_{\partial\Omega} - G_{11} \int \mathrm{dx} \left[\frac{\partial^2 P_1(x)}{\partial x^2}\delta P_1(x)\right] \ .
\end{aligned} \tag{C.4}$$

Considering periodic boundary condition for $P(\mathbf{x})$ and $\delta P(\mathbf{x})$, the result is obtained in the form

$$\frac{\delta F_{\mathrm{G}}\left[P_{1,1}\right]}{\delta P_1(\mathbf{r})} = -G_{11}\frac{\partial^2 P_1(x)}{\partial x^2}(\mathbf{r}) \ . \tag{C.5}$$

C.3 Elastostriction energy variation

Formula for long-range elastostatic energy was derived in Sec. 2 in Eqn. 2.36. Derivation will be provided for the first part of this expression

$$F'_{\mathrm{Cq}}\left[\{P_i\}\right] = -\frac{1}{2} \iint \mathrm{ds}\,\mathrm{dt}\, \Psi_{11}(\mathbf{t}-\mathbf{s}) P_x^2(\mathbf{s}) P_y^2(\mathbf{t}) \ . \tag{C.6}$$

Other components are similar.

$$\begin{aligned}
&\frac{\delta F'_{\mathrm{Cq}}\left[\{P_i\}\right]}{\delta P_x} = \\
&= -\frac{1}{2} \lim_{t\to 0} \frac{1}{t} \iint \mathrm{ds}\,\mathrm{dt}\, \Psi_{11}(\mathbf{t}-\mathbf{s}) [(P_x(\mathbf{s}) - t\delta P_x(\mathbf{s}))^2 (P_x(\mathbf{t}) - t\delta P_x(\mathbf{t}))^2 - P_x^2(\mathbf{s}) P_x^2(\mathbf{t})] \\
&= -\frac{1}{2} \iint \mathrm{ds}\,\mathrm{dt}\, \Psi_{11}(\mathbf{t}-\mathbf{s}) \left[2P_x(\mathbf{s})\delta P_x(\mathbf{s}) P_x^2(\mathbf{t}) + 2P_x(\mathbf{t})\delta P_x(\mathbf{t}) P_x^2(\mathbf{s})\right] \\
&= -\int \mathrm{ds} P_x^2(\mathbf{s}) \int \mathrm{dt}\, \Psi_{11}(\mathbf{t}-\mathbf{s}) P_x(\mathbf{t})\delta P_x(\mathbf{t}) \\
&\quad -\int \mathrm{dt} P_x^2(\mathbf{t}) \int \mathrm{ds}\, \Psi_{11}(\mathbf{t}-\mathbf{s}) P_x(\mathbf{s})\delta P_x(\mathbf{s}) \\
&= -2\int \mathrm{ds} P_x^2(\mathbf{s}) \int \mathrm{dt}\, \Psi_{11}(\mathbf{t}-\mathbf{s}) P_x(\mathbf{t})\delta P_x(\mathbf{t}) \ .
\end{aligned} \tag{C.7}$$

Relation $\Psi_{\rho\sigma}(\mathbf{r}) = \Psi_{\rho\sigma}(-\mathbf{r})$, used in last step, holds due to the fact that $\Psi_{\rho\sigma}(\mathbf{k})$ is purely real in reciprocal space. We finally obtain the result in the form

$$\frac{\delta F'_{\mathrm{Cq}}\left[\{P_i\}\right]}{\delta P_x(\mathbf{r})} = -2P_x(\mathbf{r}) \int \mathrm{d}\mathbf{s}\, \Psi_{11}(\mathbf{r}-\mathbf{s}) P_x^2(\mathbf{s}) \ . \tag{C.8}$$

C.4 Electrostatic dipole-dipole energy variation

Derivation is given for two-dimensional case. Three-dimensional extension simply follows. Firstly, dipole-dipole energy is split into two parts:

$$\begin{aligned} F_{\mathrm{dep}}\left[\{P_i\}\right] &= \frac{1}{8\pi\epsilon_0\epsilon_B} \iint \mathrm{d}\mathbf{r}_1\mathrm{d}\mathbf{r}_2 \left[\frac{\mathbf{P}(\mathbf{r}_1)\cdot(\mathbf{P})(\mathbf{r}_2)}{|\mathbf{r}_1-\mathbf{r}_2|^3} - \frac{(\mathbf{P}(\mathbf{r})\cdot(\mathbf{r}_1-\mathbf{r}_2))(\mathbf{P}(\mathbf{r}_2)\cdot(\mathbf{r}_1-\mathbf{r}_2))}{|\mathbf{r}_1-\mathbf{r}_2|^5}\right] \\ &= \frac{1}{8\pi\epsilon_0\epsilon_B}\Bigg[\iint \mathrm{d}\mathbf{r}_1\mathrm{d}\mathbf{r}_2 \left[\frac{P_x(\mathbf{r}_1)P_x(\mathbf{r}_2)+P_y(\mathbf{r}_1)P_y(\mathbf{r}_2)}{|\mathbf{r}_1-\mathbf{r}_2|^3}\right] \\ &- 3\left[\frac{\left[P_x(\mathbf{r}_1)(\mathbf{r}_1-\mathbf{r}_2)_x + P_y(\mathbf{r}_1)(\mathbf{r}_1-\mathbf{r}_2)_y\right]\left[P_x(\mathbf{r}_2)(\mathbf{r}_1-\mathbf{r}_2)_x + P_y(\mathbf{r}_2)(\mathbf{r}_1-\mathbf{r}_2)_y\right]}{|\mathbf{r}_1-\mathbf{r}_2|^5}\right]\Bigg] \\ &= F_{\mathrm{dep1}}\left[\{P_i\}\right] - F_{\mathrm{dep2}}\left[\{P_i\}\right] \ . \end{aligned} \tag{C.9}$$

Functional derivative of the first part

$$\begin{aligned} &\frac{\delta F_{\mathrm{dep1}}\left[\{P_i\}\right]}{\delta P_x} = \\ &= \frac{1}{8\pi\epsilon_0\epsilon_B}\lim_{t\to 0} \iint \mathrm{d}\mathbf{r}_1\mathrm{d}\mathbf{r}_2 \frac{1}{t}\left[\frac{(P_x(\mathbf{r}_1)+t\delta P_x(\mathbf{r}_1))(P_x(\mathbf{r}_2)+t\delta P_x(\mathbf{r}_2)) - P_x(\mathbf{r}_1)P_x(\mathbf{r}_2)}{|\mathbf{r}_1-\mathbf{r}_2|^3}\right] \\ &= \frac{1}{8\pi\epsilon_0\epsilon_B} \iint \mathrm{d}\mathbf{r}_1\mathrm{d}\mathbf{r}_2 \left[\frac{P_x(\mathbf{r}_1)\delta P_x(\mathbf{r}_2) + P_x(\mathbf{r}_2)\delta P_x(\mathbf{r}_1)}{|\mathbf{r}_1-\mathbf{r}_2|^3}\right] \\ &\frac{\delta F_{\mathrm{dep1}}\left[\{P_i\}\right]}{\delta P_x(\mathbf{r})} = \\ &= \frac{2}{8\pi\epsilon_0\epsilon_B}\int \mathrm{d}\mathbf{r}_1 \left[\frac{P_x(\mathbf{r})}{|\mathbf{r}_1-\mathbf{r}|^3}\right] \ . \end{aligned} \tag{C.10}$$

Similarly, after slightly longer algebra

$$\begin{aligned} \frac{\delta F_{\mathrm{dep2}}\left[\{P_i\}\right]}{\delta P_x} &= \frac{3}{8\pi\epsilon_0\epsilon_B} \iint \mathrm{d}\mathbf{r}_1\mathrm{d}\mathbf{r}_2 \left[\frac{\delta P_x(\mathbf{r}_1)(\mathbf{r}_1-\mathbf{r}_2)_x\left[\mathbf{P}(\mathbf{r}_2)\cdot(\mathbf{r}_1-\mathbf{r}_2)\right]}{|\mathbf{r}_1-\mathbf{r}|^5}\right] \\ &+ \frac{3}{8\pi\epsilon_0\epsilon_B} \iint \mathrm{d}\mathbf{r}_1\mathrm{d}\mathbf{r}_2 \left[\frac{\delta P_x(\mathbf{r}_2)(\mathbf{r}_1-\mathbf{r}_2)_x\left[\mathbf{P}(\mathbf{r}_1)\cdot(\mathbf{r}_1-\mathbf{r}_2)\right]}{|\mathbf{r}_1-\mathbf{r}|^5}\right] \\ \frac{\delta F_{\mathrm{dep2}}\left[\{P_i\}\right]}{\delta P_x(\mathbf{r})} &= \frac{6}{8\pi\epsilon_0\epsilon_B}\int \mathrm{d}\mathbf{r}_1 \left[\frac{(\mathbf{r}_1-\mathbf{r})_x\left[\mathbf{P}(\mathbf{r})\cdot(\mathbf{r}_1-\mathbf{r})\right]}{|\mathbf{r}_1-\mathbf{r}|^5}\right] \ . \end{aligned} \tag{C.11}$$

Together, functional derivative of electrostatic dipole-dipole contribution with respect to P_x component of polarization field reads

$$\begin{aligned} \frac{\delta F_{\mathrm{dep}}\left[\{P_i\}\right]}{\delta P_x(\mathbf{r})} &= \frac{2}{8\pi\epsilon_0\epsilon_B}\int \mathrm{d}\mathbf{r}_1 \left[\frac{P_x(\mathbf{r}_1)}{|\mathbf{R}|^3} - \frac{3\mathbf{R}_x\left(P(\mathbf{r})\cdot\mathbf{R}\right)}{|\mathbf{R}|^5}\right] \\ &= \frac{2}{8\pi\epsilon_0\epsilon_B}\int \mathrm{d}\mathbf{r}_1 \left[\frac{P_x(\mathbf{r}_1)(|\mathbf{R}|^2-3R_x^2) - 3P_y(\mathbf{r}_1)R_xR_y}{|\mathbf{R}|^5}\right] \ . \end{aligned} \tag{C.12}$$

Appendix D

Elastostriction kernels

Long-range elastostatic interaction in the free energy functional with eliminated elastic field is determined by the form of angular kernels $\Phi_{\rho\sigma}(\hat{\mathbf{k}})$ in Eqn. 2.36. Their contribution to the generalized force, given by convolution (C.8), is equivalent to multiplication of Fourier image of polarization square (2.38) with elastostriction kernels $A_{\rho\sigma}(\hat{\mathbf{k}})$. Explicit form of these kernels, which were derived according to Ref. [18], reads:

$$
\begin{aligned}
A_{\rho\rho}(\hat{\mathbf{k}}) &= \hat{q}_{22}^2 B_{\rho\rho}(\hat{\mathbf{k}}) + 2q_{12}\hat{q}_{22}\sum_{\sigma=1}^{3} B_{\rho\sigma}(\hat{\mathbf{k}}) + q_{12}^2 \sum_{\rho=1}^{3}\sum_{\sigma=1}^{3} B_{\rho\sigma}(\hat{\mathbf{k}}) && \text{for } \rho = 1,2,3 \\
A_{23}(\hat{\mathbf{k}}) &= \hat{q}_{22}^2 B_{23}(\hat{\mathbf{k}}) - q_{12}\hat{q}_{22}\sum_{\rho=1}^{3} B_{\rho 1}(\hat{\mathbf{k}}) + q_{11}q_{12}\sum_{\rho=1}^{3}\sum_{\sigma=1}^{3} B_{\rho\sigma}(\hat{\mathbf{k}}) \\
A_{32}(\hat{\mathbf{k}}) &= A_{23}(\hat{\mathbf{k}}) \\
A_{13}(\hat{\mathbf{k}}) &= \hat{q}_{22}^2 B_{13}(\hat{\mathbf{k}}) - q_{12}\hat{q}_{22}\sum_{\rho=1}^{3} B_{\rho 2}(\hat{\mathbf{k}}) + q_{11}q_{12}\sum_{\rho=1}^{3}\sum_{\sigma=1}^{3} B_{\rho\sigma}(\hat{\mathbf{k}}) \\
A_{31}(\hat{\mathbf{k}}) &= A_{13}(\hat{\mathbf{k}}) \\
A_{12}(\hat{\mathbf{k}}) &= \hat{q}_{22}^2 B_{12}(\hat{\mathbf{k}}) - q_{12}\hat{q}_{22}\sum_{\rho=1}^{3} B_{\rho 3}(\hat{\mathbf{k}}) + q_{11}q_{12}\sum_{\rho=1}^{3}\sum_{\sigma=1}^{3} B_{\rho\sigma}(\hat{\mathbf{k}}) \\
A_{21}(\hat{\mathbf{k}}) &= A_{12}(\hat{\mathbf{k}}) \\
A_{1\sigma}(\hat{\mathbf{k}}) &= \hat{q}_{22}q_{44}B_{1\sigma}(\hat{\mathbf{k}}) + q_{12}q_{44}\sum_{\rho=1}^{3} B_{\rho\sigma}(\hat{\mathbf{k}}) && \text{for } \sigma = 4,5,6 \\
A_{2\sigma}(\hat{\mathbf{k}}) &= \hat{q}_{22}q_{44}B_{2\sigma}(\hat{\mathbf{k}}) + q_{12}q_{44}\sum_{\rho=1}^{3} B_{\rho\sigma}(\hat{\mathbf{k}}) && \text{for } \sigma = 4,5,6 \\
A_{3\sigma}(\hat{\mathbf{k}}) &= \hat{q}_{22}q_{44}B_{3\sigma}(\hat{\mathbf{k}}) + q_{12}q_{44}\sum_{\rho=1}^{3} B_{\rho\sigma}(\hat{\mathbf{k}}) && \text{for } \sigma = 4,5,6 \\
A_{\rho\sigma}(\hat{\mathbf{k}}) &= q_{44}^2 B_{\rho\sigma}(\hat{\mathbf{k}}) && \text{for } \rho,\sigma = 4,5,6
\end{aligned}
$$

Polarization square vector (2.38) reduces to $\mathbf{Y} = [P_1^2, P_2^2, 0, 0, 0, P_1P_2]$ and only components $A_{11}(\hat{\mathbf{k}})$, $A_{22}(\hat{\mathbf{k}})$, $A_{12}(\hat{\mathbf{k}})$, $A_{16}(\hat{\mathbf{k}})$, $A_{26}(\hat{\mathbf{k}})$, $A_{66}(\hat{\mathbf{k}})$ contributes to the free energy. Shapes of these functions are plotted in Figs. D.1,D.2.

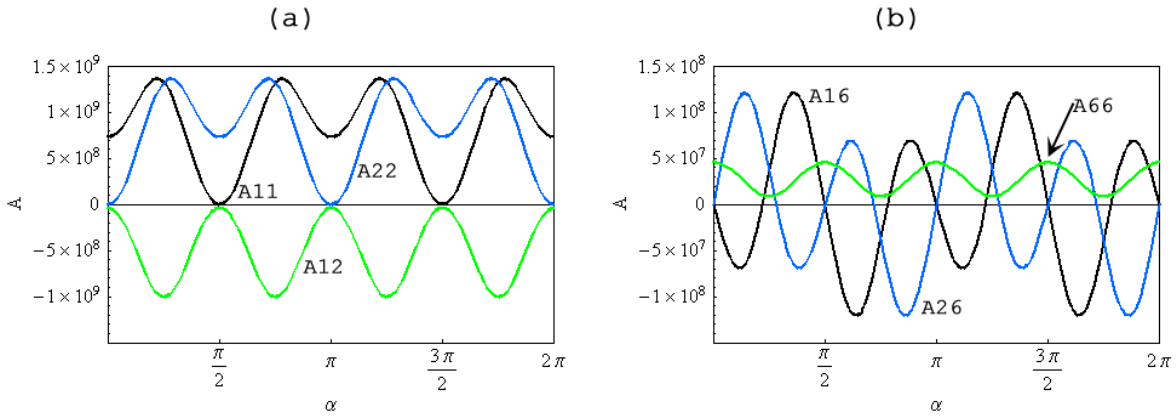

Figure D.1: Angular dependence of elastostriction kernels $A_{11}(\hat{\mathbf{k}})$, $A_{22}(\hat{\mathbf{k}})$, $A_{12}(\hat{\mathbf{k}})$, $A_{16}(\hat{\mathbf{k}})$, $A_{26}(\hat{\mathbf{k}})$, $A_{66}(\hat{\mathbf{k}})$ in two dimensions.

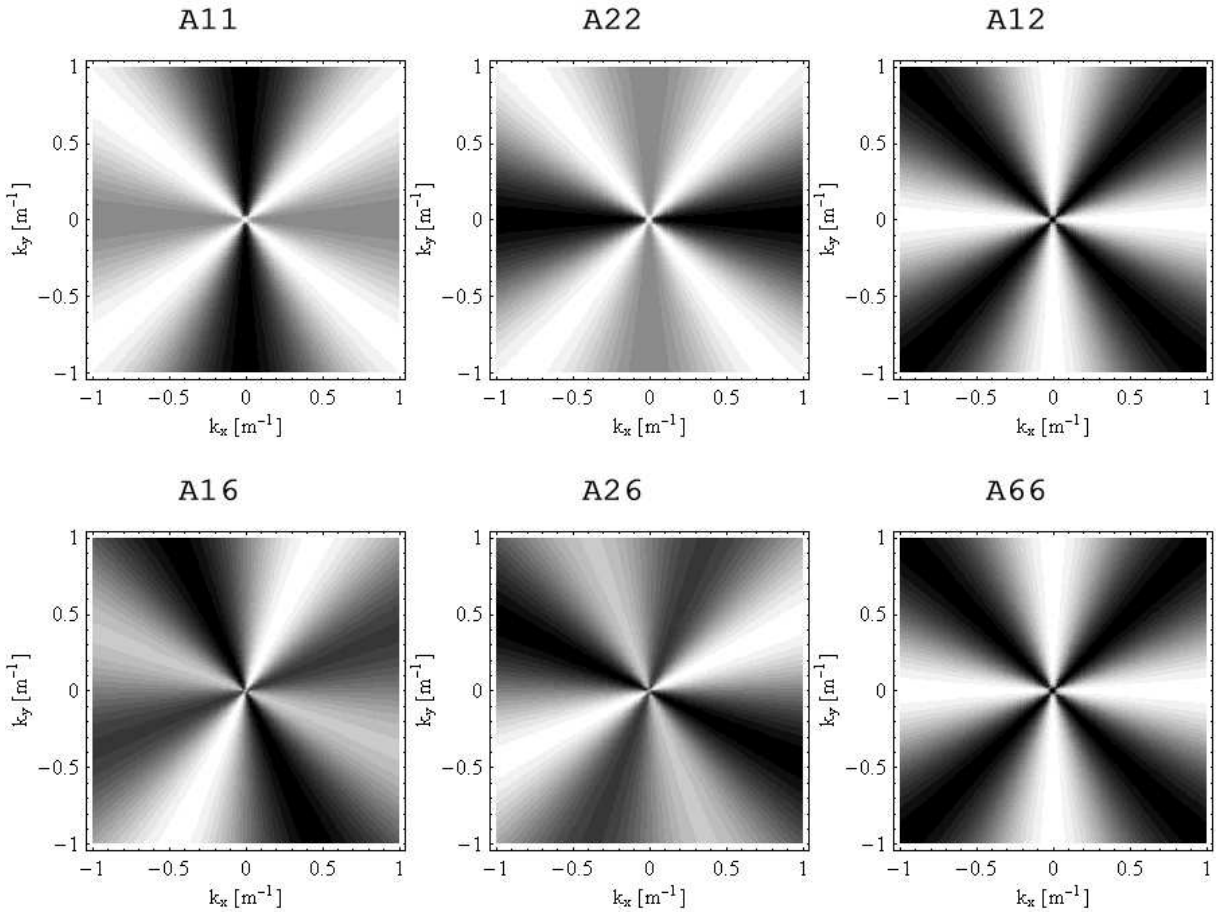

Figure D.2: Schematic plots of elastostriction kernels $A_{11}(\hat{\mathbf{k}})$, $A_{22}(\hat{\mathbf{k}})$, $A_{12}(\hat{\mathbf{k}})$, $A_{16}(\hat{\mathbf{k}})$, $A_{26}(\hat{\mathbf{k}})$, $A_{66}(\hat{\mathbf{k}})$ in two-dimensional reciprocal space. The darker the color, the lower the value.

Appendix E

Tensors and transformation of coordinates

Physical properties of the matter are represented by tensors. Neumann's principle (A crystal's point group is a subgroup of the symmetry of that crystal's properties.) allows determination of number of independent components of a tensor. Symmetry properties of tensors are described in detail e.g. in [51].

E.1 Transformation of tensors

Transformation from the original to a new coordinate system, which denoted by primes, is given by transformation matrix **R**. It can be written as product of rotation matrices along individual axes

$$\mathbf{R} \;=\; \mathbf{R_x} \cdot \mathbf{R_y} \cdot \mathbf{R_z} \;, \tag{E.1}$$

where

$$\begin{aligned}
\mathbf{R_x} &= \begin{bmatrix} 1 & 0 & 0 \\ 0 & cos(\alpha) & -sin(\alpha) \\ 0 & sin(\alpha) & sin(\alpha) \end{bmatrix} \;, \\
\mathbf{R_y} &= \begin{bmatrix} cos(\beta) & 0 & sin(\beta) \\ 0 & 1 & 0 \\ -sin(\beta) & 0 & cos(\beta) \end{bmatrix} \;, \\
\mathbf{R_z} &= \begin{bmatrix} cos(\gamma) & -sin(\gamma) & 0 \\ sin(\gamma) & cos(\gamma) & 0 \\ 0 & 0 & 1 \end{bmatrix} \;.
\end{aligned} \tag{E.2}$$

Angles α, β and γ are rotations along axes x, y and z, respectively (see Fig. E.1). A vector $\mathbf{x}$ transforms according to the relation

$$x'_m = \sum_i R_{mi} x_i \;. \tag{E.3}$$

A tensor of second-order $\mathbf{e}$ transforms as

$$e'_{mn} = \sum_{ij} R_{mi} e_{ij} R^{-1}_{jn} \;. \tag{E.4}$$

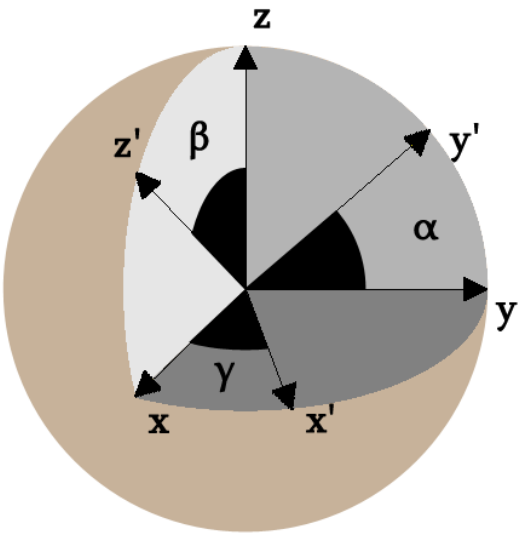

Figure E.1: Rotation along individual axes.

Transformation relations for fourth-rank elastic, gradient and electrostriction tensors **C**, **G** and **q**

$$\begin{aligned} C'_{mnop} &= \sum_{ijkl} C_{ijkl} R^{-1}_{im} R_{nj} R^{-1}_{ko} R_{pl} \\ G'_{mnop} &= \sum_{ijkl} G_{ijkl} R^{-1}_{im} R_{nj} R^{-1}_{ko} R_{pl} \\ q'_{mnop} &= \sum_{ijkl} q_{ijkl} R^{-1}_{im} R_{nj} R^{-1}_{ko} R^{-1}_{lp} \ . \end{aligned} \tag{E.5}$$

Gradient coefficients G_{ijkl} have the same transformation properties as C_{ijkl} (see relation for gradient part of the free energy, Eqn. 2.18).

E.2 Voigt notation

For a second rank tensor **e** it defines $e_1 = e_{11}$, $e_2 = e_{22}$, $e_3 = e_{33}$, $e_4 = 2e_{23}$, $e_5 = 2e_{13}$ and $e_6 = 2e_{12}$. Symmetric fourth-rank tensor like tensor of elastic constants in Voigt notation reads

$$C = \begin{bmatrix} C_{1111} & C_{1122} & C_{1133} & C_{1123} & C_{1113} & C_{1112} \\ & C_{2222} & C_{2233} & C_{2223} & C_{2213} & C_{2212} \\ & & C_{3333} & C_{3323} & C_{3313} & C_{3312} \\ & & & C_{2323} & C_{2313} & C_{2312} \\ & SYM. & & & C_{1313} & C_{1312} \\ & & & & & C_{1212} \end{bmatrix} = \begin{bmatrix} C_{11} & C_{12} & C_{13} & C_{14} & C_{15} & C_{16} \\ & C_{22} & C_{23} & C_{24} & C_{25} & C_{26} \\ & & C_{33} & C_{34} & C_{35} & C_{36} \\ & & & C_{44} & C_{45} & C_{46} \\ & SYM. & & & C_{55} & C_{56} \\ & & & & & C_{66} \end{bmatrix} . \tag{E.6}$$

The tensor of electrostriction constants **q** that express linear-quadratic coupling of deformation and polarization is not generally symmetric. For cubic symmetry we define $q_{44} = 2q_{1212}$. Vector

of polarization square is defined $P = \{P_{11}, P_{22}, P_{33}, P_{23}, P_{13}, P_{12}\}$.

E.3 Transformation matrices for domain walls in $BaTiO_3$

In Sec. 3, the transformation of coordinates $(x, y, z) \rightarrow (r, s, t)$ is performed in order to simplify computation of domain wall profiles. Rotation matrices of these transformations are provided bellow.

T180{001}

$$\begin{bmatrix} 1 & 0 & 0 \\ 0 & 0 & 1 \\ 0 & -1 & 0 \end{bmatrix} \tag{E.7}$$

T180{011}

$$\frac{1}{\sqrt{2}} \begin{bmatrix} \sqrt{2} & 0 & 0 \\ 0 & 1 & 1 \\ 0 & -1 & 1 \end{bmatrix} \tag{E.8}$$

T180{011}

$$\frac{1}{\sqrt{2}} \begin{bmatrix} \sqrt{2} & 0 & 0 \\ 0 & 1 & 1 \\ 0 & -1 & 1 \end{bmatrix} \tag{E.9}$$

T90

$$\frac{1}{\sqrt{2}} \begin{bmatrix} 1 & 1 & 0 \\ 1 & -1 & 0 \\ 0 & 0 & -\sqrt{2} \end{bmatrix} \tag{E.10}$$

O180{1$\bar{1}$0}

$$\frac{1}{\sqrt{2}} \begin{bmatrix} 1 & 1 & 0 \\ 1 & -1 & 0 \\ 0 & 0 & -\sqrt{2} \end{bmatrix} \tag{E.11}$$

O180{001}

$$\frac{1}{\sqrt{2}} \begin{bmatrix} 1 & 1 & 0 \\ 0 & 0 & \sqrt{2} \\ 1 & -1 & 0 \end{bmatrix} \tag{E.12}$$

O90

$$\begin{bmatrix} 0 & 1 & 0 \\ 1 & 0 & 0 \\ 0 & 0 & -1 \end{bmatrix} \tag{E.13}$$

O60

$$\begin{bmatrix} \frac{1}{\sqrt{2}} & 0 & \frac{1}{\sqrt{2}} \\ \frac{e_a-e_c}{\sqrt{2(e_a-e_c)^2+4e_b^2}} & \frac{2e_b}{\sqrt{2(e_a-e_c)^2+4e_b^2}} & \frac{e_c-e_a}{\sqrt{2(e_a-e_c)^2+4e_b^2}} \\ \frac{-e_b}{\sqrt{(e_a-e_c)^2+2e_b^2}} & \frac{e_a-e_c}{\sqrt{(e_a-e_c)^2+2e_b^2}} & \frac{e_b}{\sqrt{(e_a-e_c)^2+2e_b^2}} \end{bmatrix} \tag{E.14}$$

O120

$$\frac{1}{\sqrt{6}} \begin{bmatrix} 1 & 2 & -1 \\ \sqrt{3} & 0 & \sqrt{3} \\ \sqrt{2} & -\sqrt{2} & -\sqrt{2} \end{bmatrix} \tag{E.15}$$

R180{1$\bar{1}$0}

$$\frac{1}{\sqrt{6}} \begin{bmatrix} \sqrt{2} & \sqrt{2} & \sqrt{2} \\ \sqrt{3} & -\sqrt{3} & 0 \\ 1 & 1 & -2 \end{bmatrix} \tag{E.16}$$

R180{$\bar{2}$11}

$$\frac{1}{\sqrt{6}} \begin{bmatrix} \sqrt{2} & \sqrt{2} & \sqrt{2} \\ -2 & 1 & 1 \\ 0 & -\sqrt{3} & \sqrt{3} \end{bmatrix} \tag{E.17}$$

R109

$$\frac{1}{\sqrt{2}} \begin{bmatrix} 1 & 1 & 0 \\ 0 & 0 & \sqrt{2} \\ 1 & -1 & 0 \end{bmatrix} \tag{E.18}$$

R71

$$\frac{1}{\sqrt{2}} \begin{bmatrix} 0 & \sqrt{2} & 0 \\ 1 & 0 & 1 \\ 1 & 0 & -1 \end{bmatrix} \tag{E.19}$$

Appendix F

Compatibility relations

In the linear theory of elasticity, components of strain tensor are derivatives of displacement.

$$e_{ij} = \frac{1}{2}\left(\frac{\partial u_i}{\partial x_j} + \frac{\partial u_j}{\partial x_i}\right) \tag{F.1}$$

If the computation is provided in terms of components of strain tensor, additional conditions must be included to provide existence of a displacement field for given components of strain tensor. These compatibility conditions have the form

$$\epsilon_{ikl}\epsilon_{jmn}e_{ln,km} = 0 \tag{F.2}$$

for $i, j, k, l, m, n \in \{1, 2, 4\}$. In three dimensions, there are six independent equations

$$\begin{aligned}
e_{22,33} - 2e_{23,23} + e_{33,22} &= 0 \\
e_{11,33} - 2e_{13,13} + e_{33,11} &= 0 \\
e_{11,22} - 2e_{12,12} + e_{22,11} &= 0 \\
-e_{11,23} + e_{12,13} + e_{13,12} - e_{23,11} &= 0 \\
-e_{22,13} + e_{12,23} + e_{23,12} - e_{13,22} &= 0 \\
-e_{33,12} + e_{13,23} + e_{23,13} - e_{12,33} &= 0\ ,
\end{aligned} \tag{F.3}$$

which reduce to one relation in two dimensional space.

$$e_{11,22} - 2e_{12,12} + e_{22,11} = 0\ . \tag{F.4}$$

In Sec. 3, where only variation along second coordinate (s) is taken into account in quasi one dimensional calculations, compatibility conditions simplifies to

$$\begin{aligned}
e_{tt,ss} &= 0 \\
e_{rr,ss} &= 0 \\
e_{rt,ss} &= 0\ .
\end{aligned} \tag{F.5}$$

Mechanical compatibility conditions are not included in numerical computation in this work, because the elastic field is eliminated in every step with explicit use of displacement field, Eqn. 2.25. Consequently, the existence of an underlying field of displacements is provided.

Bibliography

[1] N. Setter, D. Damjanovic, L. Eng, G. Fox, S. Gevorgian, S. Hong, A. Kingon, H. Kohlstedt, N. Y. Park, G.B. Stephenson, I. Stolitchnov, A.K. Tagantsev, D.V. Taylor, T.Y. Tamada and S. Streiffer: Ferroelectric thin films: Review of materials, properties, and applications, J. Appl. Phys **100**, 051606 (2006).

[2] V. Giurgiutiu: Mechatronics Aspect of Smart Materials Induced Strain Actuation, 7^{th} Mechatronics Forum Internattional Conference, (2000).

[3] H. Fu and E. Cohen: Polarization rotation mechanism for ultrahigh electromechanical response in single-crystal piezoelectrics, Nature **403**, 281 (2000).

[4] J. Fousek and V. Janovec: The orientation of domain walls in twinned ferroelectric crystals, J. Appl. Phys. **40**, 135 (1969).

[5] A.F. Devonshire: Theory of ferroelectrics, Adv. Phys. **3**, 85 (1954).

[6] K. Aizu: Possible species of ferromagnetic, ferroelectric, and ferroelastic crystals, Phys. Rev. B **2**, 754 (1970).

[7] M. Abplanalp, L.M. Eng and P. Gunter: Mapping the domain distribution at ferroelectric surfaces by scanning force microscopy, Appl. Phys. A **66**, S231 (1998).

[8] V. Dvořák: Improper Ferroelectrics, Ferroelectrics **7**, 1 (1974).

[9] T. Ostapchuk, J. Petzelt, M. Savinov, V. Buscaglia and L. Mitoseriu: Grain-size effect in $BaTiO_3$: study by far infrared spectroscopy, Phase Transitions **79**, 361 (2006).

[10] S. Wada, K. Yako, H. Kakemoto, T. Tsurumi, and T. Kiguchi: Enhanced piezoelectric properties of barim titanate single crystals with different engineered-domain sizes, J. Appl. Phys. **98**, 014109 (2005).

[11] V. Janovec, V. Dvořák and J. Petzelt: Symmetry classification and properties of equitranslation structural phase-transitions, Czech J. Phys. **25**, 1362 (1975).

[12] Y. L. Li, L. E. Cross and L. Q. Chen: A phenomenological thermodynamic potential for $BaTiO_3$ single crystals, J. Appl. Phys. **98**, 064101 (2005).

[13] A.J. Bell: Phenomenologically derived electric field-temperature phase diagrams and piezoelectric coefficients for single crystal barium titanate under fields along different axes, J. Appl. Phys. **89**, 3907 (2000).

[14] A.J. Bell and L.E. Cross, Ferroelectrics **59**, 197 (1984).

[15] J. Fousek, D.B. Litvin and L.E. Cross: Domain Geometry engineering and domain average engineering of ferroics, J. Phys.: Condens. Matter. **13**, L33 (2001).

[16] J. Fuksa and V. Janovec: Macroscopic symmetries and domain configurations of engineered domain structures, J. Phys.: Condens. Matter. **14**, 3795 (2002).

[17] J. Fousek: Permissible domain walls in ferroelectric species, Czech J. Phys. **21**, 955 (1971).

[18] S. Nambu and D. A. Sagala: Domain formation and elastic long-range interaction in ferroelectric perovskites, Phys. Rev. B **50**, 5838 (1994).

[19] H. L. Hu and L. Q. Chen: Computer simulation of 90^o ferroelectric domain formation in two-dimensions, Mater. Sci. Eng. A **238**, 182 (1997).

[20] H. L. Hu and L. Q. Chen: Three-Dimensional Simulation of Ferroelectric Domain Formation, J. Am. Ceram. Soc. **81**, 492 (1998).

[21] R. Ahluwalia, T. Lookman, A. Saxena and W. Cao: Electromechanical properties of multi-domain ferroelectrics, cond-mat/0308232 (2003).

[22] X. Ren: Large electri-field-induced strain in ferroelectric crystals by point-defect-mediated reversible domain switching, Nature Materials **3**, 91 (2004).

[23] W.L. Warren, G.E. Pike, K. Vanheusden, D. Dimos, B.A. Tuttle and J. Robertson: Defect-dipole alignment and tetragonal strain in ferroelectrics, J. Appl. Phys. **79**, 9250 (1995).

[24] W. Zhang and K. Bhattacharya: A computational model of ferroelectric domains. Part I: model formulation and domain switching, Acta Mater. **53**, 185 (2005).

[25] W. Zhang and K. Bhattacharya: A computational model of ferroelectric domains. Part II: grain boundaries and deffect pinning, Acta Mater. **53**, 199 (2005).

[26] J. Hlinka and P. Marton: Phenomenological model of 90^o domain wall in $BaTiO_3$ type ferroelectrics, Phys. Rev. B **74**, 104104 (2006).

[27] J. Hlinka and P. Marton: Ferroelastic Domain Walls in Barium Titanate - Quantitative Phenomenological Model, Integrated Ferroelectrics [SUBMITTED].

[28] P. Marton and J. Hlinka: Simulation of domain patterns in $BaTiO_3$, Phase Transitions **79**, 467 (2006).

[29] L.A. Shuvalov, J. Phys. Soc. Jpn. **28** (Supplement), 38 (1970).

[30] Landolt-Börnstein, New Series 16: Ferroelectric and related substances, Springer-Verlag Berlin·Heidelberg·New York 1981

[31] A.G. Khachaturyan: Theory of structural transformations in solids, Willey, New York (1983).

[32] L.Q. Chen and J.Shen: Applications of semi-implicit Fourier-spectral method to phase field equations, Computer Physics Communications **108**, 147 (1998).

[33] W. Cao and L. E. Cross: Theory of tetragonal twin structures in ferroelectric perovskites with a first-order phase transition, Phys. Rev. B **44**, 5 (1991).

[34] X. R. Huang, S. S. Jiang, X. B. Hu and W. J. Liu: Theory of twinning in the orthorombic phase of ferroelectric perovskites, J. Phys.: Condens. Matter **9**, 4467 (1997).

[35] J. Erhart, W. Cao, J. Fousek: The structure of S-Wall in $m\bar{3}m \rightarrow mmm$ ferroelastics, Ferroelectrics **252**, 137 (2001)

[36] M.E. Lines and A.M. Glass: Principles and applications of ferroelectrics and related materials, Clarendon, Oxford (1979).

[37] A.F. Devonshire: Theory of Barium Titanate. – Part I., (1949).

[38] J. Hlinka and E. Klotins: Application of elastostatic Green function tensor technique to electrostriction in cubic, hexagonal and orthorombic crystals, J. Phys.: Condens. Matter. **15**, 5755 (2003).

[39] Y. Ishibashi and E. Salje: A theory of Ferroelectric 90 Degree Domain Wall , J. Phys. Soc. Jpn. **71**, 2800 (2002).

[40] V. Janovec: A symmetry approach to domain structures, Ferroelectrics **12**, 43 (1976).

[41] J.L. Servoin, F. Gervais, A.M. Quittet and Y. Luspin: Infrared and raman responses in perovskite ferroelectric crystals: Aparent inconsistencies, Phys. Rev. B **21**, 2038 (1980).

[42] J. Hlinka, J. Petzelt, S. Kamba, D. Noujni and T. Ostapchuk: Infrared dielectric response of relaxor ferroelectrics, Phase Transitions **79**, 41 (2006).

[43] L.D. Landau and I.M. Khalatnikov, Dok. Akad. Nauk SSSR **96**, 469 (1954).

[44] J. Hlinka: Mobility of ferroelastic domain wall in barium titanate, Ferroelectrics **349**, 1 (2007).

[45] R.H. Lyddane, R.G. Sachs and E. Teller: On the Polar vibrations of Alkali Halides, Phys. Rev. **59**, 673 (1941).

[46] D. Gottlieb and S.A. Orszag: Numerical Analysis of Spectral Method, Society for Industrial and Applied Mathematics, Philadelfia, Pennsylvania (1977).

[47] D.J. Eyre: Unconditionally gradient stable time marching the Cahn-Hillard equation, MRS Symposium Proceedings **529**, 39 (1998).

[48] B.P. Vollmayr-Lee and A.D. Rutenberg: Fast and accurate coarsening simulation with and unconditionally stable time step, Phys. Rev. E **68**, 066703 (2003).

[49] B.C. Vladimirov: Obobščennyje funkcii v matematičesoj fizike (Special functions in mathematical physics), Moskva, NAUKA (1976).

[50] International Tables for Crystallography, Vol. A, (1996).

[51] J.F. Nye: Physical properties of crystals, Oxford (1957).

[52] S.E. Park and T.R. Shrout: Ultrahigh strain and piezoelectric behavior in relaxor based ferroelectric single crystals, J. Appl. Phys. **82**, 1804 (1997).

[53] D.L. Rousseau, R.P. Bauman and S.P.S. Porto: Normal Mode Determination in Crystals, Journal of Raman Spectroscopy **10**, 253 (1981).

[54] E.J. Huibregtse, W.H. Bessey and M.E. Drougard: Electromechanical Behavior of Single Crystals of Barium Titanate from 25 to 160^{o}C, J. Appl. Phys **30**, 899 (1959).

[55] M. Kempa, J. Hlinka, J. Kulda, P. Bourges, A. Kania and J. Petzelt: Lattice dynamics of cubic $PbTiO_3$ by inelastic neutron scattering, Phase Transitions **79**, 351 (2006).

[56] J. Hlinka, M. Kempa, J. Kulda, P. Bourges, A. Kania and J. Petzelt: Lattice dynamics of ferroelectric $PbTiO_3$ by inelastic neutron scattering, Phys. Rev. B **73**, 140101(R) (2006).

[57] L.M. Eng, M. Abplanalp and P. Gunter: Ferroelectric domain switching in tri-glycine sulphate and barium-titanate bulk single crystals by scanning microscopy, Appl. Phys. A **66**, S679 (1998).

[58] M. Bouville and R. Ahluwalia: Interplay between diffusive and displacive phase transformations: Time-temperature-transformation diagrams and microstructures, Phys. Rev. Lett. **97**, 055701 (2006).

[59] S. Choudhury, Y.L. Li, C.E. Krill III and L.-Q. Chen: Phase-field simulation of polarization switching and domain evolution in ferroelectric polycrystals, Acta. Mater **53**, 5313 (2005).

[60] W. Zhong, D. Vanderbilt and K.M. Rabe: First-principles theory of ferroelectric phase transitions for perovskites: The case of $BaTiO_3$, Phys. Rev. B **52**, 6301 (1995).

[61] ANSI/IEEE 176: Standard on piezoelectricity (1987).

[62] C.P. Pole Jr.: Encyclopedic Dictionary of Condensed Matter Physics, Elsevier Academic Press (2004).

[63] M.T. Dove: Sructure and Dynamics - An atomic view of materials, Oxford UNIVERSITY PRESS (2001).

[64] Ch. Kittel: Introduction to Solid State Physics, Willey (2005).

[65] I. Štol: Mechanika, Czech Technical University Press (1998).

[66] O. Litzman, M. Sekanina: Užití grup ve fyzice, ACADEMIA (1982).

[67] ČSN ISO 5807: Zpracování informací. Dokumentační symboly a konvence pro vývojové diagramy toku dat, programů a systémů, síťové diagramy a diagramy zdrojů systémů.

[68] ČSN ISO 690: Bibliografické citace dokumentů.

[69] APC International, Ltd., http://www.americanpiezo.com (2007)

[70] FFTW library, Version 3.1., http://www.fftw.org (2007)

[71] PGPLOT Graphics Subroutine Library, Version 5.1.1., http://www.astro.caltech.edu/∼tjp/pgplot (2006)

[72] DoITPoMS Micrograph Library, http://www.doitpoms.ac.uk/miclib/micrographs/large/000199.gif (2007)

[73] DoITPoMS Micrograph Library, http://www.doitpoms.ac.uk/miclib/micrographs/large/000663.gif (2007)

[74] Bilbao Crystallographic server, http://www.cryst.ehu.es (2007)

List of publications

Publications in international journals

P. Marton and J. Hlinka: "Simulation of domain patterns in $BaTiO_3$", Phase Transitions 79, 467 (2006).

J. Hlinka and P. Marton: "Phenomenological model of a 90 degree domain wall in $BaTiO_3$-type ferroelectrics", Phys. Rev. B 74, 104104 (2006).

P. Marton, J. Hlinka and I. Rychetský: "Domain walls in ferroelectric $BaTiO_3$: Systematic study in framework of Generalized Ginzburg-Landau-Devonshire phenomenological model", being prepared for publication.